Heterogeneous Ultrafast Energy Transfer in Photosynthetic Proteins

by

Raymundo Moya III

B.S., Rice University (2016)

Submitted to the Department of Chemistry
in partial fulfillment of the requirements for the degree of

Doctor of Philosophy in Chemistry

at the

MASSACHUSETTS INSTITUTE OF TECHNOLOGY

February 2022

Author .....
Department of Chemistry
January 14, 2022

Certified by .....
Gabriela S. Schlau-Cohen
Associate Professor of Chemistry
Thesis Supervisor

Accepted by .....
Adam Willard
Associate Professor of Chemistry
Graduate Officer

This doctoral thesis has been examined by a Committee of the Department of Chemistry as follows:

Keith A. Nelson .....
Chairman, Thesis Committee
Haslam and Dewey Professor of Chemistry

Gabriela S. Schlau-Cohen .....
Thesis Supervisor
Associate Professor of Chemistry

Jianshu Cao .....
Member, Thesis Committee
Professor of Chemistry

Heterogeneous Ultrafast Energy Transfer in Photosynthetic Proteins

by

Raymundo Moya III

Submitted to the Department of Chemistry
on January 14, 2022, in partial fulfillment of the
requirements for the degree of
Doctor of Philosophy in Chemistry

Abstract

Photosynthesis begins with the absorption and rapid transport of energy through a protein network to reach the reaction center, where conversion to chemical energy occurs. The energy transport is facilitated through a series of energy transfer events between pigments bound to a protein backbone. These steps exhibit a remarkable near-unity quantum efficiency. Energy transfer rates are exquisitely sensitive to intermolecular distances, which vary within proteins due to thermal fluctuations of the structure. As a result, models predict that the energy transfer rates vary dramatically between proteins, producing some instances of inefficient energy transfer. Reconciling the high efficiency with the presence of thermal fluctuations has not been possible, because whether energy transfer rates in photosynthetic proteins actually vary and, if so, by how much has not been measured.

Previous experiments to measure rates relied on ensemble ultrafast spectroscopy, which is limited to average values. With single-molecule approaches, we can overcome the limitations of ensemble averaging by measuring individual proteins. However, single-molecule experiments have been primarily restricted to fluorescence, which occurs on a nanosecond timescale. The limited knowledge provided by ensemble averaging or nanosecond dynamics cannot describe heterogeneity in femtosecond energy transfer rates. Therefore, direct measurements of the distribution are required.

In this thesis, we expand upon a novel technique, single-molecule pump-probe spectroscopy (SM2P), which measures energy transfer rates at the single-molecule level. In Chapter 2, I describe a newly developed SM2P apparatus that is easily tunable across the visible region and demonstrate its utility on a fluorescent dye. In Chapter 3, I expand upon these results by applying SM2P to photosynthetic light-harvesting systems, where we are able to directly measure the distribution of energy transfer rates on cyanobacterial light-harvesting subunits. These novel experiments provide insight into how photosynthetic light-harvesting proteins are robust to thermal fluctuations and tightly regulate energy transfer rates. Lastly, in Chapter 4 I present the first single-molecule experiments on light-harvesting complexes from cryptophyte algae. The results imply that light-harvesting complexes from crypto-

phytes maintain the ability to regulate light harvesting through quenched states that prevent excess sunlight from damaging the light-harvesting machinery.

Thesis Supervisor: Gabriela S. Schlau-Cohen
Title: Associate Professor of Chemistry

Acknowledgments

First, I want to thank my advisor, Prof. Gabriela Schlau-Cohen for providing the opportunity to ask some of the most interesting questions in physical chemistry. My discussions with Gabriela have made me a better scientist, writer, and speaker, but most importantly, she gave me the confidence to act on my own scientific convictions. I am also grateful to my committee members Profs. Keith Nelson and Jianshu Cao for their enthusiastic questions that paved the way to multiple insights in my research throughout the years.

I, of course, have to thank all of the Schlau-Cohen lab members that made graduate school the memorable experience that it was. From the Muddy to coffee to movies to six flags, one of the best part of the last couple years has been the people I shared the road with. I am particularly thankful to Toru Kondo, who is an expert in just about everything under the sun. On top of your infinite knowledge, you inspire me to be the greatest teacher and mentor that I can be. You are responsible for everything I know and I can't imagine being a quarter as successful without you having set the path. Audrey, forcing you to join the sm2p project was maybe the greatest idea I've ever had. More than a labmate, you were there for the late nights, the stress, the struggles, the achievements, and, more importantly, the croissants and coffee. To the other members of the Fantastic Four: Jesse, Olivia and Shwetha. Your companionship carried me through the hardest moments of graduate school. You all brought happiness into my life and I can't imagine having done this without your support. Olivia, you were always there for hot chocolate, conversation, and the positive outlook on life I wish I always had. Shwetha, you are, perhaps, the wittiest and kindest bully I have ever met. Jesse, thanks for making the trip through graduate school bearable. Whether it was the peanuts, the attitude, or the never-failing willingness for trips to the Muddy, thanks for making graduate school fun.

Then there's the rest of the lab. Mikaila and Steph, you two are probably the coolest people in graduate school. For making the lab a better place, the group is indebted to you. Minjung, you're still the smartest person I know. Your work served

as inspiration and I hope you forgive me for all the terrible ultrafast questions I bugged you with over the years. I can't forget to mention Steph here again, who happily took your place as ultrafast expert and teaches me new random photophysics every day. I also want to thank Julianne Troiano who carried me through my first real project, and taught me how to carry awesome science through to publication. More importantly, Julianne taught me that scientists can, in fact, be cool. Thanks to Raju Regmi, for being a beacon of light in life. Your never-ending positivity is contagious.

My Phd woud not have been the same without everyone who's come through the Schlau-Cohen lab — John Ogren, Sandra Mosquera Vázquez, Ashley Tong, Prem Manna, Muath Nairat, Steve Quinn, Courtney Olsen, Dvir Harris, Jiajia Guo, Dihao Wang, Arusha Acharyya Angela Lee, Shirley Chen, Paul Cesanna, Maddie Hoffman, Maddi Scott, Yi Ji, and, of course, Sadie — with all of you around, this has been a wonderful environment to learn and grow as a person. Within MIT, there's the army of staff that keeps the world spinning including Brian Pretti, Peter Giunta, Li Miao, Paula Robinson, Prossy Najjuma, Jennifer Weisman, Rebecca Teixeira, and Jay Matthews.

My time at MIT will be remembered through the Muddy crew. Jesse, Michael, Crystal, Lexie, and Amr: thanks for enjoying the High Life. These friendships are the most valuable lessons I take home from MIT. Of course, there's no better combination than the 6 Cherry Crew. Shaina, Andee, and Eliza, thanks for the memories. Matt, thanks for picking up where Shaina and Andee left off. I don't know how I managed to be so lucky to end up with this group of strangers in a city so far away. It was fun, it was terrible, it was rowdy, but most of all, it was home. Between all of you, I truly cherish our friendships. And to the rest of the Hamilton and Hamilton-adjacent crew — Lilly, Dave, Collin, Peter, Shannon, Phil, and Josh — thanks for being an escape from the vacuum of science.

To all my of Aunts, Uncles, and cousins of which there are too many to count, you are my inspiration to be better. Your resolve, strength, and love has been with me every step of the way. I miss all of you and remember you always. To Cecilia, Jeff,

Jasper, Mema and Pops. Thank you for taking me in; your warmth and kindness got me through these northeast winters. Lila, thank you for your unwavering support and strength. I cannot imagine having made it this far with out your warmth, encouragement,and confidence. I am blessed to have you as my partner as we climb mountains.

Finally, I have to thank my family. My parents, Dora and Raymundo Moya. None of this would be possible without your sacrifice. You instill in me the confidence to face my fears and the spirit to smile through life's challenges. And to my siblings, Melissa and Daniel Moya. You've been my best friends since the start and I can't imagine life without you.

Contents

Chapter 1

Introduction to Photosynthesis

1.1 Photosynthetic Light Harvesting

Photosynthesis is the powerhouse of most life on Earth, producing over 100 billion tons of biomass annually [1, 2]. Despite its prevalence and over two centuries of scientific study, its molecular mechanisms remain not fully understood. In the first steps of photosynthesis, solar energy capture to conversion can occur with a remarkable near-unity quantum efficiency [3–9]. The key parameters in this process are the rates of the constituent energy and charge transfer steps, which combine to control the overall efficiency [10–15]. The energy and charge transfer rates depend on intermolecular couplings, which scale nonlinearly with distance. Therefore, thermal fluctuations of the protein structure are predicted to produce heterogeneity in rates [16–23]. However, for high quantum efficiency, the heterogeneous rates must reliably produce efficient energy transfer. In material systems, this is accomplished with highly ordered, homogeneous materials [24–30]. How photosynthetic systems achieve this efficiency despite heterogeneous protein structures is not yet understood. Identifying how high quantum efficiency is maintained is both of fundamental interest and important to solar energy research. The proposed work accesses the distribution of energy transfer rates, which is the first step in addressing this question.

Developing theoretical models of energy transfer in photosynthesis has been a long-standing challenge. Energy transfer occurs between pigments (chlorophylls,

carotenoids, phycobilins) held within a protein matrix. The pigments are densely packed within the matrix, which gives rise to strong electronic coupling between pigments (J) and coupling between pigments and the protein (λ) [31, 32]. The mechanism of energy transfer depends on the balance of these two couplings. If the electronic coupling is stronger than the pigment-protein coupling, energy transfer is coherent or wavelike, as described by Redfield theory [16, 33, 34]. In contrast, if the pigment-protein coupling is stronger, energy transfer is incoherent or hopping-type, as described by Förster theory [35–38]. In photosynthetic systems, these couplings (λ, J) are the same order of magnitude and the energy transfer rate (k_{ET}) reaches a maximum, as described by hierarchical equations of motion [21, 39–43]. For individual energy transfer steps, the balance of these couplings, and thus the behavior, vary dramatically. Experimental results from ultrafast spectroscopy have revealed energy transfer in photosynthetic systems on timescales from tens of femtoseconds to tens of picoseconds, corresponding to coherent and incoherent transfer, respectively. [6, 44–46, 46, 47, 47–60].

Our understanding of energy transfer is further complicated by heterogeneity in the pigment-protein coupling. Due to thermal motion, the protein matrix is thought to fluctuate on timescales ranging from microseconds to seconds and length scales ranging from single bonds to the entire structure [61–65]. Characterizing these fluctuations for this wide range of scales is both an experimental and theoretical challenge, making our knowledge of these motions limited. The couplings are electrodynamic, and so are highly sensitive to position and relative orientation [33, 37, 43, 66–70]. Upon thermal fluctuations, the magnitude changes, which, in turn, changes the excited-state energies [71–75]. Theoretical models suggest that the heterogeneity in excited-state energies and pigment-protein couplings produces quantitatively and qualitatively differences in the energy transfer dynamics [76–85]. Energy transfer steps within a single protein are thought to fluctuate between incoherent and coherent mechanisms, and thus identical proteins may exhibit either type of dynamics [86]. Despite the predicted heterogeneity, the vast majority of proteins maintain efficient energy transfer, as evidenced by the near-unity quantum efficiency [10, 87]. However,

the true distribution of energy transfer rates is not yet known.

Single-molecule fluorescence spectroscopy has provided experimental confirmation of heterogeneity in excited-state energies. However, whether energetic heterogeneity produces energy transfer heterogeneity and, if so, how quantitatively and qualitatively different the microscopic behaviors are, have not yet been determined. As a result, it is not clear what distribution of energy transfer rates underlies the robust functionality observed in natural systems.

Here, we directly observe and causally systemize the heterogeneity in energy transfer rates for photosynthetic proteins. The heterogeneity reveals how tightly the protein structure regulates rates, and, in turn, the efficiency of solar energy conversion. From this information, we gain insight into how molecular machinery is optimized to maintain efficiency despite thermal fluctuations and identify the requisite tolerances, which are a necessary parameter for a blueprint of efficient light harvesting [3, 88–91].

1.2 Photosynthesis in Cyanobacteria

Cyanobacteria are evolutionarily the most ancient and numerically the most abundant photosynthetic system. In light harvesting, absorbed photo-energy transfers through a protein network, known as the phycobilisome, to reach the photosystem II reaction center (PSII RC) [5–7], where conversion to chemical energy occurs [8, 9]. As shown in Fig. 1-1a, the phycobilisomes sit on the phospholipid bilayer membrane, which contains the PSII RC [92, 93]. The phycobilisomes are formed from $2-5$ cylinders in a central core surrounded by $6-8$ rods, all of which consist of structurally-similar associated subunits called phycobiliproteins [92, 94]. The phycobiliproteins derive from a simple blueprint of a monomer base with $2-5$ pigments that can be tuned by electronic coupling (J), pigment-protein coupling (λ), or pigment composition. The rods are tube-like structures formed from two classes of subunits, phycoerythrin and phycocyanin, and funnel blue light to the redder core [94]. The cores are four trimers of the subunit allophycocyanin (APC) [94, 95]. One or more of these trimers is modified by a pigment red-shifted through a tighter binding pocket. This modified

APC, known as APC-B, serves as the lowest-energy site of the phycobilisome that transfers energy to the PSII RC [96, 97].

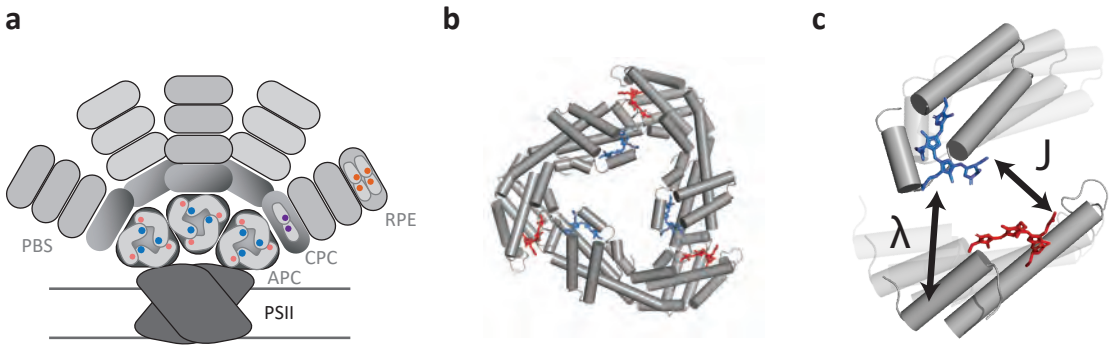

Figure 1-1: **Molecular machinery of cyanobacterial light harvesting.** (a) Associated rods, constructed from various phycoerythrin (e.g., RPE) and phycocyanin (e.g., CPC) subunits, and membrane-adjacent cylinders, constructed from allophycocyanin (APC), form the phycobilisome (PBS). Energy transfers through the rods to the cylinders to reach the Photosystem II reaction center (PSII RC). (b) APC has a trimeric structure, in which a phycocyanobilin dimer, shown in blue and red, sits across each interface between monomers [98]. (c) Energy transfer in photosyntheis is generically explained by the tuning of interpigment coupling (J) and coupling to the bath (λ).

Cyanobacteria adapt to environmental habitats by tuning the phycobilisome absorption, composition, and organization to utilize the available solar spectrum [99–105]. Structurally, this involves subunits with additional pigments [106], distinct pigment environments (λ) [107], changes in pigment-pigment coupling (J) [108], and altered aggregation state [94, 109, 110]. Through these variations, the subunits provide a range of excited-state properties to investigate individual parameters. The number and location of the numerous phycobiliproteins to optimize energy transfer to the reaction center [101–103]. Working as a funnel, energy absorbed in the rods rapidly migrates through the cylinders to the APC core and then transfers from the core to the PSII reaction center, where charge separation occurs [111–113]. The PBS construction highlights functional heterogeneity utilized by nature and provides a platform to understand efficient energy transformation though individual component functionality. Linker proteins tune the association of these phycobiliproteins within these structures and modify their spectral properties. Understanding how the

phycobilisome and other light-harvesting systems achieve high efficiency requires understanding these parameters. Here, we leverage this suite of subunits to identify the contribution of each parameter to heterogeneity in energy transfer. By exploiting the aggregation state of the phycobiliproteins, we gain insight into how nature uses these fundamental building blocks to harvest solar energy.

1.3 Photosynthesis in Cryptophytes

Cryptophyte algae, a relatively understudied photosynthetic organism, are thought to be the result of multiple endosymbiotic events, that somehow led to an organism that is essentially a moving chloroplast [114]. As cyanobacteria served as the endosymbiont, the light-harvesting complexes in cryptophytes maintain a high degree of similarity to subunits found in the phycobilisome [114]. While the phycobiliproteins in the phycobilisome generally consist of trimers and hexamers stacked into rod-like structures that sit on the outer surface of the thylakoid membrane, the phycobiliproteins in cryptophytes are dimers that lack higher order structure and are densely packed within the luminal space (see Figure 1-2) [115–118]. Similarly to cyanobacteria and red algae, the light-harvesting complexes are found as heterodimers with an $\alpha\beta$ building block, generally referred to as the monomer [119]. The high degree of similarity between the β subunit of cryptophytes and cyanobacteria as well as recent research connecting the α subunit to linker proteins that hold the phycobilisome together, support the secondary endosymbiotic hypothesis [120].

The diverse environments where crypotphyte algae, and photosynethetic organisms in general, thrive have led to a diverse set of photosynthetic subunits [114]. There are a plethora of phycobiliprotiens that have finely tuned their molecular blueprint to harvest light effeciently. This includes selection of pigments as well as their orientation within the protein backbone. This leads to a wealth of spectra available to these species as well as different energy transfer mechanisms [119, 121]. Ultrafast experiments have recently recorded the ultrafast dynamics as well, highlighting how these systems tune vibrational resonances in the excited electronic state to increase

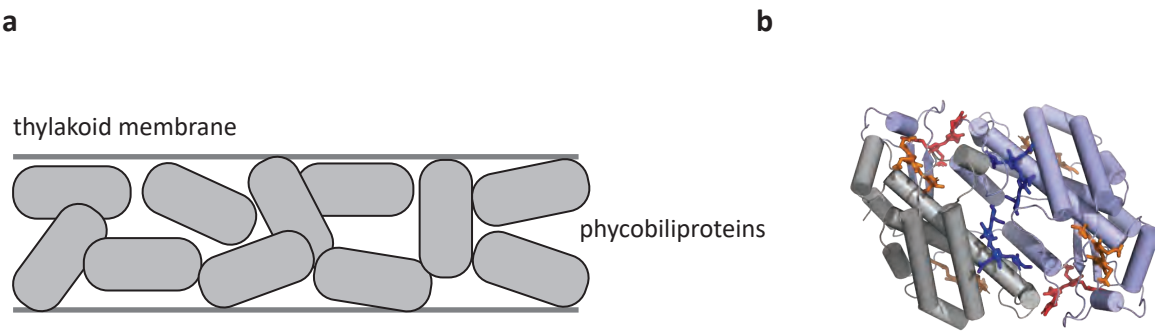

Figure 1-2: **Photosynthesis in cryptophyte algae.** (a) Schematic detailing how the phycobiliproteins are densely packed within the thylakod. (b) The structure of the phycobiliprotein, phycoerythrin 545 (PDB 1QGW) is illustrated.

the efficiency of light harvesting [122–127]. In this thesis, we will report the first single-molecule fluorescence experiments on phycobiliproteins from cyrptophyte algae. These experiments will provide a first look at how these proteins utilize protein conformations and asynchronous dynamics to function effectively.

1.4 Single-molecule pump-probe spectroscopy uncovers heterogeneity at the ultrafast timescale

Two current state-of-the-art techniques to characterize excited states are single-molecule spectroscopy and ultrafast spectroscopy, each of which has its own strengths and limitations. Optical single-molecule experiments are primarily restricted to fluorescence, which has two fundamental limitations: (1) fluorescence reports on the emissive state, not the initial and intermediate states in a multi-step process; and (2) fluorescence occurs on a nanosecond timescale, hiding faster processes [128, 129]. In contrast, ensemble transient absorption spectroscopy elucidates these faster processes [130–132], but the observed rates are ensemble-averaged and limited to synchronizable processes. This averages out conformational fluctuations and multi-step pathways that cannot be synchronized beyond the first step. Individually, both single-molecule and transient absorption spectroscopy have dramatically advanced our understanding of condensed-phase systems, characterizing heterogeneity and excited-state dynamics,

respectively [6, 76, 133–135]. However, the interplay of these phenomena that produces the microscopic excited-state dynamics has been inaccessible with traditional methods.

In recent years, a suite of new techniques has appeared for single-molecule ultrafast measurements [136, 137]. Traditional transient absorption spectroscopy has been integrated into a microscope and applied to supramolecular particles with large oscillator strength, such as carbon nanotubes [138]. However, for smaller particles, including single copies of molecular or biological systems, an increase in sensitivity beyond traditional transient absorption is required. This has been achieved in two ways: (1) complex detection electronics [139, 140]; and (2) mapping the ultrafast dynamics onto fluorescence, which can be detected with low background through spectral filtering [141–143]. The latter is implemented by combining ultrafast pulses with confocal detection and does not require complex electronics, thus providing a more straightforward way to achieve single-particle sensitivity for fluorescent systems.

In studies of photosynthetic light harvesting, fluorescence-based approaches build on the intrinsic fluorescence of photosynthetic proteins, making these the natural choice. The van Hulst group has pioneered single-molecule, fluorescence-detected ultrafast spectroscopy [142–144]. They have observed heterogeneity in vibrational coherence in dyes and electronic coherence in photosynthetic proteins [144]. However, in photosynthetic solar energy conversion, it is the energy and electron transfer rates that are the key parameters, and so van Grondelle and co-workers used this experiment to measure an energy transfer step in the bacterial light-harvesting complex, LH2 [145], uncovering a distribution of rates. While these pioneering experiments demonstrated the feasibility and promise of this approach, their apparatus was unable to span the visible region. Photosynthetic systems absorb across the visible to capture sufficient energy to meet their needs, and so investigation across these regions is required. Here, we repurpose and redesign fluorescence-based single-molecule ultrafast spectroscopy to produce an apparatus that can straightforwardly measure single-molecule, excited-state dynamics across the visible.

Chapter 2

Single-Molecule Pump-Probe Spectroscopy

Adapted from: Moya R., Kondo T., Norris A., & Schlau-Cohen, G. S. "Spectrally-tunable femtosecond single-molecule pump-probe spectroscopy" *Opt. Express* **18**, 28246 – 28256 (2021).

2.1 Chapter Summary

Single-molecule spectroscopy has been extensively used to investigate heterogeneity in static and dynamic behaviors on millisecond and second timescales. More recently, single-molecule pump-probe spectroscopy emerged as a method to access heterogeneity on the femtosecond and picosecond timescales. Here, we develop a single-molecule pump-probe apparatus that is easily tunable across the visible region and demonstrate its utility on the widely-used fluorescent dye, Atto647N. A spectrally-independent, bimodal distribution of energetic relaxation time constants is found, where one peak corresponds to electronic dephasing ($\sim$ 100 fs) and the other to intravibrational relaxation ($\sim$ 300 fs). The bimodal nature indicates that relaxation within each individual molecule is dominated by only one of these processes. Both peaks of the distribution are narrow, suggesting little heterogeneity is present for either process. As illustrated here, spectrally-tunable single-molecule pump-probe spectroscopy will enable

investigation of the heterogeneity in a wide range of biological and material systems.

2.2 Introduction

Ensemble transient absorption spectroscopies are routinely used to explore the excited-state dynamics in a wide range of condensed phase systems [146–152]. Analysis and separation of the contributions to spectral broadening in ensemble measurements have established that the presence of nano-environments within these systems give rise to the sub-populations, which collectively determine the material properties [153, 154]. With the advent of single-molecule spectroscopy, these sub-populations have been explored directly, and photophysical heterogeneity has been observed [6, 147, 155, 156]. However, traditional single-molecule techniques lacked the femtosecond temporal resolution required to investigate the heterogeneity in the excited-state dynamics.

In recent years, a suite of new techniques has appeared to probe femtosecond dynamics for sub-populations. Transient absorption microscopy interrogates micron-scale regions of a sample or a single nanostructure [146–151]. While these methods have revealed heterogeneity in solid materials such as graphene or perovskites [148–151, 157], transient absorption measurements rely on a nonlinear signal, and so the region interrogated must produce large signals and be highly photostable [147]. As a result, these techniques have not been used on single molecules or proteins. Single-molecule pump-probe spectroscopy (SM2P) is an alternative approach that modulates the fluorescence emission to access femtosecond dynamics of single fluorescent particles. SM2P incorporates two ultrafast excitation pulses into a single-molecule confocal microscope and the level of fluorescence emission depends on the delay between the pulses [41, 141, 158]. This technique has been used to investigate vibrational relaxation and to coherently control excited state populations in single pigments and to observe coherent wavepacket oscillations and characterize energetic relaxation in photosynthetic light-harvesting complexes [143, 145, 159]. SM2P, therefore, has the sensitivity required to investigate molecules and proteins at the single-molecule level.

Herein, we introduce a spectrally tunable version of SM2P that allows facile ex-

ploration of excited-state dynamics across the visible range. Whereas previous SM2P apparatuses were tuned via the Ti:Sapphire gain curve, the introduction of a fiber laser extends the measurement down to 450 nm, spanning the visible region of the spectrum. Furthermore, the simple turn-key operation of the fiber laser combined with the incorporation of single-prism compression enables easy alignment. We demonstrate the utility of the apparatus on the widely-used single-molecule dye, Atto647N, and observe spectrally-independent energetic relaxation. A bimodal distribution of relaxation time constants is observed, which shows two processes are present on the timescales interrogated and that relaxation in an individual molecule is dominated by one of these processes. We assign the two peaks to electronic dephasing on a 100 fs timescale and intravibrational relaxation on a 300 fs timescale, based on previous work [41, 141, 158]. Both peaks are narrow, which indicates little molecule-to-molecule variation likely due to the homogeneity of the solution-phase environment. Detailed simulations of SM2P data characterized the influence of Poissonian noise the measured distributions. Collectively, these results determined the heterogeneity in energetic relaxation for Atto647N, and laid the groundwork for studies of the spectral dependence of heterogeneity in material and biological systems across the visible region.

2.3 Theory of the experiment

SM2P relies on an isoenergetic 2 pulse pump-probe like excitation in the saturating regime where the laser is exclusively resonant with a higher-lying excited state [141, 145, 158]. As shown in Figure 2-1 (left and right), the sample can be modeled as a three-level system where the first saturating pulse generates damped Rabi oscillations between the ground state and higher-lying excited state that, in the long-time limit of our pulse duration ($\sim$100 fs), is equilibrated to the same probability of the molecule being in either state. As the delay increases, the population in the higher-lying excited state increasingly relaxes to the off-resonant state. The second pulse then re-equilibrates the population remaining in the higher-lying state with that in the

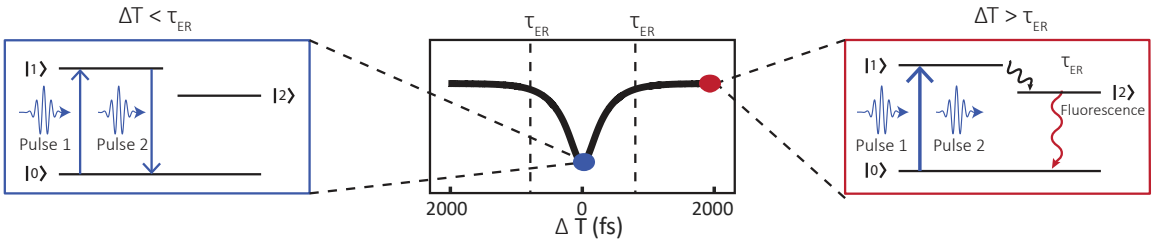

Figure 2-1: **Single-molecule pump-probe spectroscopy.** Two laser pulses are focused onto the sample where energy relaxes between two excited states (a donor, $|1\rangle$, and an acceptor, $|2\rangle$) with a timescale, τ_{ER}. If ΔT is less than τ_{ER} (left), pulse 2 stimulates emission, decreasing the fluorescence intensity. If ΔT is greater than τ_{ER} (right), fluorescence emission occurs, increasing the fluorescence intensity. Scanning the time delay from negative to positive delays produces a dip like shape (middle) where the width of the modulation is governed by τ_{ER}.

ground state, which increases the probability of population for a depleted higher-lying state. Due to its narrow bandwidth, the pulse does not interact with the off-resonant state. The re-equilibrated population of the higher-lying excited state continues to undergo relaxation into the off-resonant state, from which it eventually fluoresces on a nanosecond timescale. Due to the proportionality between the population of the off-resonant state and the detected fluorescence, when the delay is scanned from negative to positive delay times, a dip-like shape is seen in the fluorescence emission (Figure 2-1 middle), which can be fit to extract the time constant of relaxation from the higher-lying excited state to the off-resonant state.

2.4 The Experimental Set-up

A schematic of the experimental setup is shown in Figure 2-2. A tunable fiber laser (FemtoFiber pro, Toptica; ∼100 fs pulse duration, ∼4 nm bandwidth, 80 MHz repetition rate) that spans the visible spectrum was used for the experiment. Due to the high powers required for saturating excitation, the single chromophores quickly photobleached, which appeared as a permanent reduction of the fluorescent intensity to the background level (40 Hz). To reduce the effects of photobleaching, the laser repetition rate was reduced from 80 MHz to 312.5 kHz with an acousto-optic pulse picker (Brimrose Corporation, FSPP-400-80-BR-800). The selected repetition rate

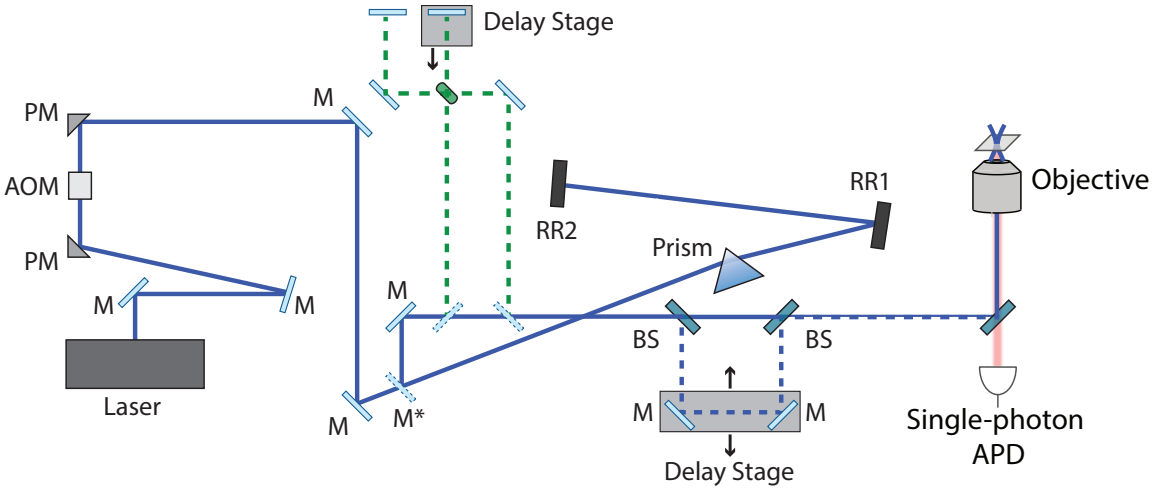

Figure 2-2: **Experimental set-up for single-molecule pump-probe spectroscopy** Schematic of the apparatus shows the femtosecond fiber laser excitation source focused and collimated by a set of parabolic mirrors (PM) into an acousto-optic modulator (AOM), which is used as a pulse picker to reduce the repetition rate. The pulse is compressed by a single-axis prism compressor paired with two retroreflectors (RR1 and RR2) before traveling through a set of beam splitters (BS) and a delay stage in a Mach-Zehnder configuration. The horizontal polarization is converted to right handed polarization by a quarter-waveplate ($1/4\lambda$) before being focused to a diffraction limited spot by the objective. The emission is collected through the same objective, filtered by a dichroic mirror (DM) to remove the excitation light, and focused onto a single-photon avalanche photodiode (APD). The dashed green line shows an optional path with another BS and a more precise delay stage (Newport Picomotor Actuator Model 8302 with stage Model 9067-COM-E, minimum step size: 80 nm) introduced using removable magnetic mirror mounts (MM1 and MM2) to record the interferometric autocorrelation.

was the lowest available with the pulse picker, which led to the longest period before photobleaching.

A single-axis prism compressor was set to minimize dispersion effects from the high NA objective at the sample position[160], which allows straightforward optimization of the compression for different wavelengths. The pulse duration was measured by interferometric autocorrelation (IAC) using a GaP photodiode (Marktech, MTPD3650D-1.4) at the sample position [161, 162]. The dashed green lines in 2-2C show the optical path for the autocorrelation measurements. To achieve the step size required for interferometric measurements in the visible region, the autocorrelation was performed with a dedicated translation stage (Newport Picomotor Actuator

Model 8302 with stage Model 9067-COM-E, minimum step size: 80 nm). The differential dispersion in the two arms due to the beamsplitter (Thorlabs, UFBS5050) was neglected because it only adds $\sim$500 fs^2 of group delay dispersion at 610 nm. The additional dispersion would extend a pulse of 100 fs to 101 fs, which can be ignored for the reported measurements. Sample IACs are shown in Figure 2-3 for 610nm (a,b; compressed 118 fs, c,d; uncompressed 180 fs) and 645 nm (e,f; uncompressed 303 fs). The intensity autocorrelations (b, d, f) were extracted by Fourier transforming the IAC and filtering out the coherent oscillations. The intensity autocorrelations were fit assuming a Gaussian envelope [131]. All data manipulation was completed in Matlab. Replicate autocorrelation measurements found 95% confidence intervals to be within $\sim$10% of the mean value.

The laser pulses were split by a set of beamsplitters (Thorlabs, UFBS5050) and a delay stage (Newport ISL100CC, minimum step size: 1 μm) in a Mach-Zehnder interferometer. To prevent dipole orientation dynamics from affecting the experiment, the laser exication was converted to circular polarization using a zeroth order quarter-waveplate (Newlight Photonics, WPM03-Q-VIS). The pulse pairs were coupled into an inverted confocal microscope (Mad City Labs, Stage Model Nano-LP100) and focused onto the sample with an objective (UPLSAPO100XO, Olympus, NA 1.4). Emission was isolated through the combination of a dichroic mirror determined by excitation wavelength (Chroma, T635lpxr-UF3; Chroma, ZT647rdc-UF2)) and two bandpass filters (Semrock, FF02-675/67-25; Chroma, ET690/120x). An avalanche photodiode (SPCM-AQRH-15, Excelitas) with a time-correlated single photon counting module (TimeTagger20, Swabian Instruments) was used to detect the fluorescence photons and had an instrument response function of $\sim$0.5 ns for fluorescence lifetime experiments.

Atto647N (ThermoFisher, 04507-1MG-F) was initially diluted in DMSO and then diluted in water to a final concentration of $\sim$ 500 pM in solution that was 1% polyvinyl alchohol. An enzymatic oxygen-scavenging system was added to the solution at final concentrations of 25 nM protocatechuate-3,4-dioxygenase and 2.5 mM protocatechuic acid [163, 164]. 50 μL of the solution was spin-coated onto glass coverslips. This

concentration gave rise to about one molecule per square micron.

For SM2P experiments the power was set to ∼1 pJ per pulse at the sample plane. The center wavelength of the laser was tuned to either 610 nm or 645 nm with a focal spot FWHM of ∼350 nm at the sample plane. For the 610 nm measurements, experiments were performed with near-transform limited temporal compression (118 fs). For the 645 nm measurements, experiments were performed with no temporal compression (300 fs) due to power limitations via bypassing the prism compressor.

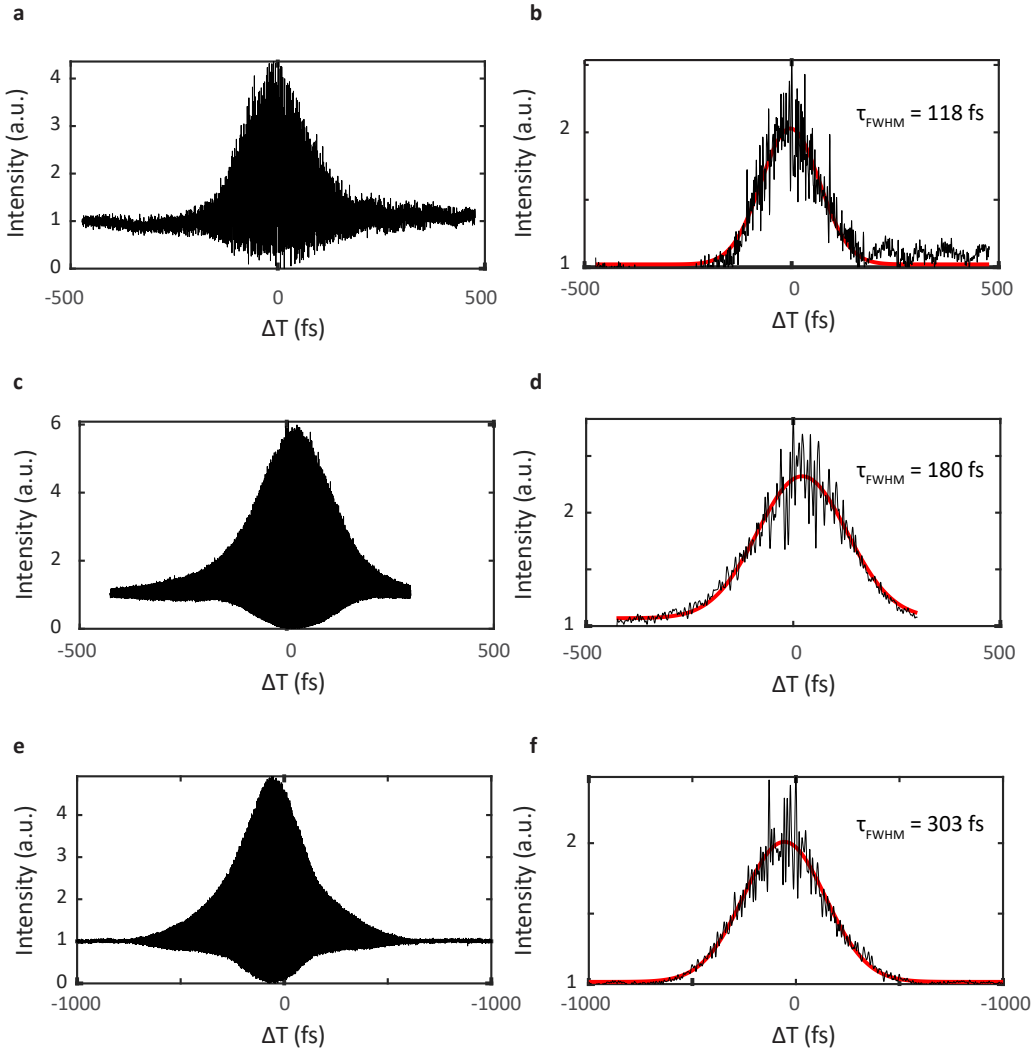

Figure 2-3: **Interferometric autocorrelation of excitation pulses.** Interferometric autocorrelations are shown in (**a**, **c**, **e**) for compressed 610 nm excitation, uncompressed 610 nm excitation, and uncompressed 645 nm excitation, respectively. Corresponding intensity autocorrelations with fits are shown in (**b**, **d**, **f**). The insets list the FWHM of the excitation puless assuming a Gaussian envelope.

The delay time between pulse pairs was scanned from -1.5 ps to 1.5 ps at 100 μm/s ($\sim$300 ps/s). Although the FWHM of the 645 nm pulse was 300 fs, theoretical work has shown that the strong interaction in the presence of saturating laser pulses improves the temporal resolution [165–167]. For example, previous SM2P measurements recovered timescales as short as one sixth of the FWHM [145].

Fluorescence emission was binned at 50 ms intervals, which gives a data point every $\sim$30 fs. Photobleaching appears as a permanent reduction of fluorescence intensity down to background levels. Analysis was limited to molecules that photobleached after completion of the full SM2P trace ($\sim$4 s). Single molecules also exhibit fluorescence intermittency and blinking due to local conformational and environmental changes [168–170]. Intermittency appears as a change in the fluorescence intensity and molecules that exhibited intermittency were removed from further analysis. Blinking appears as a brief ($<$50 ms) reduction of the intensity down to background levels. The time point corresponding to the blinking event was not included in the fitted data, *i.e.*, points identified as blinking events did not contribute to the error function that was minimized to extract relevant timescales. A blinking event was observed in $\sim$10% of molecules. The binned data was fit to the convolution of the measured intensity autocorrelation with an exponential rise [145]. A small fraction ($\sim$5%) of SM2P traces were collected on a previously-measured molecule, but the fraction was not sufficient for statistically robust independent analysis.

2.5 Simulations of SM2P experiment determine effects of Poissonian noise

To aid in the interpretation of SM2P data, simulated traces were generated in MATLAB. A simple three-level system was used as shown in Figure 2-1. In the saturating limit and where the pulses are longer than the dephasing time, the population of the states in the three-level system can be described by the following differential equations [141, 145, 158]:

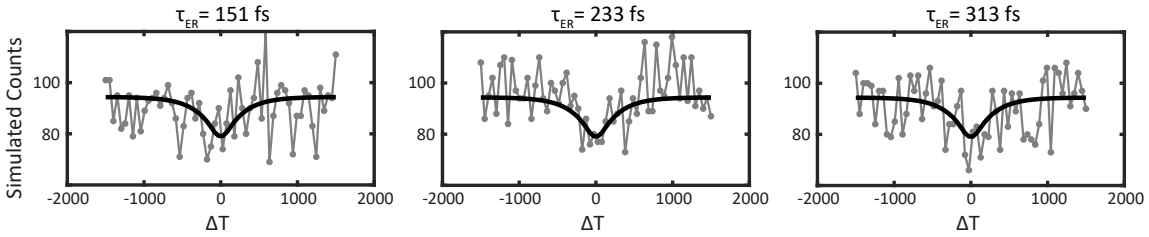

Figure 2-4: **Simulated SM2P traces.** Representative traces with an input of $\tau_{ER,\mathrm{sim}}$ = 250 fs where the τ_{ER} extracted from the fit is shown above. Variation from the input time constant is introduced by Poissonian noise

$$\frac{\partial N_0}{\partial t} = -k_L(N_0 - N_1) + k_f N_2, \tag{2.1}$$

$$\frac{\partial N_1}{\partial t} = k_L(N_0 - N_1) - k_{ER} N_1, \tag{2.2}$$

$$\frac{\partial N_2}{\partial t} = k_{ER} N_1 - k_f N_2. \tag{2.3}$$

Where N_0, N_1, and N_2 are the population of $|0\rangle$, $|1\rangle$, and $|2\rangle$, respectively, k_L is the rate of absorption/stimulated emission, k_f is rate of fluorescence, and k_{ER}, *i.e.* $\frac{1}{\tau_{ER}}$, is the rate of energetic relaxation. Note that $k_f \approx 0$ because fluorescence occurs on a much longer timescale (ns) than energy redistribution and $k_L = \alpha I(t, \Delta\mathrm{T})$ where α is the absorption cross section and $I(t, \Delta\mathrm{T})$ is the intensity profile of the two pulse laser excitation with time delay ΔT. In practice, the pulsed excitation was modeled as a Gaussian with a FWHM of 150 fs and the amplitude of the Gaussian pulses were set to one. k_L was then increased by varying α until saturation was obtained, which was determined by monitoring the value at which the probability of N_1 became 50% under a single pulse excitation. For a specific time delay (ΔT), equations 1-3 are numerically integrated to simulate system dynamics observed through the population of N_2, which is directly proportional to the observed fluorescence. By controlling the time delay between the excitation pulses, we generate a fluorescence curve comparable to the one obtained experimentally and the fit function was used to extract the simulated time constants.

The finite photon budget of a single molecule limits the signal-to-noise ratio (SNR) of SM2P data. The observed fluorescence intensity ($\mathrm{I_{fl}}$) of our SM2P experiments is

$\sim$100 photons/50 ms. The theoretical modulation depth of 33% [141, 145] means that the signal is $\sim$33 photons/50 ms. Due to the stability of the laser and microscope, the dominating contribution to noise is Poissonian fluctuations in the number of detected photons, given by $\sigma_{\mathrm{fl}} = \sqrt{\mathrm{I}_{\mathrm{fl}}}$ =10 photons/50 ms. Collectively, these values yield a SNR of $\sim 3:1$. Although the SNR could be improved with further averaging, the acquisition time is limited by rapid photobleaching due to the saturating power used in our experiment.

The ability to extract the underlying parameters was investigated by simulating traces with typical levels of Poissonian noise and fitting them in the same manner as the experimental data to extract energetic relaxation time constants. Representative simulated traces for a $\tau_{ER,\mathrm{sim}}$ of 250 fs are shown with their fit values in Figure 2-4. The presence of Poissonian noise can distort the fit, which, as illustrated here, gives rise to variation in the extracted time constants. To quantify the variation, the simulation was repeated 100 times for a range of energetic relaxation time constants. First, single time constants of $\tau_{ER,\mathrm{sim}} = 150$ fs, $\tau_{ER,\mathrm{sim}} = 250$ fs, and $\tau_{ER,\mathrm{sim}} = 500$ fs were investigated. These time constants were selected to span the pulse duration (150 fs) to the energetic relaxation time constants (500 fs) observed in molecular systems [171]. For each time constant, histograms were constructed from the values extracted by fitting the simulated traces (Figure 2-5A–C). The medians of the histograms recovered the time constants with relatively high fidelity. The histograms had standard deviations of $\sim$100–200 fs and little dependence on the value of the time constant itself was observed in this regime (7 fs per 100 fs; see Supplementary Information Figure 2-8). These standard deviations reflect narrow distributions as expected for single time constant simulations.

To investigate the ability of SM2P to characterize the distribution of behaviors, simulations were performed for single time constants randomly drawn from a Gaussian distribution. Specifically, a fixed central value of $\tau_{ER,\mathrm{sim}} = 250$ fs was used with σ_{sim} values of 25, 100, and 400 fs. Histograms of the resulting simulations are shown in Figure 2-5D – F. For distributions narrower than the $\sim$125 fs width from Poissonian noise alone (Figure 2-5 D, E), the width remains similar and no additional information

is extracted. For distributions wider than the width from Poissonian noise (Figure 2-5F), both the median and the width are affected.

Lastly, to investigate the ability of SM2P to extract multiple time constants, simulations were performed for two components. The timescale was randomly selected from two Gaussian distributions with the specified mean values and a standard deviation of 25 fs for each one. Figure 2-5G –I shows the influence of the presence of two components with equal amplitudes on the distribution. The extracted median value is an accurate average of the two time constants. With a 350 fs and 250 fs separation (Figure 2-5G and H, respectively), the bimodal nature of the distribution is clear. However, for a 150 fs separation, the two time constants are too close to resolve, and the distribution is similar to one for a single time constant (*e.g.*, Figure 2-5C), with the median shifted towards slightly shorter values. Collectively, these results suggest that multiple components closer than 150 fs cannot be resolved, while those further apart could be separable, depending on the heterogeneity in the time constants themselves.

Figure 2-5J –L shows the influence of the presence of two components with varying amplitudes on the distribution for time constants with a 350 fs separation. When the two components had amplitudes of 70%/30% (Figure 2-5J,K), the distribution appeared asymmetric, although with significant population at both timescales. However, for amplitudes of 90%/10% (Figure 2-5L), the distribution peaked around the dominant timescale, and it would be difficult to reliably extract information about the minor component.

2.6 Energetic Relaxation in Atto647N

We used SM2P to investigate ultrafast excited-state relaxation in Atto647N, a photostable fluorophore widely used in single-molecule imaging. The absorption and fluorescence spectra of Atto647N are shown in Figure 2-6A along with the laser spectra. Excitation at 610 nm and 645 nm was chosen to isolate the effects of energy relaxation in the main peak and the vibronic side band. Representative SM2P traces

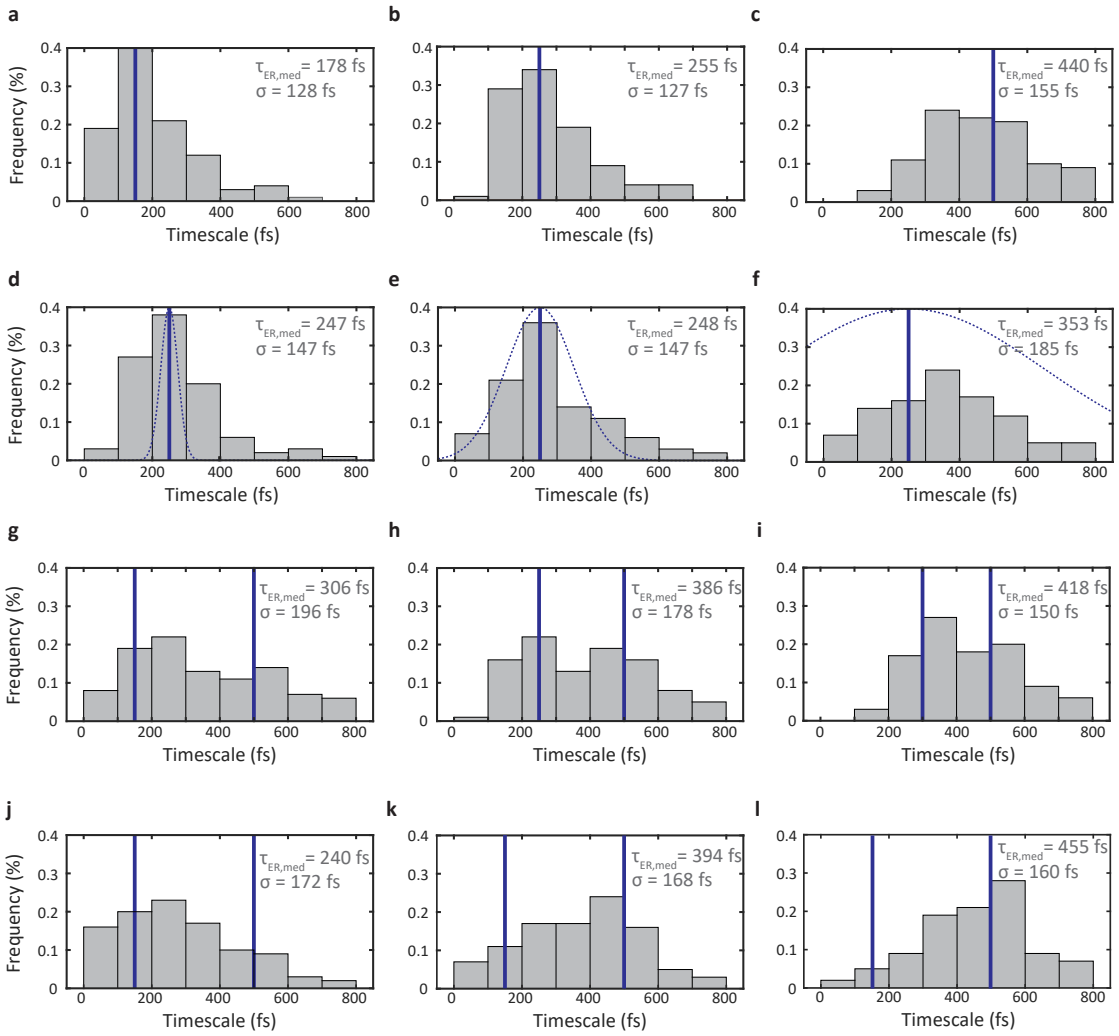

Figure 2-5: **Distribution of energetic relaxation time constants for simulated SM2P traces.** SM2P experiments were simulated using the input values plotted in blue of single time constants of 150 fs (a), 250 fs (b), and 500 fs (c); Gaussian distributions (dashed) around a center time constants of 250 fs with standard deviations of 25 fs (d), 100 fs (e), and 400 fs (f); two time constants with equal amplitude of 150 fs and 500 fs (g), 250 fs and 500 fs (h), and 350 fs and 500 fs (i); and for two time constants of 150 fs and 500 fs with amplitudes of 70% and 30% (j), 30% and 70% (k) and 10% and 90% (l). The extracted parameters from the distribution are shown in the upper right corner of each panel and listed in Table 2.2 in the Supplementary Information.

are shown in Figure 2-6B and C for an excitation wavelength of 610 nm and in Figure 2-6D and E for a wavelength of 645 nm. To extract the energetic relaxation time constant, each trace was fit using a maximum likelihood estimation algorithm, which is more robust in the presence of noise as it includes a specific noise model.

The observed Fisher information matrix was calculated and is directly related to the variance of our parameter estimation and asymptotically approaches the Cramér-Rao lower bound [172]. The standard error in the extracted time constants is determined through this variance and is generally less than 50 fs.

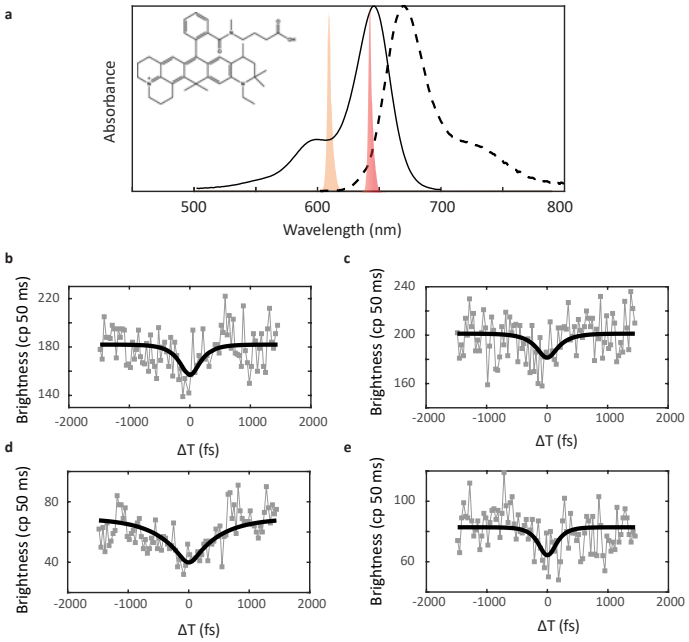

Figure 2-6: (a) Absorption (solid) and fluorescence (dashed) spectra of Atto647N are shown with the chemical structure in inset. The laser pulses are overlaid (λ_c=610 nm, orange; λ_c=645 nm, red). Representative SM2P traces are shown for 610 nm excitation with values of 182±43 fs and 197±19 fs in (b) and (c), respectively, and for 645 nm excitation with values of 466±43 fs and 142±25 fs in (d) and (e), respectively.

2.6.1 Components of the energetic relaxation in Atto647N

SM2P traces on individual Atto647N were successfully performed 52 and 78 times for 610 nm and 645 nm excitation, respectively. To determine the distribution of energetic relaxation time constants, the extracted values were used to construct the histograms shown in Figure 2-7. The histograms show a sharp peak and tail extended towards longer time constants, consistent with previous SM2P work [141, 158]. The histograms were fit using a Gaussian mixture model in which two components were required to capture both the peak and the tail (Table 2.1). Gaussians were used

as the simplest functional form that agreed with the measured distributions. The solution environment of Atto647N likely leads to multiple uncorrelated interactions between the dye and the surrounding molecules, which the central limit theorem predicts would lead to a Gaussian distribution. In environments where single interactions dominate, other distributions, such as an exponential Gaussian or a Gamma distribution, would be more appropriate and could better connect the skewed data to a physical phenomenon. We focus on the time constants extracted from the Gaussian mixture model, because the analysis was empirically found to more accurately and reproducibly extract the center values of the components as compared to the widths or standard deviations. The fit found a ∼115 fs time constant for the peak and ∼325 fs time constant for the tail. The ability of the 645 nm laser pulse to approximately measure the fast time component was confirmed using simulated data (see Supplementary Information Figure 2-9).

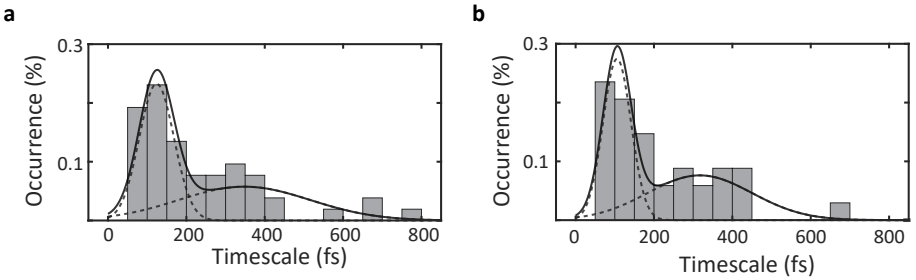

Figure 2-7: Spectral independence of Atto647N energetic relaxation time constants. Histograms of energetic relaxation time constants were constructed for excitation at (A) 610 nm (N= 52) and (B) 645 nm (N=78). The histograms were fit (solid) with a two component Gaussian mixture model (dashed lines).

Table 2.1: Mean (μ), standard deviation (σ), and amplitude (A) from a two-component Gaussian mixture model fit of the energetic relaxation time constants for Atto647N.

	λ_{exc} = 610 nm		λ_{exc} = 645 nm	
Component	1	2	1	2
μ (fs)	124	348	105	317
σ (fs)	44	168	35	133
A	48	52	49	51

2.6.2 Interpretation of ultrafast time constants

We now consider the likely molecular origin of the two measured components. One-color SM2P spectroscopy measures the collective timescale of the dynamics through which the excited state moves out of resonance with the laser pulse. Previous ensemble ultrafast measurements extensively characterized the early timescale molecular dynamics, which can be divided into inertial solvation, diffusive solvation, and intramolecular vibrational relaxation (IVR) to non-optically coupled modes [171, 173, 174]. Inertial solvation is the fast timescale ($\sim$100 fs to 600 fs) response by individual solvent molecules to the new excited state and its dynamics. Diffusive solvation is the longer timescale ($\sim$ ps) collective reorganization of the solvent into a pseudo-equilibrium around the new excited-state electronic structure. While diffusive solvation occurs on timescales outside of the range of our experiment, inertial solvation contributes to the energetic relaxation time constants measured in SM2P. The final contribution is electronic dephasing due to the random fluctuations of the electronic transition energy known to occur in condensed phase systems [142, 159, 175]. Electronic dephasing occurs on a 50 to 100 fs timescale and can be modeled using the Bloch equations under pulsed excitation [159].

The histograms generated from the measured time constants include all of these contributions, which are well-described with two components (Figure 2-7, Table 2.1). We assign the fast component ($\sim$ 100 fs) to contributions from electronic dephasing and the slower ($\sim$ 350 fs) component to a combination of inertial solvation and IVR. Previous experiments have shown an inertial-like response comes from coupled phonon modes in supercooled liquids[174], and similar effects may be present in the polymer matrix used here. Notably, the presence of two components in the single-molecule data suggests that each individual molecule is dominated by one of these components, potentially due to the composition of the neighboring polymer environment for each immobilized dye. The width of each component is narrow, with standard deviations consistent with the simulations of a single-value energetic relaxation time constant (Figure 2-5), and thus is likely primarily due to Poissonian noise. The extracted

standard deviations, therefore, suggest relatively homogeneous timescales, *i.e.*, little molecule-to-molecule heterogeneity, in electronic dephasing, solvation, and IVR.

2.6.3 Spectral independence of energetic relaxation in Atto647N

To investigate the spectral dependence of energetic relaxation, SM2P measurements were performed for both the main peak (0-0 transition) and the vibronic shoulder (0-1 transition) with excitation at 645 nm and 610 nm, respectively. Histograms were constructed for both excitation conditions (Figure 2-7A, B) and comparison of the distributions gives a p-value of 0.14, reflecting no statistically significant differences. Consistently, the values extracted from the Gaussian mixture model fit (Table 2.1) are similar. The lack of spectral dependence is comparable to ensemble ultrafast measurements on bodipy dyes as well as in theoretical models of solvation [171, 173, 174, 176, 177]. Although with the similarity in the random fluctuations that give rise to electronic dephasing, the contribution of IVR must also be spectrally independent. This suggests that relaxation pathways for the two excitation energies relies on a similar set of vibrational modes within the molecule or in the solvent.

2.7 Conclusion

In this work we developed a spectrally tunable version of SM2P, a technique that accesses the ultrafast dynamics of single emitters, and applied it to a widely-used fluorescent dye, Atto647N. These experiments revealed multi-timescale relaxation within the fluorophore with heterogeneity less than the Poissonian noise, suggesting the time constants of the early-time processes are insensitive to the local environment. While here we focused on spectral tunability, the quality of the SM2P data is also limited by the number of detected photons. In future versions of the experiment, the signal level could be improved through the addition of a second collection objective, incorporation of a cryostat for low temperature measurements, and/or detectors with improved quantum efficiency, such as those recently-developed using carbon nanotubes [178].

The versatility of our SM2P set-up allows for investigation into the distribution

of energetic relaxation time constants for a multitude of optical systems. While the high fluences and multiple excitation cycles required for SM2P limit studies to systems that are photostable, there are multiple biological and material systems that meet this criterion, including fluorescent proteins, molecular aggregates, and quantum dots. For multi-choromophoric systems, processes such as exciton-exciton annihilation may lower the detected signal level [179], however, SM2P has been demonstrated on samples of this type. Indeed, the expanded spectral range will enable studies of photosynthetic proteins from many different species, such as the light-harvesting complexes from plants.

2.8 Supplementary Information

2.8.1 Derivation of fit function

The final solution used for extracting energy relaxation can be found by convolving the δ pulse solution with the optical pulse autocorrelation as shown previously [141, 145, 158, 180–182]. The δ pulse solution can be found by assuming that the probability of a transition by a single pulse is p. After the first pulse, the population of the initially excited state, N_1, depopulates as

$$N_1 = pe^{-k_{ER}\Delta \mathrm{T}}, \tag{2.4}$$

where k_{ER} is the energy transfer rate to the off-resonant state 2. And ΔT is the time elapsed before the second δ pulse arrives. When the second δ pulse arrives, we must consider both excitation from the ground state and de-excitation from the excited state population that has yet to relax. The population of the off-resonant state, N_2, is not affected by the second pulse. However, after the second pulse, the entirety of N_1 will transfer to increase N_2, and eventually fluoresce. After the second

pulse, the ensuing population is given by

$$\begin{aligned} N_2 =& \{\text{prob. of energy transfer before pulse 2}\} \\ &+ (\text{prob. of excitation})(\text{prob. in ground state}) \\ &+ (\text{prob. not de-excited})(\text{prob in excited state}),\ \textit{i.e.} \end{aligned} \tag{2.5}$$

$$N_2 = \{p - pe^{-k_{ER}\Delta\mathrm{T}}\} + p(1-p) + (1-p)(pe^{-k_{ER}\Delta\mathrm{T}}), \tag{2.6}$$

which reduces to

$$N_2 = -p^2 e^{-k_{ER}\Delta\mathrm{T}} + (2p - p^2). \tag{2.7}$$

Because N_2 is directly proportional to the fluorescence, this equation represents the fluorescence as a function of time delay between the two pulses, $I(\Delta\mathrm{T}) \propto N_2(\Delta\mathrm{T})$. This representation correlates with the framework used by the van Hulst group where $I_{dip} = I(\Delta T = 0)$ and $I_{long} = I(\Delta T = \infty)$ [141, 158].

$$I(t) = (I_{dip} - I_{long})e^{-k_{ER}|\Delta\mathrm{T}|} + I_{long}. \tag{2.8}$$

The solution for Gaussian pulse excitation is given by the convolution of the autocorrelation of Gaussian pulse with the δ pulse excitation solution [180–182]. This is most easily written as

$$I(\Delta\mathrm{T}) \propto \int AC(t - \Delta\mathrm{T})N_2(t)dt, \tag{2.9}$$

where

$$AC(\Delta\mathrm{T}) = \int f(t)f(t - \Delta\mathrm{T})d\Delta\mathrm{T}. \tag{2.10}$$

is the pulse autocorrelation for Gaussian pulses $f(t) = \frac{\sqrt{2}}{d\sqrt{\pi}}e^{\frac{-2t^2}{d^2}}$ with an adjusted pulse FWHM given by $d = \frac{d_{fwhm}}{\sqrt{2ln(2)}}$.

Plugging these terms into Equation 1.7 leads to the equation reported by the van Grondelle group [145]:

$$I(\Delta \mathrm{T}) \propto$$
$$I_\infty \left(1 - \frac{p}{2-p}\frac{1}{2} e^{\frac{k_{ER}^2 d^2 \Delta \mathrm{T}}{4}} \left(e^{-k_{ER}\Delta \mathrm{T}} erfc\left(\frac{d^2 k_{ER} - 2\Delta \mathrm{T}}{2d}\right) + e^{k_{ER}\Delta \mathrm{T}} erfc(\frac{d^2 k_{ER} + 2\Delta \mathrm{T}}{2d}\right)\right)\right). \tag{2.11}$$

There are three fit parameters in equation S8: the baseline intensity, I_∞, the probability of excitation by a single pulse, p, and the energy transfer rate, $k_{ER} = \frac{1}{\tau_{ER}}$. This function (equation 1.9) was fit through a custom Matlab program that minimized the negative log-likelihood function (LL), below, where M_i represents the counts predicted by the model and C_i represents the experimental counts detected [183].

$$-LL = -2\sum_i (C_i - M_i) + C_i \; log\left(\frac{M_i}{C_i}\right). \tag{2.12}$$

2.8.2 Weak dependence of distribution due to Poissonian Noise

To investigate the effect of Poissonian noise, 100 traces with a fixed τ_{ER} were simulated as described in the main text for various timescales in our experimental regime. The widths of the resulting distribution, measured through the standard deviation statistic, were then calculated and showed a weak linear dependence on the input τ_{ER} (Figure 2-8). A Pearson's coefficient of 0.90 was found suggesting a positive relationship. A linear fit gave a slope of 0.07, corresponding to an increase in standard deviation of about 7 fs for every 100 fs. This dependence will be minor over the experimentally measured range.

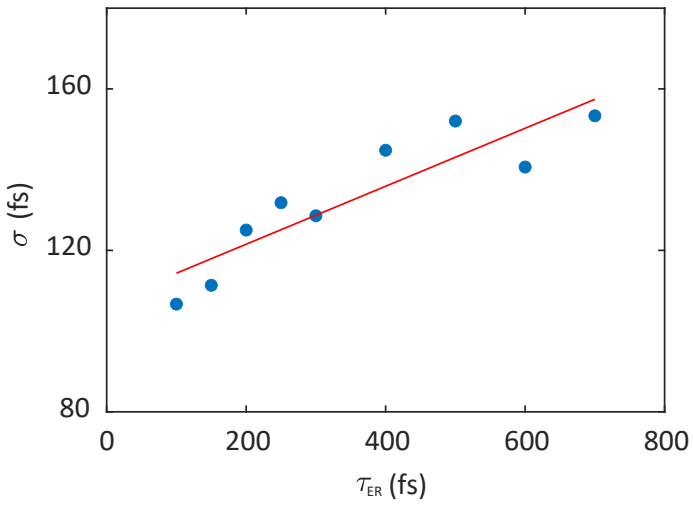

Figure 2-8: Blue points indicate the measured standard deviation from our simulations of 100 traces with Poissonian noise. The red line indicates the linear fit that shows a weak linear dependence.

2.8.3 Simulation Parameters

	$\tau_{ER,sim}$ fs	$\tau_{ER,med}$ fs	σ fs		$\tau_{ER,sim}$ fs	σ_{sim} fs	$\tau_{ER,med}$ fs	σ fs
A	150	178	128	**D**	250	25	247	147
B	250	255	127	**E**	250	100	248	147
C	500	440	155	**F**	250	400	353	185

	$\tau_{ER,sim,1}$ fs	$\tau_{ER,sim,2}$ fs	$\tau_{ER,med}$ fs	σ		A_{150} %	A_{500} %	$\tau_{ER,med}$ fs	σ fs
G	150	500	306	196	**J**	70	30	240	172
H	250	500	386	178	**K**	30	70	394	168
I	350	500	418	150	**L**	10	90	455	160

Table 2.2: Data from the energy transfer timescale simulations in Figure 4. Blue text headers indicate input parameters for simulations while black text headers indicate the parameters extracted from the simulations.

2.8.4 Effect of pulse duration on fast timescales

We characterized the precision of the measured timescales in the regime in which the pulse duration is longer than the energetic relaxation, which has been established theoretically to be accessible in SM2P measurements [145, 165–167]. Simulations were performed for Gaussian pulses with a FWHM of 300 fs and an energetic relaxation timescale of 100 fs. The resulting distribution is shown in Figure 2-9, and an energetic relaxation timescale of 137 fs was extracted. Simulations were completed using the same methods described in Section 2.5.

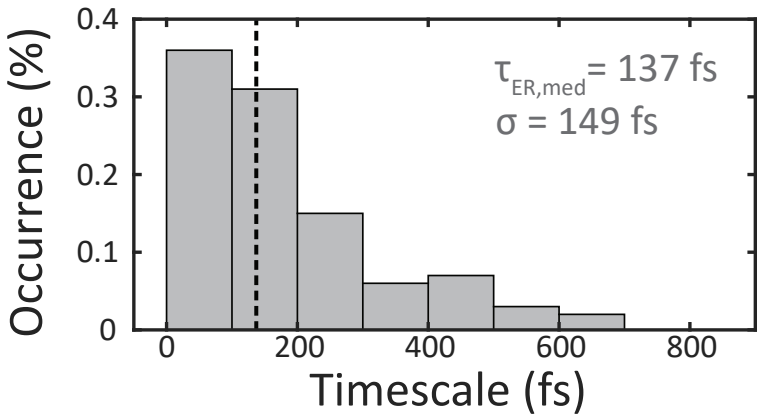

Figure 2-9: Distribution of energetic relaxation timescales for an SM2P simulation with an energetic relaxation timescale of 100 fs and an optical pulse of a Gaussian envelope with a FWHM = 300 fs. The distribution reveals the dominant population is around 100 fs and has a median of 137 fs, indicated by the dashed vertical line.

Chapter 3

Heterogeneous Ultrafast Dynamics in Photosynthetic Proteins from Cyanobacteria

Adapted from: Moya R., Norris A., Kondo T., & Schlau-Cohen, G. S. "Observation of robust energy transfer in the photosynthetic protein allophycocyanin using single-molecule pump–probe spectroscopy" *Nat. Chem* (2022)

3.1 Chapter Summary

Photosynthetic organisms convert sunlight to electricity with near unity quantum efficiency. Absorbed photoenergy transfers through a network of chromophores positioned within protein scaffolds, which fluctuate due to thermal motion. The resultant variation in the individual energy transfer steps has not yet been measured, and so how the efficiency is robust to this variation, if any, has not been determined. Here, we describe single-molecule pump-probe spectroscopy with facile spectral tuning and its application to the ultrafast dynamics of single allophycocyanin, a light-harvesting protein from cyanobacteria. Using the spectral dependence of the dynamics, energy transfer and energetic relaxation from nuclear motion were disentangled. For energy transfer, an asymmetric distribution of timescales was observed. For energetic relax-

ation, the timescales were slower and more heterogeneous due to the impact of the protein environment. Collectively, these results suggest that energy transfer is robust to protein fluctuations, a prerequisite for efficient light harvesting.

3.2 Introduction

Photosynthetic light-harvesting systems power most life on earth by capturing and directing absorbed energy through networks of protein-scaffolded chromophores [4]. Rapid transfer of the absorbed energy is driven by coupling between the transition dipole moments of the chromophores. Fluctuations of the protein scaffold induce changes in the distances and orientations of the transition dipole moments that can, in turn, change the timescales of energy transfer [9, 16, 19–21, 43]. Despite these fluctuations, energy travels through the light-harvesting systems to reach the reaction center with near-unity quantum efficiency [3, 4]. Heterogeneity in the timescales of energy transfer, *i.e*, the impact of protein fluctuations on light harvesting, has not yet been characterized.

Over the past decades, single-molecule methods have been a powerful approach to characterize heterogeneity in biological, chemical, and material systems, including photosynthetic light-harvesting proteins [6, 147, 155, 156]. More recently, single-molecule pump-probe spectroscopy (SM2P) emerged as a technique to resolve femtosecond processes, such as energy transfer. SM2P maps femtosecond dynamics onto fluorescence intensity using two ultrafast isoenergetic pulses to generate a pump-probe like excitation, where the temporal resolution is from the delay time between pulses (Fig. 3-2a) [136, 141, 145, 158]. This technique has been applied to various ultrafast processes in single molecules, including coherent wavepacket oscillations and relaxation amongst the excitonic states of light-harvesting proteins from purple bacteria [143–145]. Comparison of the exciton relaxation measurements with theoretical calculations found a narrow distribution of chromophore transition energies, enabling robust exciton delocalization and, therefore, robust energy transfer [184]. The complexity of the ultrafast dynamics of the measured light-harvesting protein

has, however, obfuscated the heterogeneity specific to an individual energy transfer step. Furthermore, most of the previous measurements lacked spectral dependence, which provides an additional axis to help disentangle the contributions associated with each process.

The cyanobacterial light-harvesting protein, allophycocyanin (APC), contains strongly coupled dimers of chromophores that serve as a minimal system to examine photosynthetic energy transfer (Fig. 3-1a). Ensemble ultrafast measurements found complex kinetics of energy transfer within APC, potentially due to heterogeneous timescales [49, 86, 185–192]. Consistently, single-molecule fluorescence measurements identified heterogeneous photophysical states that arose from fluctuations of the protein scaffold [193–198], yet their impact on energy transfer could not be resolved due to the limited time resolution of fluorescence measurements.

Here, we report SM2P with facile spectral tuning across the visible region and perform SM2P measurements on APC, the homologous protein C-phycocyanin (CPC), and a chromophore in solution. Based on the spectral dependence of the dynamics and the concomitantly-measured fluorescence lifetimes, distributions were constructed for APC in which the populations were dominated by proteins with energy transfer or by proteins with only energetic relaxation due to nuclear motion. For the distribution with energy transfer, the median of the distribution was $\sim$100 fs shorter than the mean, suggesting that the ensemble values may be lengthened or non-monoexponential due to slow sub-populations. Broad distributions of energetic relaxation timescales were observed for both APC and CPC, which comparison to choromophores in solution indicated arises from the protein structure. Furthermore, slow energetic relaxation was observed in APC, enabling energy transfer to precede, and thus likely be unaffected by, the heterogeneity in the relaxation timescales. Together, these results demonstrate that rapid energy transfer is maintained despite fluctuations of the protein, which may play a role in the high quantum efficiency of photosynthetic light harvesting.

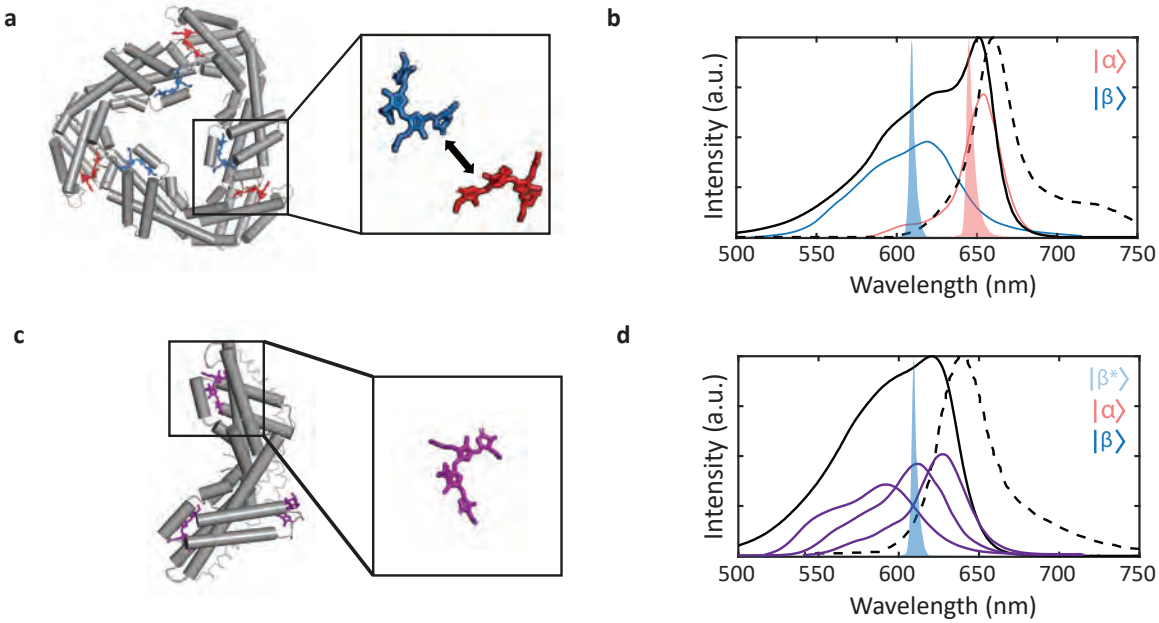

Figure 3-1: **Structure and spectra of phycobilisome subunits.**(a) Structural model of allophycocyanin with the β (blue) and α (red) chromophores (PDBID 1ALL). (b) Absorption (solid) and emission (dashed) spectra are shown with the 610 nm and 645 nm excitation in blue and red, respectively. The individual spectra for the α and β chromophores are shown in blue and red [49]. (c)The structure of C-phycocyanin (Protein Data Bank ID Code 1GH0) is shown with a callout of a tetrapyrole chromophore (purple). (d) The corresponding absorption (solid) and emission (dashed) spectra are shown with the 610 nm excitation shown in blue.

3.3 Results

3.3.1 Ultrafast dynamics in APC

We used SM2P to determine the distribution of ultrafast energetic relaxation timescales in APC. APC forms a trimer where each monomer contains two protein subunits, known as α and β, that each bind a phycocyanobilin chromophore, which are positioned on distal ends of the monomer (∼5 nm apart) [94, 98]. The structural model of trimeric APC is shown in Fig. 3-2b. Upon trimerization, complementary chromophores on different monomers are brought close together (∼2 nm apart) to generate the dimer shown in Fig. 3-2b, inset [94, 98]. The trimers assemble into the central core of the primary cyanobacterial light-harvesting structure, known as the phycobilisome [94]. The linear absorption spectrum of APC is shown in Fig. 3-2c

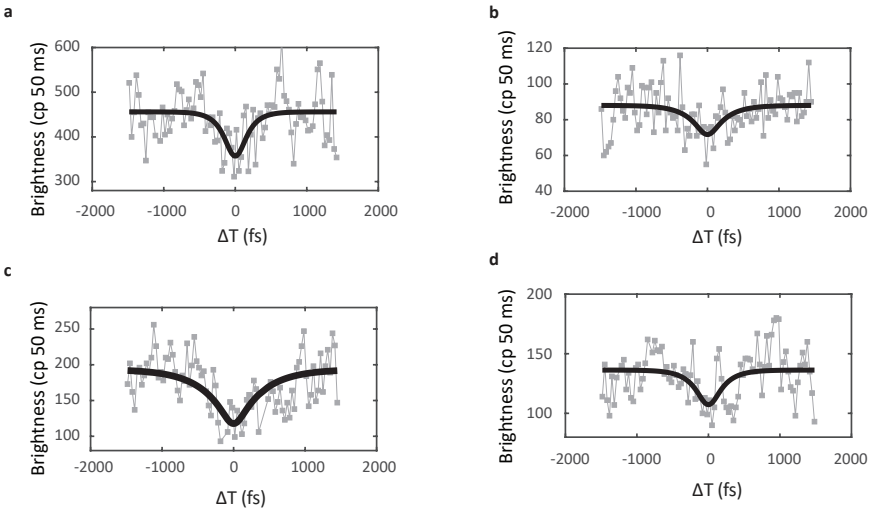

Figure 3-2: **Single-molecule pump probe (SM2P) experiments on allophycocyanin**: Representative SM2P traces (gray) of allophycocyanin with fits (black) for 610 nm excitation with decay time constants of 148±15 and 225±70 fs are shown in (a) and (b), respectively and for 645 nm excitation with decay time constants of 371±46 and 185±39 fs are shown in (c) and (d), respectively.

with the calculated absorption profiles for the underlying states [49]. The higher energy state has a broad absorption and the lower energy state has a narrow absorption with a vibrational mode at ∼1,600 cm^{-1} above the primary transition. Although the electronic coupling between the α and β chromophores leads to excited states that are a linear combination of the excited states of the individual chromophores, the large energy gap means that the higher energy state is dominated by the β chromophore and the lower energy one by the α chromophore [49, 185]. Thus, we refer to the states based on their dominant contribution.

The SM2P apparatus was constructed with a tunable excitation laser and a single-axis prism compressor for straightforward wavelength changes across the visible, which was used to investigate the dynamics of the individual chromophores. SM2P experiments on APC were performed with an excitation laser centered at 610 nm and 645 nm, which were selected to predominantly excite the β or α chromophores respectively (Fig. 3-2c) as in previous ensemble ultrafast measurements [86, 187, 189, 199]. In SM2P, the first saturating pulse drives damped Rabi oscillations between the ground state ($|0\rangle$) and the initially excited state ($|1\rangle$), resulting in an equal probability of

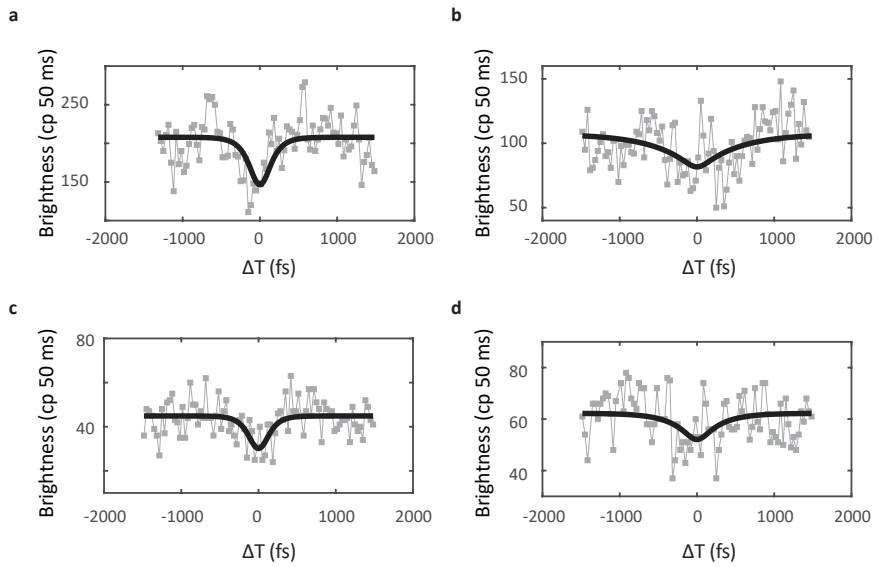

Figure 3-3: **Single-molecule pump probe (SM2P) experiments on C-phycocyanin**:Representative SM2P traces (gray) of C-phycocyanin with fits (black) for 610 nm excitation with decay time constants of 125±2 and 503±124 fs are shown in (a) and (b), respectively and for 645 nm excitation with decay time constants of 113±29 and 270±51 fs are shown in (c) and (d), respectively.

population in both states after interaction with the pulse. Population in $|1\rangle$ relaxes to the off-resonance state ($|2\rangle$) with a timescale determined by the microscopic properties of the sample. The second saturating pulse drives the same Rabi oscillations between $|0\rangle$ and $|1\rangle$, but does not interfere with population out of resonance (*i.e.*, in $|2\rangle$). On timescales longer than the relaxation time (Fig. 3-2a, right), the second Rabi oscillation provides another opportunity to populate $|1\rangle$ and subsequently transfer to $|2\rangle$, increasing the population and thus fluorescence from $|2\rangle$. By detecting fluorescence from $|2\rangle$ and scanning the delay from negative to positive times, an SM2P trace is recorded that shows a dip-like shape, which can be fit to extract the timescale of energy relaxation between states.

Representative SM2P traces are shown for primarily β excitation at 610 nm (Figure 3-2d,e) and primarily α excitation at 645 nm (Fig. 3-2f,g). While these β excitation traces exhibit timescales that are not statistically different (148±15 and 225±70 fs in Figure3-2d and e, respectively), the α excitation traces differ significantly (371±46 and 185±39 fs in Figure 3-2f and g, respectively), providing an initial

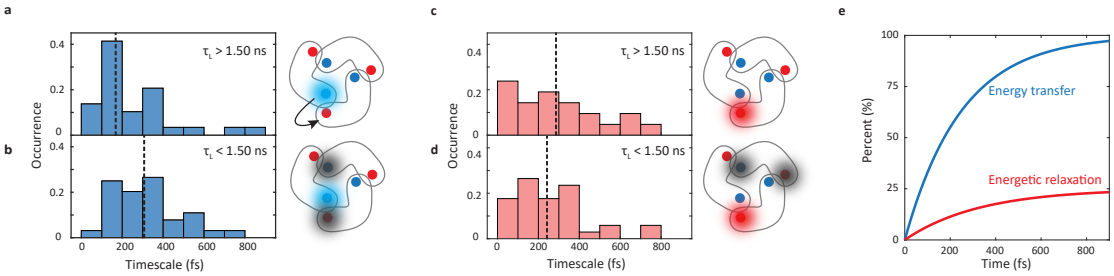

Figure 3-4: **Distributions of energetic relaxation and energy transfer timescales for APC**. Histograms of the energy relaxation timescales were constructed from the β excitation data (λ_{exc}=610 nm, blue) for the (**a**) bright ($\tau_L \geq$1.50 ns) population and (**b**) quenched ($\tau_L <$1.50 ns) population and from the α excitation data (λ_{exc}=645 nm, red) for the (**c**) bright population and (**d**) quenched population. The median values of the distributions are indicated by the dashed lines. As shown in (**a**), right, excitation of the β chromophore (blue) leads to energy transfer to the α chromophore (red). As shown in (**b**, **d**), right, photobleached chromophores (dark gray) lead to a loss of photoactivity and/or conversion into quenchers. (**e**) A kinetic model of energetic relaxation and energy transfer with the experimentally determined rates (SI Section 9), was used to calculate the percent of population transferred (blue) and of energetic relaxation due to nuclear motion (red) as a function of time.

demonstration of the ability of SM2P to uncover heterogeneity in ultrafast dynamics.

lator strength and/or spectral shifts of the photodegraded chromophore eliminate the rapid β to α energy transfer, and so only energetic relaxation due to nuclear motion remains [193, 194, 197, 198].

To separate and characterize energy transfer and energetic relaxation, four histograms were constructed from the measured timescales, divided by the excitation wavelength and the concomitantly measured fluorescence lifetime. The histograms are shown in Fig. 3-4 for β excitation (a,b) and α excitation (c,d) for bright ($\tau_L \geq$1.50 ns) and quenched ($\tau_L <$1.50 ns) populations, respectively, with their primary photophysical pathways illustrated. The quenching properties of the photodegraded β chromophore lead to quenched populations enriched in proteins without energy transfer and vice versa. Following previous work [194, 195], the photophysics were simulated (Fig. 3-22, SI Section 3.6.3). The simulations showed that the enrichment of the bright population in proteins with energy transfer reached a maximum of 86% at a cut off value of $\tau_L \geq$1.50 ns (Fig. 3-23). Statistical parameters for the histograms are given in SI Section 6.

In the β excitation data, the histograms have medians of 168 fs for bright APC and 308 fs for quenched APC (Fig. 3-4a, 3-4b). Comparison of the two distributions with a permutation test yielded a p-value of 0.0001 (SI Section 3.6.1), which establishes with a high probability (99.99%) that the two distributions are different. In contrast, in the α excitation data, the histograms have medians of 286 fs for bright APC and 242 fs for quenched APC (Fig. 3-4c, 3-4d), and comparison of the two distributions showed that they are the same (p >0.05, SI Section 3.6.1). Similarly, the quenched populations for β excitation and α excitation were the same (p >0.05, SI Section 3.6.1). In agreement with these results, energetic relaxation is expected to dominate in all three of these populations. The statistically significant shorter median timescale for the bright population of the β excitation data, the only histogram in which energy transfer is expected, is consistent with this picture.

The β excitation data can also be further analyzed to quantify the dynamics. Each of the histograms contains APC with intact chromophore dimers, which undergo energetic relaxation and energy transfer simultaneously, and photodegraded ones, which undergo energetic relaxation alone. Rate histograms were constructed for both the bright and quenched populations and fit with a two-component Gaussian mixture model (SI Section 3.6.1, Fig. 3-17). While similar rates were extracted from both distributions (Table 3.4), the faster component of ~ 0.007 fs^{-1} (140 fs) was dominant in the bright population, whereas the slower component of ~ 0.003 fs^{-1} (330 fs) was dominant in the quenched population. The simulations of APC predicted 86% and 32% of the photophysical states can exhibit energy transfer in the bright and quenched populations, respectively (SI Section 3.6.3). Thus, the faster component was assigned to energetic relaxation and energy transfer and the slower component was assigned to energetic relaxation alone.

To explore the ultrafast dynamics, a kinetic model of energy transfer and energetic relaxation was constructed (SI Section 3.6.4). From the additivity of rates, the two components of the Gaussian mixture model give a rate of ~ 0.004 fs^{-1} (250 fs) for energy transfer alone. Using the experimental rates in the kinetic model, >90% of energy transfer was complete by 600 fs, when only ∼20% of the energetic relaxation

had occurred as illustrated in Fig. 3-4e. The relative amplitudes indicate energy transfer generally precedes energetic relaxation.

The distribution of timescales that primarily includes APC with both energy transfer and energetic relaxation, shown in Fig. 3-4a, has a median of 168 fs and a mean of 249 fs, where the large difference between these two values is due to its asymmetric profile. In previous ensemble measurements, which are more accurately compared to the mean of single-molecule distributions, energy transfer between the two chromophores was found to occur on 220 fs and 280 fs timescales. The two timescales were ascribed to different conformational states of the protein backbone [86, 188]. Analysis using rates determined through a Gaussian mixture model, which is expected to recover the mean, found an energy transfer timescale of ∼250 fs, consistent with the ensemble values. However, the asymmetric nature of the measured distribution suggests that ensemble measurements are significantly lengthened by small sub-populations with slow transfer. This observation of an asymmetric distribution suggests that traditional theories of photosynthetic energy transfer, which were primarily developed based on mean values [9, 34, 43], may be distorted by these slow sub-populations.

An asymmetric distribution of energy transfer timescales can not only lengthen the average value, but also influence the functional form of measurements. Whereas a Gaussian distribution gives rise to an energy transfer process well-described by a single-exponential function, an asymmetric distribution can lead to more complex behavior, such as a stretched exponential or the bi-exponential observed previously for APC (SI Section 3.6.2, Fig. 3-21) [49]. Thus, instead of characterizing distinct sub-populations, ensemble measurements of multi-exponential dynamics could instead arise from non-Gaussian microscopic heterogeneity, which was observed theoretically for another photosynthetic light-harvesting protein in previous work and experimentally for APC here [200].

The full distribution of timescales that primarily includes APC with both energy transfer and energetic relaxation spans ∼65 fs to ∼800 fs. In ensemble measurements with high temporal resolution, sub-50 fs energy transfer was also observed

[49, 185, 187]. This population is absent here, which may be due to a smaller amplitude of this component and/or the challenges associated with characterizing this timescale due to the pulse duration (100-200 fs) (SI Section 7.1 and 7.2) [49]. The few measured timescales above ∼400 fs likely arise from the combination of the asymmetric distribution and the effect of Poissonian noise, which elongates the tail of SM2P distributions (SI Section 3.6.2)[93]. The lack of a significant population slower than ∼400 fs suggests that static conformational states of the protein do not often dramatically slow the energy transfer timescales. The effect of heterogeneity in the local protein dielectric environment on the distribution of energy transfer timescales was previously investigated theoretically. Using combined quantum chemical/molecular mechanical simulations, a ∼4-fold range of energy transfer times was found for another photosynthetic light-harvesting protein, which is roughly comparable with the measured range shown in Fig. 3-4a [201].

3.3.2 Energetic relaxation in APC

Upon photoexcitation, the chromophores in APC undergo energetic relaxation (redshifting) due to nuclear motion including intramolecular vibrational relaxation (IVR) and solvation within the protein pocket [202]. The ultrafast solvation, known as inertial solvation, involves coupling to the short-range motions of nearby amino acid side chains and solvent molecules. The collective reorganization of solvent molecules (diffusive solvation) occurs on longer timescales than the picosecond window investigated here [173]. The combined effects of IVR and solvation give rise to the Stokes shift, which moves population out of resonance with the laser pulse. This energetic relaxation can be investigated using the histograms where no energy transfer is present. For the α excitation data, the histograms of timescales from bright (Fig. 3-4c) and quenched (Fig. 3-4d) APC have similar median values (286 fs and 242 fs, respectively), which is consistent with previous pump-probe experiments that measured a 250 fs Stokes shift [86].

The spectral dependence of the energetic relaxation can be examined by comparing the α excitation data to the β excitation data for quenched APC. Similar median

timescales of 308 fs for the β excitation data (330 fs from the Gaussian mixture model, which finds mean values) and $\sim$260 fs for the α excitation data were determined. Previous studies reported comparable timescales of energetic relaxation for both chromophores, although two components at 120 fs and 230 fs were observed [86]. While the median timescales are approximately consistent with the longer of the two components, the shorter one is absent. This may be due to the coherent excitation scheme used in the ensemble measurements or the second component may be hidden in the width of the SM2P distribution [203].

3.3.3 Environment-dependent heterogeneity in energetic relaxation

The influence of the protein environment on the distribution of energetic relaxation timescales was investigated by comparing the distributions for APC, CPC, and Atto647N. CPC is another cyanobacterial light-harvesting protein that is homologous to an APC monomer with an additional peripheral chromophore (Fig. 3-1c and d) [94, 195]. There are large distances between the chromophores in CPC, and so energy transfer is slower than the time window measured here [186, 204]. Therefore, only energetic relaxation is present in the distribution. Atto647N is a widely-used single-molecule chromophore with sufficient photostability for SM2P, which the chromophores in APC and CPC lack. Histograms of the measured energetic relaxation timescales are shown in Fig. 3-5 for APC with α excitation (a), CPC (b) and Atto647N (c). Statistical parameters for all three distributions are given in SI Table 3.2, which show differences in both the peak locations and widths.

The distribution for Atto647N was compared to the distributions for APC and CPC in order to investigate the contribution of a protein scaffold, as Atto647N was embedded in a polymer matrix with a local aqueous environment. The asymmetric distribution and median timescale (148 fs) for energetic relaxation of Atto647N was similar to previous measurements of other chromophores in solution. Based on the previous work, we assign the measured energetic relaxation in Atto647N to IVR with

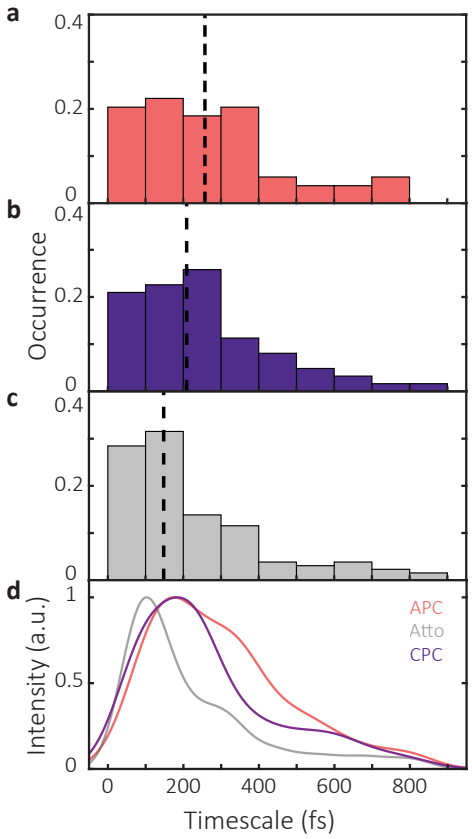

Figure 3-5: **Comparison of histograms of energy relaxation timescales**. Histograms of energy relaxation timescales for (**a**) APC with a 645 nm excitation, (**b**) CPC, and (**c**) Atto647N. The median values of each data set are indicated with a dashed vertical line at (**a**) 258 fs, (**b**) 216 fs, and (**c**) 148 fs. The kernel density estimation (KDE) smoothed fit for each histogram is shown in (**d**).

a contribution on the short timescales from electronic dephasing [141, 158]. The median timescales of energetic relaxation for APC and for CPC are similar at 258 fs and 216 fs, respectively, consistent with their homologous protein structures. In both proteins, the chromophores interact with the surrounding protein pocket by hydrogen bonds between the nitrogen atoms on its central rings and an aspartic acid residue and salt bridges between its side chain and nearby arginine and lysine residues [191]. The slower timescales for APC and CPC than for Atto647N suggest that these interactions with the protein pocket stabilize the excited chromophore and its immediate environment to slow relaxation processes such as IVR.

The slightly longer median for APC than for CPC is consistent with previous

measurements of the ultrafast fluorescence anisotropy decay that found the structural fluctuations of the chromophores in CPC are nearly 10-fold faster than those of the chromophores in APC [199]. The binding pocket of the α chromophore of APC is more polar than the other pockets, which could stabilize the excited state and give rise to the slightly slower relaxation [205]. Furthermore, in CPC, the torsional angle of the chromophore is $\sim$25° larger than in APC [185], and the more strained configuration could be less stable, *i.e.*, exhibit faster nuclear motion. The more buried position of the chromophores in trimeric APC (Fig. 3-2b) than in monomeric CPC (Fig. 3-1c) could also slow energetic relaxation. The solvent accessible surface area (SASA) for chromophores in CPC (300 Å^2) is twice that for chromophores in APC (150 Å^2). The increased solvent accessibility in CPC may create a more solution-like environment that speeds up energetic relaxation, as observed for Atto647N. Ensemble ultrafast measurements compared the relaxation timescales of chromophore-containing photosynthetic proteins from cryptophytes with open and closed protein scaffolds, which have correspondingly more and less solvent accessibility. These measurements showed faster relaxation for the open scaffolds, consistent with the results described here [126]. Other studies found that the dynamics of CPC were independent of bulk solvent, initially in contradiction with a dependence of relaxation on solvent accessibility [202]. However, the local chromophore environment, *i.e.*, the first solvation shell, may not fully reflect changes to the bulk due to interactions such as hydrogen bonding between the protein and water molecules [206].

Along with differences in the median, the distributions of timescales can be used to compare the heterogeneity in energetic relaxation. Each distribution was smoothed using a kernel density estimation (Fig. 3-5d) and the full width at half maxima (FWHM) of the smoothed curves were calculated, which describe the widths of the main peaks (SI Fig. 3-14). The distribution for Atto647N (FWHM=179 fs) is much narrower than the distributions for APC (FWHM=462 fs) and CPC (FWHM=295 fs). The width for Atto647N is similar to that measured previously for a series of other chromophores in solution, where the width was ascribed to a bimodal profile from the electronic dephasing and IVR contributions [141, 158, 207]. The wider distributions

for APC and CPC suggest that, in addition to slowing energetic relaxation, the protein matrix introduces more heterogeneity in the relaxation timescale than is present in an aqueous solution.

The distribution of energetic relaxation timescales is also broader for APC (FWHM = 462 fs) than for CPC (FWHM = 295 fs). The breadth for APC may arise from increased interaction with the protein due to the more buried position of its chromophores, although the differences in polarity and torsional angle could also play a role. The distribution for APC has signatures of a bimodal structure with peaks at ∼175 fs and ∼375 fs, along with an elongated tail as discussed above. In contrast, the distribution for CPC has only a single broad peak with a tail. The two peaks in the distribution for APC may correspond to the previously hypothesized two conformations responsible for the 220 fs and 280 fs timescales of energy transfer from ensemble measurements [49]. Alternately, previous measurements found a 400 fs component of energetic relaxation exclusively associated with the α chromophore in APC [86]. Although this component only appeared clearly upon excitation of the vibronic transition in ensemble measurements, which we do not excite here, signatures of this pathway may be contributing to the width of the measured distribution.

3.4 Discussion

In this work, we described spectrally tunable SM2P and the use of this tunability to disentangle the ultrafast dynamics of APC at the single-protein level. The distribution that primarily contains populations with energy transfer is clustered around the median at ∼150 fs, whereas the mean — and potentially ensemble values — were lengthened due to the influence of small subpopulations. Previous assignments of complex dynamics could instead arise from the microscopic heterogeneity, *i.e.*, non-Gaussian distribution, observed here.

Slow and heterogeneous energetic relaxation timescales for APC and CPC indicate that the protein matrix introduces variation in the photophysical processes. Because energetic relaxation is slower than energy transfer, the states involved in energy trans-

fer are the initially excited ones, which may be one mechanism for how rapid energy transfer is maintained despite the effects of heterogeneous energetic relaxation. In this picture, the reorganization of the environment, which can lead to trapping, is preceded by energy transfer amongst the electronic excited states [33]. It may also be that slow energetic relaxation in the protein helps maintain vibronic coupling during an energy transfer event, which is thought to mediate rapid transfer [208]. While previous work established that the electronic structure, and consequently energy transfer, was robust to protein-induced static heterogeneity [184], here we found that the heterogeneity also impacts the timescales of the dynamics. These studies illustrate that the ability of the protein to influence the timescales of energetic relaxation means the protein structure can control the excited states involved in energy transfer, and even the mechanism of energy transfer itself.

3.4.1 Methods

Single-molecule pump-probe (SM2P) spectroscopy. A schematic of the experimental setup is shown in the Figure Chapter 2 and is described in detail in Ref. [207]. In brief, a tunable fiber laser (FemtoFiber pro, Toptica; 120 fs pulse duration, ∼4 nm bandwidth, 80 MHz repetition rate) was used as the excitation source and the laser repetition rate was reduced from 80 MHz to 2.5 MHz or 312.5 KHz with an acousto-optic pulse picker (Brimrose Corporation, FSPP-400-80-BR-800). The prism compressor was designed with single-axis translation for easy optimization with spectral maximum. The compressor was translated to minimize dispersion for each center wavelength as measured at the sample position with an interferometric autocorrelation using a GaP photodiode (Marktech, MTPD3650D-1.4) [162]. Representative intensity autocorrelations for different laser excitations are shown in Chapter 2 with the FHWM determined assuming a Gaussian pulse. The laser pulses were split by a set of 50/50 beam splitters (Thorlabs, UFBS5050) and a delay stage in a Mach-Zehnder interferometer. The polarization was converted from horizontal to cicular polarization using a quarter-wavplate (Newlight Photonics, WPM03-Q-VIS). The excitation was coupled into a custom-designed inverted confocal microscope (Mad City labs, RM21)

and focused onto the sample with an objective (UPLSAPO100XO, Olympus, NA 1.4). Fluorescence emission was collected through the same objective and separated from the excitation by use of dichroic mirrors optimized for excitation filtering (Chroma, T635lpxr-UF3; Chroma, ZT647rdc-UF2) and a pair of bandpass filters (Semrock, FF02-675/67-25; Chroma, ET690/120x) Fluorescence photons were detected on an avalanche photodiode (SPCM-AQRH-15, Excelitas) with a time-correlated single photon counting module (TimeTagger20, Swabian Instruments). Fluorescence lifetimes were fit to a single exponential decay convolved with an experimentally determined instrument response function (~ 0.5 ns) as described in SI Section 5.

For SM2P experiments, the power was set to $\sim$1 pJ/pulse before the objective or 700 $\frac{\mu J}{cm^2}$ per pulse at the sample plane. The saturation power was experimentally determined by monitoring the fluorescence intensity of single APC (SI Section 3.5.2). The center wavelength of the laser was tuned to either 610 nm or 645 nm. For the 610 nm measurements, experiments were performed with both near-Fourier transform limited temporal compression (118 fs) and no temporal compression (180 fs). The measured dynamics were independent of pulse duration (Fig. 3-12). For the 645 nm measurements, experiments were performed with no temporal compression (300 fs) due to power restraints. The delay time between the two pulses was scanned from -1.5 ps to 1.5 ps at 100 μm/s (0.33 ps/s). Fluorescence emission was binned into 50 ms bins before being fit with maximum likelihood estimation to extract energy relaxation timescales. The fit function was the convolution of the measured intensity autocorrelation with an exponential rise function for energy relaxation as detailed in SI Section 3.5.1 [141, 145, 158]. The standard error was estimated using the Fisher information matrix [172]. Single-molecule blinking and on-off transitions in SM2P traces were identified by eye and omitted from the data analysis.

Energy relaxation timescales were used to construct histograms with the bin width determined by the Freedman-Diaconis rule. The generated distributions were compared using a Permutation test, which determines the likelihood of randomly allocating the complete data-set into two groups and obtaining the experimentally observed difference (SI Section 3.6.1). SASA values were determined using the 'Protein inter-

faces, surfaces and assemblies' service PISA at the European Bioinformatics Institute located online at (http://www.ebi.ac.uk/pdbe/prot_int/pistart.html) [209].

Sample preparation. APC (Sigma Aldrich, S868), CPC, (Agilent, PB11), and Atto647N (ThermoFisher, 04507-1MG-F) were purchased and diluted to ∼1 nM in pH 7.4 phosphate buffer solution (ThermoFisher, AM9624). An enzymatic oxygen-scavenging system was added to the solution at final concentrations of 25 nM protocatechuate-3,4-dioxygenase and 2.5 mM protocatechuic acid [163]. The solution was spincoated in 1% PVA onto glass coverslips, which were placed on a piezoelectric stage (Mad City labs, Nano-LP100) on the microscope.

3.5 Supplemental Information

3.5.1 Fit function used for parameter estimation

For the single-molecule pump-probe (SM2P) experiments, the fluorescence intensity was modeled as a function of the delay time between laser pulses as previously reported [141, 145, 158]. A complete derivation is shown in Ref. [207], but a brief explanation is illustrated below.

The modulated fluorescence intensity as a function of time delay, $I(\tau)$, is given by the convolution of the autocorrelation of the Gaussian pulse with the δ-pulse excitation solution as shown below: [180–182].

$$I(\tau) \propto \int AC(t-\tau)N_2(t)dt \tag{3.1}$$

where

$$AC(\tau) = \int f(t)f(t-\tau)d\tau \tag{3.2}$$

$AC(\tau)$ is the intensity autocorrelation assuming Gaussian pulses, $f(t) = \frac{\sqrt{2}}{d\sqrt{\pi}}e^{\frac{-2t^2}{d^2}}$, where d is the adjusted pulse FWHM given by $d = \frac{d_{fwhm}}{\sqrt{2ln(2)}}$, τ is the time elapsed before the second δ-pulse arrives, t is a dummy variable for integration, and N_2 is the population in the second, emissive state.

Equation 1 leads to the equation derived and applied by van Grondelle and co-workers [145]:

$$I(\tau) \propto I_{\infty}\left(1-\frac{p}{2-p}\frac{1}{2}e^{\frac{k_{ER}^2 d^2 \tau}{4}}\left(e^{-k_{ER}\tau}erfc\left(\frac{d^2 k_{ER}-2\tau}{2d}+e^{k_{ER}\tau}erfc(\frac{d^2 k_{ER}+2\tau}{2d}\right)\right)\right) \tag{3.3}$$

There are three fit parameters in Equation 3: the baseline intensity, I_{∞}, the probability of excitation by a single pulse, p, and the energy transfer rate, $k_{ER} = \frac{1}{\tau_{ER}}$. The background was experimentally measured separately, and added to this fit function. The data was fit to the sum of the fit function and background through a custom Matlab program that minimized the negative log-likelihood function (LL):

$$-LL = -2\sum_{i}(C_i - M_i) + C_i\, log\left(\frac{M_i}{C_i}\right) \tag{3.4}$$

where M_i are the counts predicted by the intensity model (Equation 3) and C_i are the experimental counts detected [183].

For each SM2P trace, p was allowed to vary between 0.2 and 1.5. The expected value in the saturation limit is 0.5 for a delta pulse. Larger values than 0.5 arise from population transfer during the pulse duration. Traces with values of p >1 were discarded as nonphysical. The rate, τ_{ER}, was allowed to range from 25 fs to 5000 fs. Traces that yielded values of τ_{ER} less than 35 fs or greater than 900 fs were discarded because simulated data suggested these timescales were not accessible experimentally due to our instrument response function and measured delay time range, respectively.

The goodness of fit was determined through the values of the log-likelihood. For a well fit system, the reduced log likelihood should approach one [210]. Fig. 3-6 shows the histogram of reduced log likelihood values from the fits of the APC data with 610 nm excitation. The values are distributed around one, consistent with a well fit system.

3.5.2 Characterization of probability of excitation by a single pulse

The probability of excitation by each laser pulse was determined experimentally. The single-molecule fluorescence brightness was measured at several pulse energies with 610 nm excitation. The distribution of brightness was constructed for each pulse energy (Fig. 3-7). Once the saturation limit is reached, the distribution no longer increases in brightness. To quantify this limit, the average brightness was extracted from the distribution and plotted as a function of the pulse energy. The resultant data points (Fig. 3-8) were fit to an exponential rise (τ=70 fJ/pulse) to determine the saturation threshold. SM2P measurements were performed at ~1,000 fJ/pulse to ensure all experiments were well above the saturation threshold.

Saturating power was also confirmed for each SM2P trace through the incorporation of individual shutters for the pump and probe beam. Before beginning an SM2P experiment, one beam was unblocked for 50 ms before the second shutter was opened. Saturation was observed through a similar level of fluorescence intensity with one and two pulses.

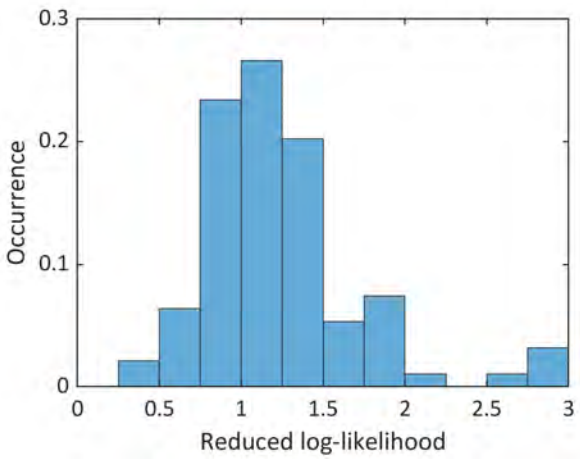

Figure 3-6: **Histogram of reduced log-likelihood values**. Reduced log-likelihood values from the fits of the SM2P traces for APC with 610 nm excitation. The reduced log-likelihood reports on goodness of fit and should approach one.

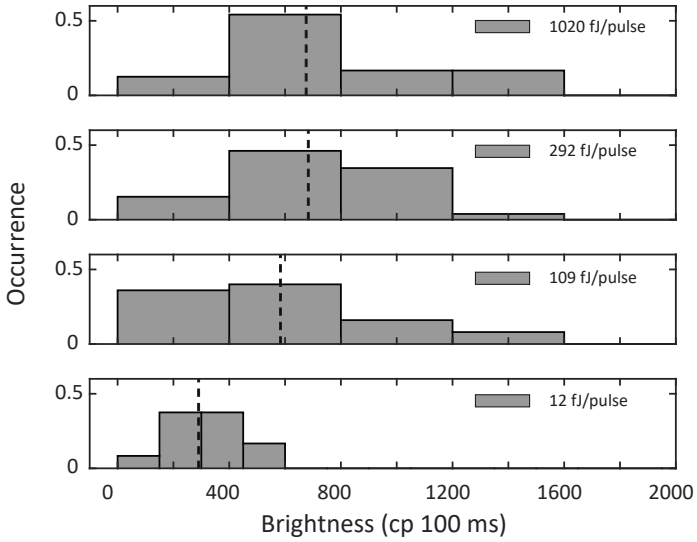

Figure 3-7: **Distribution of fluorescence brightness at different pulse energies.** Approximately 20 single-molecule fluorescence traces were recorded at each pulse energy. The fluorescence brightness for each trace was determined and these values were used to construct histograms for the pulse energies. The dashed lines indicate the mean of the brightness distributions.

3.5.3 Characterization and SM2P experiments on C-phycocyanin

3.5.4 Verification of aggregation state

Fluorescence correlation spectroscopy (FCS) was used to confirm the aggregation state of CPC and cross-linked APC. Fig. 3-9 shows the normalized autocorrelation curve calculated from the fluorescence photon stream for our samples at ∼5 nM concentration.

The autocorrelation curves ($G(\tau)$) were fit to:

$$G(\tau) = C + \left(\frac{1}{N}\right)\left(\frac{1}{1+\frac{\tau}{|\tau_D|}}\right)\left(\frac{1}{\sqrt{1+\frac{\tau}{V^2|\tau_D|}}}\right) \tag{3.5}$$

where C is a constant, N is the number of particles in the focal volume, τ is the delay time, τ_D is the diffusion time, and V is the detection volume defined as Z_0/w_0, where Z_0 and w_0 are the distances at which the 3D Gaussian volume has decayed to 1/e in the axial and radial directions, respectively. The fit is shown in black. Diffusion constants of $46\frac{\mu m^2}{s}$ and $77\frac{\mu m^2}{s}$ were calculated for APC and CPC, respectively. These

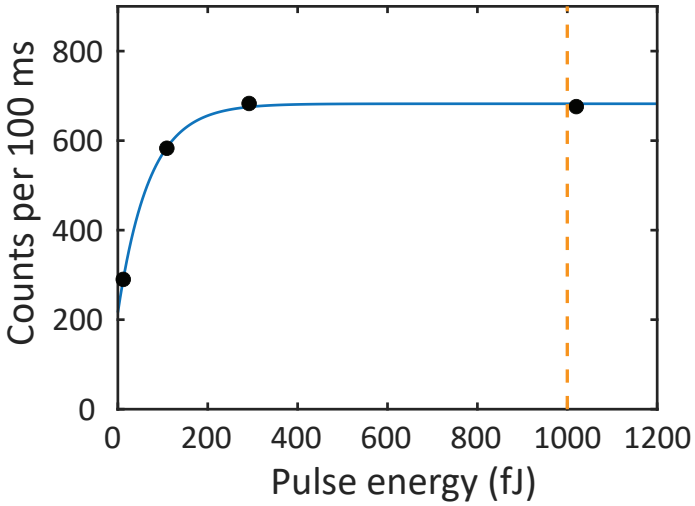

Figure 3-8: **Fluorescence brightness as a function of pulse energy.** The mean fluorescence brightness at different pulse energies (black dots) were fit with an exponential rise (blue line) to determine the saturation level. The dashed orange line indicates the pulse energy used for SM2P experiments.

numbers indicate that the aggregation state of APC is trimeric [211] and the aggregation state of CPC is monomeric [195]. The mismatch at long delay times for CPC is likely due to a small trimer population at the nM concentrations used, which is expected to disassociate at the pM concentrations of the SM2P measurements assuming an equilibrium.

3.6 Concomitant measurement of fluorescence Lifetime

Fluorescence lifetime data was simultaneously recorded during the SM2P experiments and used to characterize fluorescence states. Representative particles are shown in Fig. 3-10 with both the SM2P modulation of the fluorescence intensity and the corresponding fluorescence lifetime. Lifetimes were extracted from the decay traces with a custom MATLAB program that minimized the negative log-likelihood function (Equation 4) with the exponential model used by Maus et al. [210]. The model function was a single exponential convolved with an experimentally measured instru-

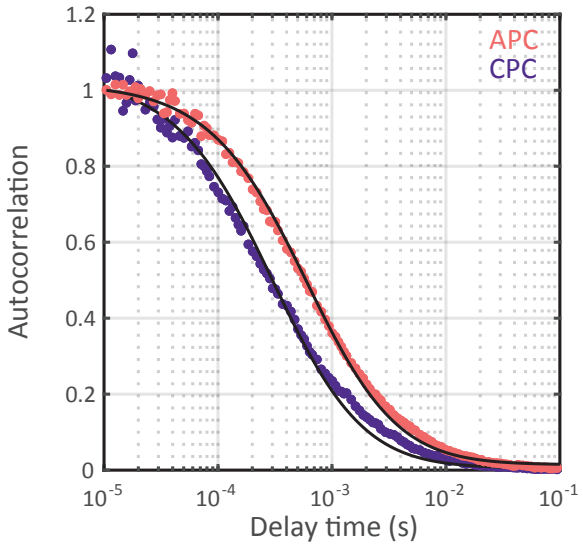

Figure 3-9: **Fluorescence autocorrelation curves of light-harvesting subunits**. FCS curves for APC (red) and CPC (purple) with least squares fits (solid black) were used to extract diffusion times of $D_{APC} = 46\frac{\mu m^2}{s}$ and $D_{CPC} = 77\frac{\mu m^2}{s}$. These values confirm that APC exists in a trimer aggregation state while CPC dissociates into monomers.

ment response function (FWHM $\sim$ 500 ps, solid gray line) plus the background. The model function (M_{exp}) is shown below in Equation 5 where IRF is normalized by the sum of photon counts, BG is an experimentally measured background trace at similar laser intensity, and γ weighs the BG component to signal intensity. In our case, γ was a tightly constrained fit parameter allowing for variation between samples. The exponential function is given by G where N is the total photon counts, A_0 is an offset, A_1 is the amplitude, and τ_1 is the time constant.

$$M_{exp} = IRF \otimes G + \gamma\ BG \tag{3.6}$$

where G is the normalized exponential decay given by

$$G = N\ \frac{(A_0 + A_1 e^{-t/\tau_1})}{\int A_1 e^{-t/\tau_1}\ dt} \tag{3.7}$$

Fluorescence lifetimes were measured for all successful SM2P experiments and are histogrammed in Fig. 3-11. The fluorescence lifetime distributions for APC with

610 nm and 645 nm excitation are similarly peaked around 1.5 ns as compared to previously reported experiments [193, 198]. However, the distributions cannot be directly compared because rapid photobleaching will bias the distributions to short timescales.

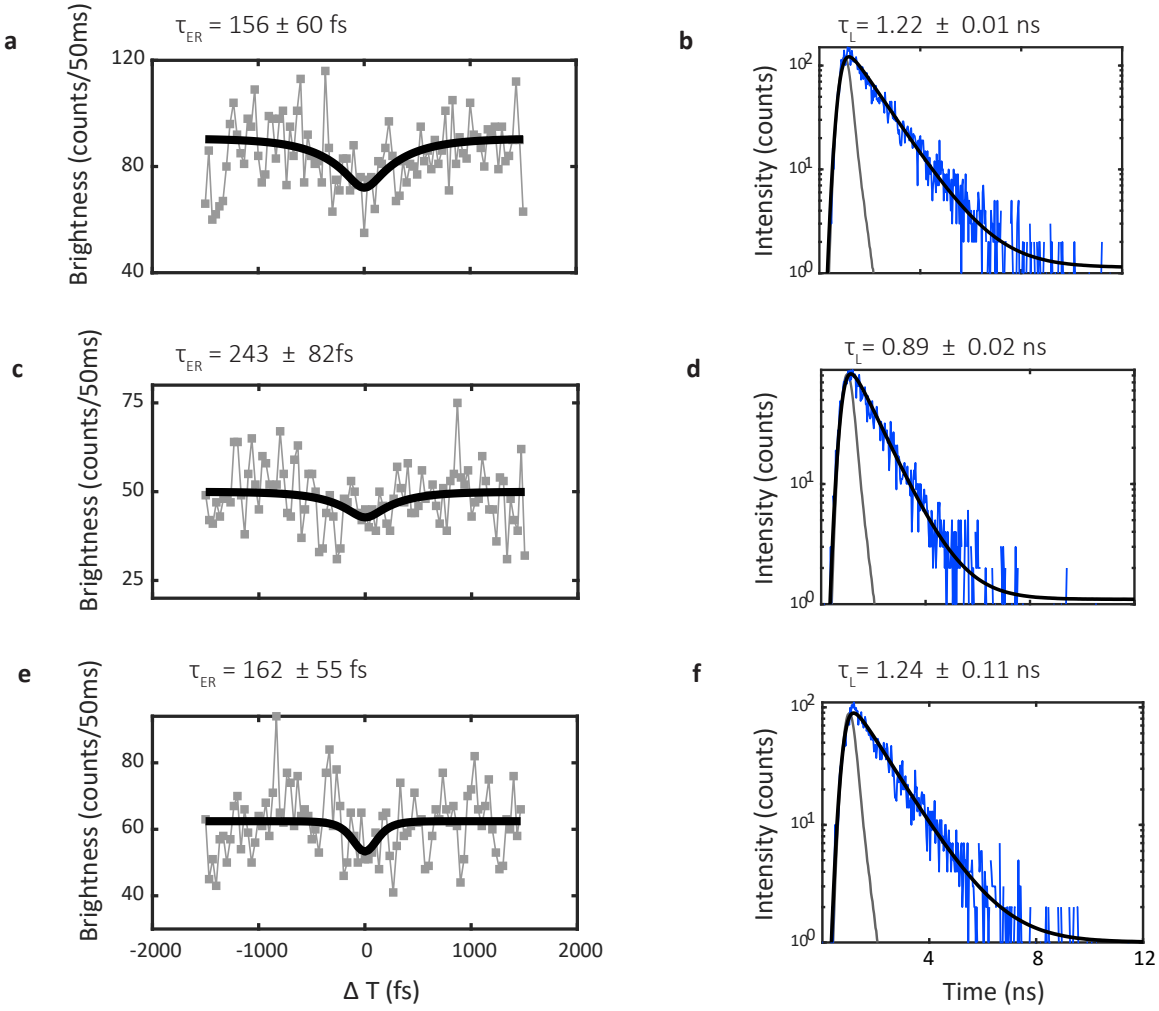

Figure 3-10: **SM2P experimental traces of APC with corresponding fluorescence lifetimes**. SM2P data from sequential measurements on a single APC. Energy transfer fits and SM2P fits are shown for the experiments pairs of (**a**, **b**), (**c**, **d**), and (**e**, **f**).

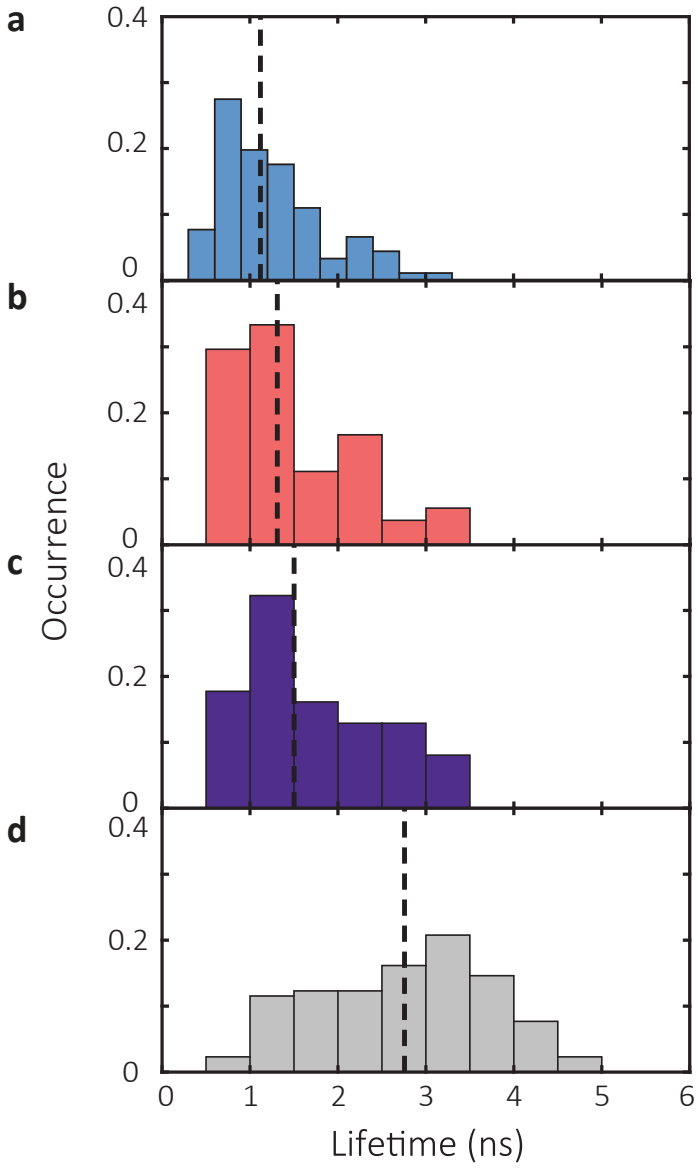

Figure 3-11: **Fluorescence lifetime distributions.** Histograms of fluorescence lifetimes for APC (610 nm, **a**), APC (645 nm, **b**), CPC (**c**), and Atto647N (**d**). Median values are marked with a dashed line at 1.12 ns (**a**), 1.31 ns (**b**), 1.50 ns (**c**), and 2.76 ns (**d**).

3.6.1 Statistical analysis of the distribution of energetic relaxation timescales

Dependence of energy relaxation histograms on excitation wavelength and pulse length

To ensure that the extracted microscopic dynamics were independent, *i.e.,* not due to, the pulse duration, we compared energy relaxation distributions for APC with 610

nm excitation with compressed and uncompressed pulses. This is shown in Fig. 3-12a These distributions were not significantly different from one another (two sample t-test gave a p-value ~ 0.6) and had similar qualitative distributions. The two data sets were combined for further analysis as described in the main text. Fig. 3-12b compares the energy relaxation distributions for Atto647N with 610 nm excitation (FWHM $\sim$ 180 fs) and 645 nm excitation (FWHM $\sim$ 303 fs). Similarly, these two data sets were found to derive from the same distribution (two sample t-test gave a p-value ~ 0.14). Further analysis of the Atto647N distributions is provided in [207] and these distributions were combined for analysis within this text. These results are in agreement with previous experimental and theoretical work in which the pulse duration was found to not affect the accuracy of values from SM2P [141, 145, 158, 165, 166, 212].

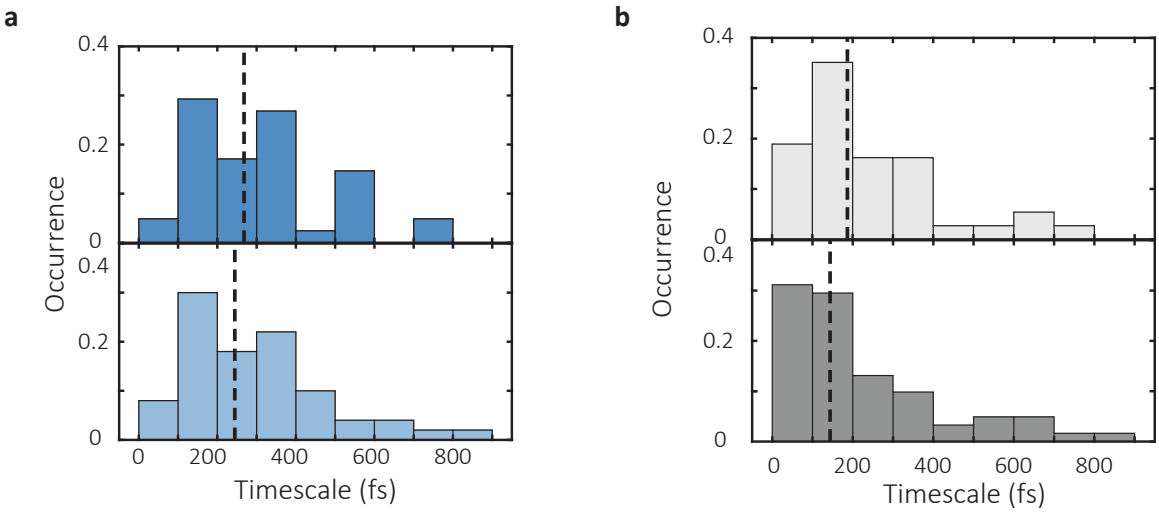

Figure 3-12: **Histograms of APC data.** (**a**) SM2P data for APC with 610 nm excitation. Dark blue represents the longer pulse length, (180 fs), and light blue represents the shorter pulse length (118 fs). (**b**) SM2P data for Atto647N with 610 nm excitation and 180 fs FWHM (top) and 645 nm excitation with 303 fs FWHM (bottom). Dashed lines indicate the medians of the distributions and are listed in Table S1.

Table 3.1: Statistical parameters for samples with different exication wavlength and pulse length

Sample	median (fs)	mean (fs)	σ (fs)	IQR (fs)	N
Atto647N (610 nm, 180 fs)	185	247	189	201	52
Atto647N (645 nm, 303 fs)	124	210	189	192	78
APC (610 nm, 118 fs)	245	294	181	228	51
APC (610 nm, 180 fs)	268	308	183	209	51

Comparison of energy-relaxation distributions for APC, CPC, and Atto647N

A combination of permutation tests and bootstrapping methods were used to investigate the timescale distributions presented in this work [213]. Bootstrap methods were used to estimate standard errors to compare parameters that describe the distributions. Fig. 3-13a shows the median values with the standard error determined by bootstrapping 10,000 times. Atto647N was found to have a significantly shorter median timescale than the phycobiliproteins. Fig. 3-13b shows the results of a permutation test between APC with 610 nm excitation and the combined Atto647N dataset. A permutation test pools the data and randomly assigns data points into two groups with the same size as the initial pooled data sets. The difference in statistical values between the resulting two groups (median) is calculated and this process is repeated many times. This tests the null hypothesis that the new data sets come from the same distribution and takes into account the fluctuations due to finite data samples. After repeating the process 10,000 times, we see that on average the difference between the two groups is zero, as expected for the null hypothesis, and that the chance of observing the experimental value for the median difference of 105 fs is 0.01 % as indicated by the red line in Fig. 3-13b. P-values of 0.0001, 0.001 and 0.001 were measured for APC with 610 nm excitation, APC with 645 nm excitation, and CPC when compared with Atto647N. The Benjamini–Hochberg procedure was used to take into account multiple testing, but the results stand as indicating that the phycobiliproteins are significantly different than Atto647N. Table 3.2 contains the statistical parameters for all datasets.

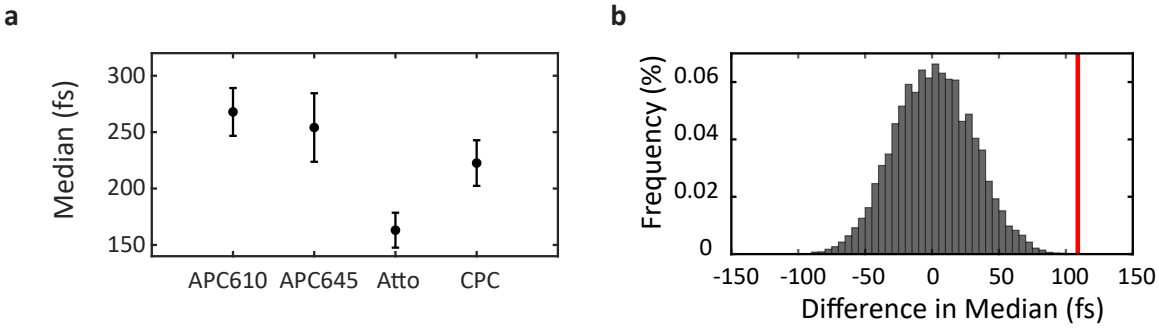

Figure 3-13: **Statistical analysis of the medians**. (**a**) The median values of the various samples with error bars given by the standard error obtained by bootstrapping. (**b**) The results of 10,000 iterations of a permutation test for Atto647N and APC with 610 nm excitation. The red line indicates the observed experimental value for the difference in medians. The location in the extreme tail of the distribution (p-value = 0.0001) shows that these distributions are significantly different

Table 3.2: Statistical values for SM2P experiments.

Sample	median (fs)	mean (fs)	σ (fs)	IQR (fs)	N
Combined Atto647N (610 nm, 645 nm)	148	224	187	205	130
Combined APC (610 nm)	257	300	180	223	93
APC (645 nm)	258	284	196	269	55
CPC	216	267	187	225	67

Comparison of the widths of the energy-relaxation distributions

To compare distribution widths, the data was smoothed using the kernel density estimation function in MATLAB and then the FWHM of the main peak was calculated. One example of the kernel density estimation (KDE) for APC with 610 nm excitation is shown in Fig. 3-14a. The resulting smoothed distribution curves for all data sets are shown in Fig. 3-14b. To determine whether the FWHM of Atto is significantly different from the phycobiliproteins, all of the data was pulled together and randomly assigned to four groups with sample sizes equal to the true data sets. The narrowest FWHM was chosen as the test statistic and is shown in Fig. 3-14c. This tests the probability of pulling a FWHM value as small as the experimentally observed Atto647N data set. Although the distribution is not normal, we can still determine that the chance of pulling a FWHM = 179 fs (the FWHM of Atto, red line in Fig. 3-14c) is less than 1.65%. This meets the p=0.05 standard, confirming

that the narrower distribution for Atto647N is statistically significant. The measured FWHM values with standard errors are shown in Fig. 3-14d.

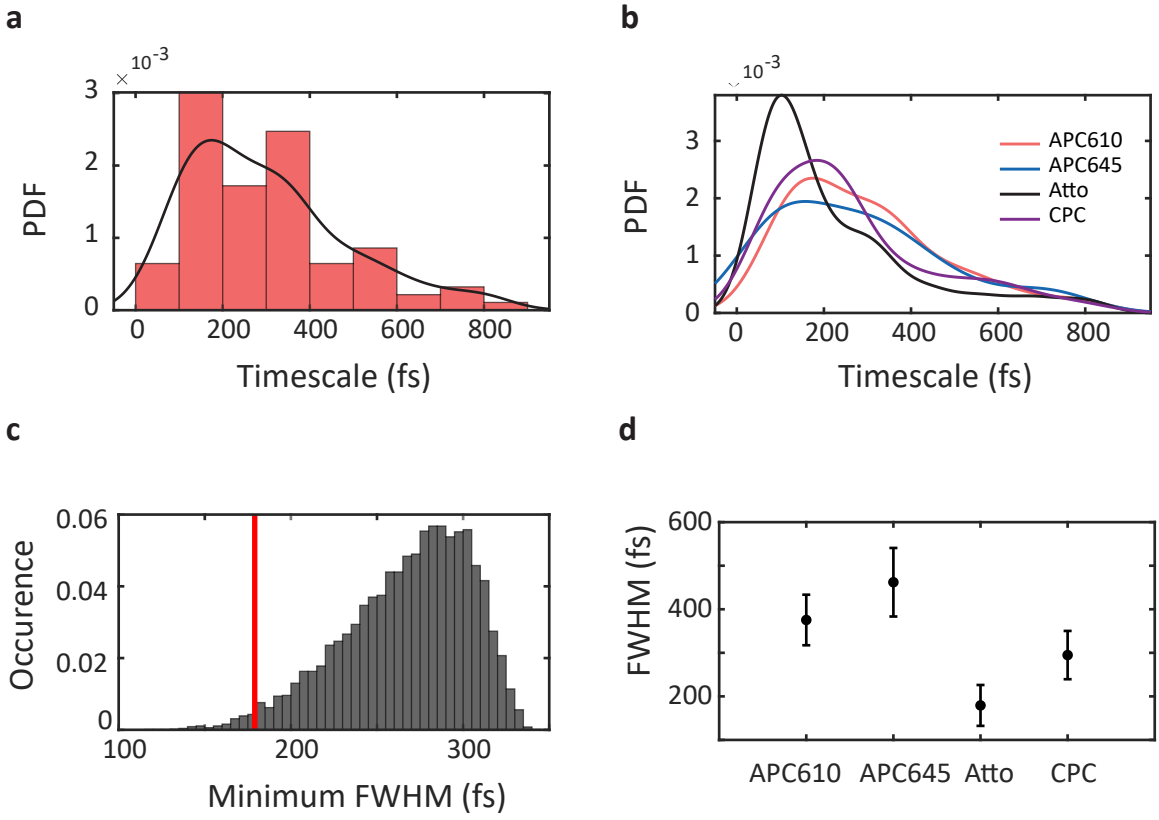

Figure 3-14: **Analysis of the width of the distributions**. (**a**) An example of a kernel density estimation (KDE) for APC with 610 nm excitation. (**b**) The KDEs for the four samples. (**c**) The results of a permutation test where the data was randomly divided into four groups and the smallest FWHM was determined. The chance of retrieving the experimentally observed value (FWHM_{Atto} = 179 fs, indicated by the solid red line) has a p-value of 0.0165. (**d**) The FWHM of the KDEs for the four samples with the error bars given by the standard error obtained from bootstrapping.

Comparison of the bright and quenched populations of APC with 610 nm excitation.

A permutation test with 10,000 iterations was used to further evaluate the statistical significance of the differences between bright and quenched states of APC with 610 nm excitation. The results of the permutation test are shown in Fig. 3-15. This

distribution shows that the probability of randomly drawing two data sets with the appropriate sizes and seeing the observed difference in medians of 168 fs is only 0.06 %. Table 3.3 contains the statistical values for the different states.

To further illustrate the difference between the bright and quenched states, cumulative density plots are shown in Fig. 3-16 for APC with 610 nm excitation (a) and 645 nm excitation (b). These plots highlight the increased accumulation of data points at faster timescales for the bright versus quenched states for the 610 nm excitation compared to 645 nm excitation. $\sim$ 30% of the quenched timescales occur before 200 fs, $\sim$ 50% of the bright timescales arrive before 200 fs for the 610 nm excitation, while the two curves are almost identical for APC with 645 nm excitation.

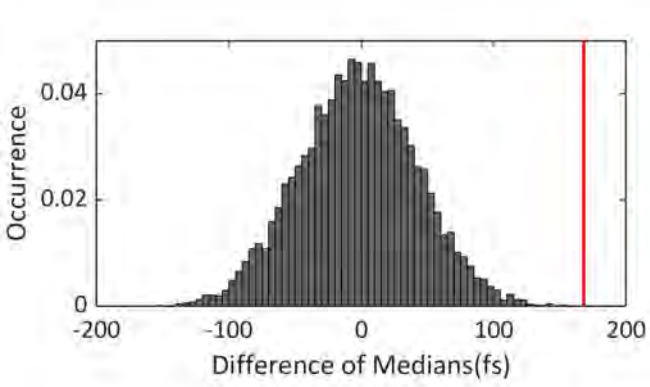

Figure 3-15: **Permutation test results on APC with 610nm excitation**. 33 timescales were randomly drawn without replacement from the APC with 610 nm excitation data-set to simulate the bright population and the median was compared to unselected values. This process was repeated 10,000 times. The red line indicates the observed experimental value of 168 fs that occurs less than 0.07% of the time.

Table 3.3: Statistical values filtered by lifetime.

	median (fs)	mean (fs)	σ (fs)	N
APC (610 nm, bright)	168	249	186	29
APC (610 nm, quenched)	308	324	174	64
APC (645 nm, bright)	286	305	218	21
APC (645 nm, quenched)	242	271	183	34

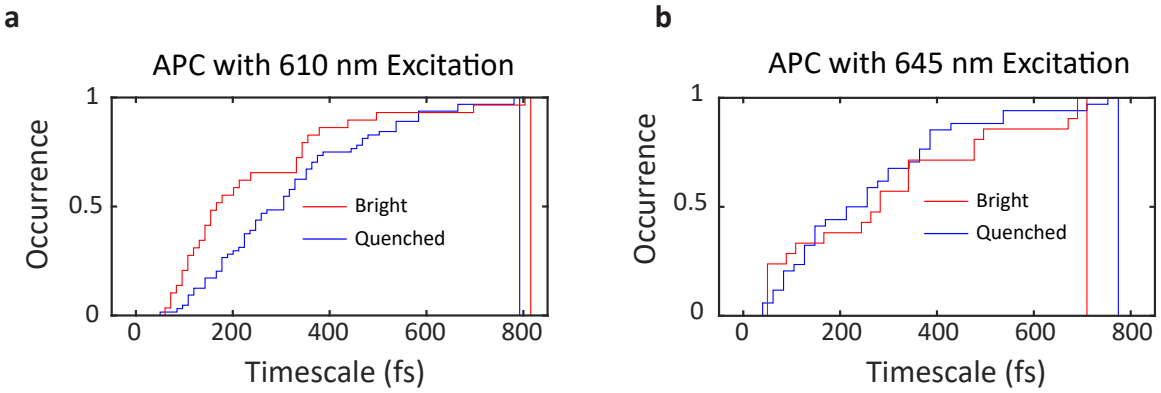

Figure 3-16: **Bright and quenched cumulative probability histograms.**. (**a**) For 610 nm excitation, a steep rise in the cumulative density function is shown for bright (red) versus quenched (blue). This is most easily seen at 200 fs, where a greater than 20% difference occurs. (**b**) For 645 nm excitation, the two histograms are effectively the same.

Extraction of rates for ultrafast dynamics

In order to quantitatively extract the rates from the measurements, the 610 nm excitation data were fit with a two component Gaussian mixture model (Fig. 3-17, Table 3.4), as 610 nm excitation is expected to excite proteins with both energy transfer and energetic relaxation and proteins with energetic relaxation alone. Although the distributions are non-Gaussian (Section 3.6.2), the Gaussian mixture model captured the populations observed in the distributions. Similar rates were extracted for both distributions but the faster component dominates the bright population whereas the slower component dominates the quenched population. Based on analysis of simulated data, the center values from the components can be extracted reliably despite the non-Gaussian profile, although the amplitudes and widths are less accurate [207].

Table 3.4: Fit parameters from Gaussian mixture model

	A_1 (%)	k_1 (fs^{-1})	σ_1 (fs)	A_2 (%)	k_2 (fs^{-1})	σ_2 (fs)
APC (610 nm, bright)	71	0.0077	3×10^{-3}	39	0.0024	6×10^{-4}
APC (610 nm, quenched)	35	0.0068	3×10^{-3}	65	0.0029	1×10^{-3}

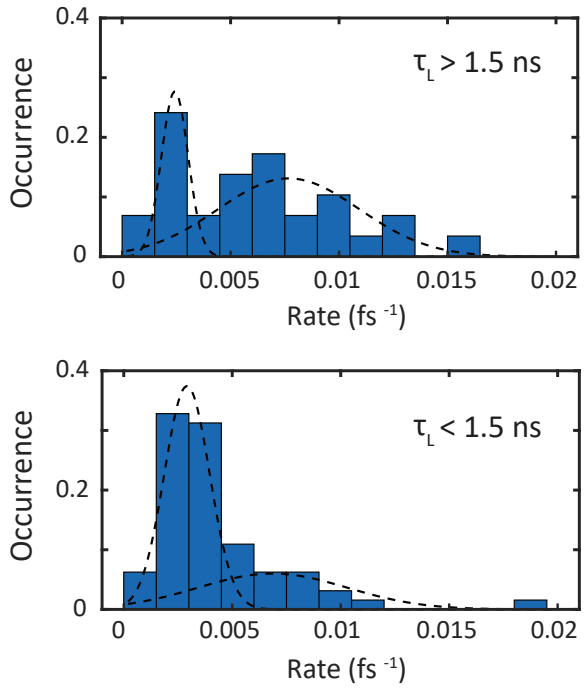

Figure 3-17: **Gaussian mixture model extracts two rate components**. The distributions of energy relaxation rates from the bright (top) and quenched (bottom) populations were fit to a two-component Gaussian mixture model, which is shown in dashed lines. All parameters of the Gaussian mixture model fit are given in Table 3.4.

3.6.2 Contributions to the distribution of energetic relaxation timescales

Analysis of sub-populations in bright APC distribution

To further understand the sub-populations present in the distribution of bright APC with 610 nm excitation (APC610B), representative distributions were simulated. For the simulations, 50 values were randomly selected from a Gaussian distribution with center values (τ_{sim}) of 150 fs and 50 fs and a width of the same value. These parameters were then used to simulate SM2P traces, Poissonian noise was added, and the traces were fit following the procedure used for experimental data to extract energy relaxation timescales. The pulse length was set to 120 fs (FWHM) for simulations. Fig. 3-18 shows histograms of the simulated data as well as the APC610B distribution. To quantify the sub-populations observed in the energy relaxation timescales,

the top of the histograms display the percent of values between 0 – 100 fs, 100 – 400 fs, and 400 – 850 fs. The simulations show that the bulk of the values fall between 100 – 400 fs, and that $\sim$ 5 - 10 % of the values are greater than 400 fs due to Poissonian noise and the shape of the distribution, as discussed in more detail in Section 3.6.2 and in Ref. [207]. Fig. 3-18C illustrates the distribution for τ_{sim} = 50 fs, which includes an increase of population of $\sim$ 20 % in the 0 – 100 fs range. This increase in timescales faster than the pulse length (150 fs), suggests that the fast timescales (50 fs) skews the distribution to short timescales. The lack of fast timescales for APC610B and τ_{sim} = 150 fs indicates that there is no significant component faster than pulse length in APC610B.

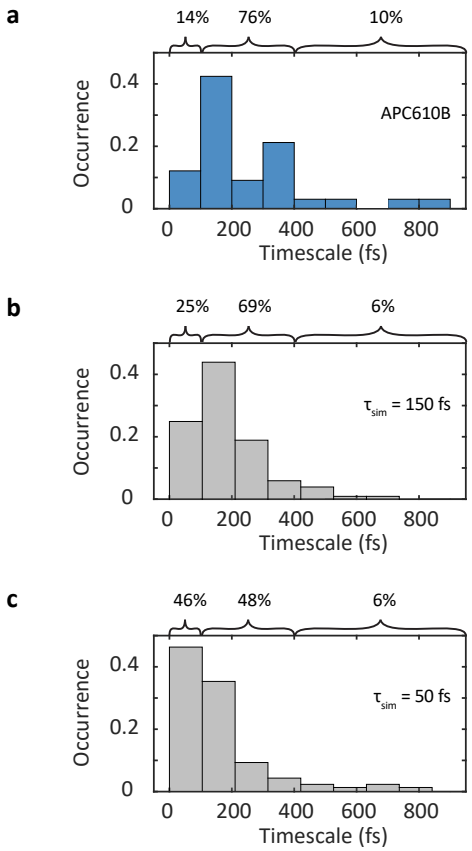

Figure 3-18: **Comparison of energy transfer distribution with simulated timescales**. Histograms with percentages shown above for population between 0–100 fs, 100 –400 fs, and 400–850 fs. Selected data sets are (**a**) APC bright population with 610 nm excitation, (**b**) Simulation data for τ_{sim} = 150 fs, (**c**) τ_{sim} = 50 fs

Observation of populations with fast dynamics

To further characterize the ability of the SM2P apparatus to identify populations with <100 fs dynamics, representative distributions were simulated for τ_{sim} of 35 fs and 100 fs following the procedure described above. Fig. 3-19 illustrates these two simulated distributions. The simulations show that the fast population appears as a shift of the distribution to short timescales in the 0 – 50 fs range. While these redistributions of population can be observed, the precision with which the timescale is measured decreases when the values of τ are much shorter than the pulse duration. The ability to observe these populations arises from the temporal resolution relative to the pulse duration for SM2P, although this resolution is better than typical ultrafast measurements because SM2P is in the strong field as opposed to the perturbative regime [165–167].

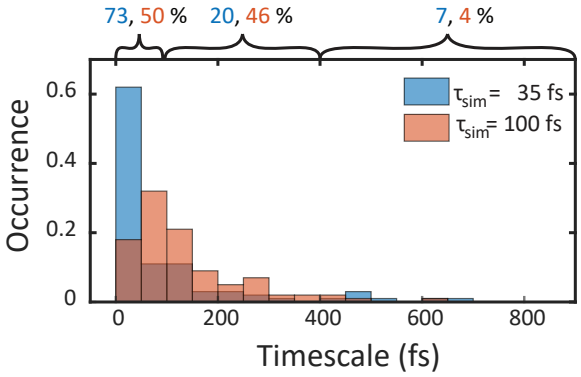

Figure 3-19: Comparison of energy transfer distributions with fast simulated timescales. Histograms of simulated data for τ_{sim} = 35 fs and 100 fs. Percent of population between 0–100 fs, 100–400 fs, and 400–850 fs is indicated above for all distributions.

Contributions to tail of distribution

To further characterize the contributions to the tails of the SM2P distributions, distributions were simulated for τ_{sim} of 250 fs and a width of the same value following the procedure described above. Simulated SM2P distributions were generated for timescales selected from a Gaussian distribution and an exponential Gaussian distribution as shown in Fig. 3-20a.

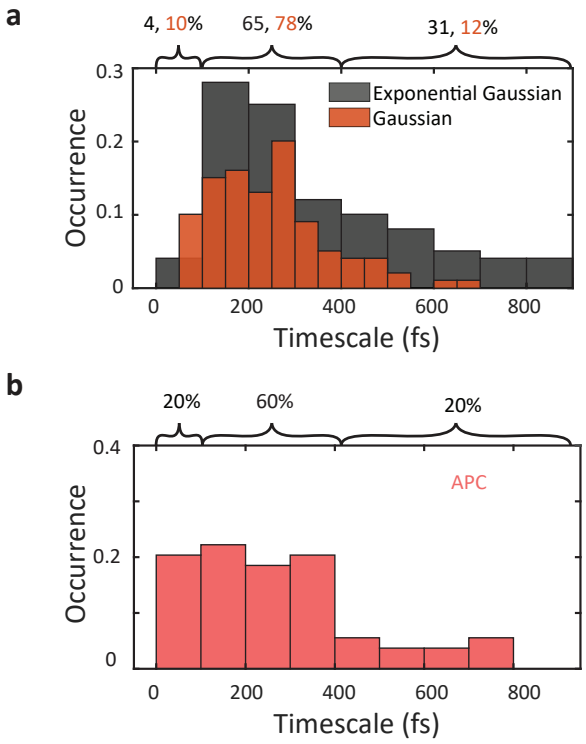

Figure 3-20: Population in elongated tail of skewed distributions. (**a**) Sampling energy relaxation values from a Gaussian distribution (orange) leads to an elongated tail and non-Gaussian distributions (p-value = 1×10^{-3}). Sampling from an exponential Gaussian with an equal mean (gray), leads to an extended tail. (**b**) Distribution of energy relaxation timescales for APC with 645 nm excitation. Percent of population between 0–100 fs, 100–400 fs, and 400–850 fs is indicated above for all distributions.

SM2P distributions have an elongated tail due to Poissonian noise [207] for a Gaussian distribution. The population of the tail was ~3-fold greater for the exponential Gaussian distribution. The population of the tail in the experimentally-measured SM2P histograms (reproduced for 645 nm excitation of APC in Fig. 3-20b) is between the two simulated values, suggesting a contribution from both Poissonian noise and an underlying asymmetric distribution.

Effect of a skewed distribution on ensemble kinetics

The non-Gaussian shape of our distributions were confirmed through Shapiro-Wilk tests. The Gaussian character of the distributions were evaluated for histograms of both timescales and rates for all data sets. The resulting p-values (Table 3.5)

confirmed that the null hypothesis of normality was rejected at the 10^{-5} significance level for all distributions.

Table 3.5: p-values from Shapiro-Wilk tests.

	energy transfer rates	energy transfer timescales
APC (610 nm)	4×10^{-7}	4×10^{-5}
APC (645 nm)	6×10^{-6}	5×10^{-4}
CPC	8×10^{-8}	5×10^{-5}
Atto647N	2×10^{-6}	6×10^{-5}

The non-Gaussian distribution of energy transfer timescales observed may give rise to an ensemble averaged decay may have a more complex functional form than a simple mono-exponential. Previous ensemble ultrafast experiments generally modeled non-mono-exponential behavior as a sum of exponential terms where each time constant is assigned to a different physical interpretation. To better quantify how non-Gaussian distributions influence ensemble behavior, we sampled rate constants from a Gaussian distribution and an exponential Gaussian distribution (Fig. 3-21). The two distributions (Fig. 3-21) have the same mean value and similar spread. These distributions were sampled 1000 times and the rate constants were used to make simple exponential decay curves as a function of delay time and then averaged; these averaged decay curves are shown in Fig. 3-21b and simulate an ensemble measurement. We found that the Gaussian sampled data is well described by a single exponential decay, as shown by the straight line in the semi-log plot. However, the data sampled from the exponential Gaussian distribution is not well described by a mono-exponential decay, but instead requires a bi-exponential or other model. This brief analysis suggests that a non-Gaussian distribution of decay rates may lead to multi-exponential dynamics in ensemble experiments.

3.6.3 Simulation of the photophysics of APC

Number of photophysical states. Trimeric APC contains a total of six chromophores as each monomer contains an α and a β chromophore. In previous single-molecule studies [194], it was found that both the α and β chromophores can photo-

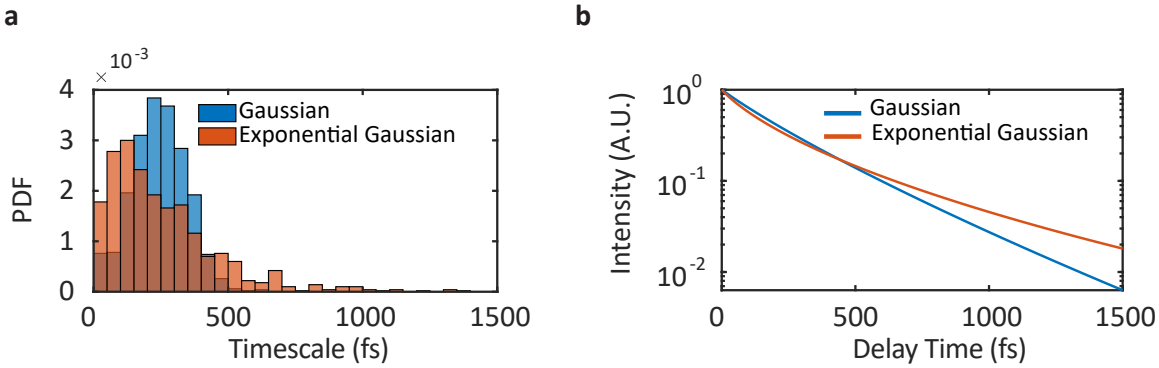

Figure 3-21: **Effect of distribution on ensemble dynamics**. Rate constants were randomly sampled from a Gaussian and an exponential Gaussian distribution as histogrammed in (**a**). The rate constants were then used to create a set of decay curves that are averaged in and plotted in a semi-log plot in (**b**) to highlight a turnover from mono-exponential to bi-exponential behavior.

bleach and become optically dark and only the β chromophore can photodegrade into a quencher for neighboring chromophores. From these constraints, there are a total of 66 possible photophysical states [194] with different combinations of quenchers and/or photobleached chromophores, which combined with intact APC yields a total of 67 states.

Simulation of lifetime and brightness. For each photophysical state, we simulated the fluorescence lifetime (τ_L) and brightness (B) by adapting the formalism previously published for APC and CPC [194, 195]. We modeled how the probability of observing the excitation at any specific chromophore in APC changed in time, $d\boldsymbol{p}(t)/dt$. This coupled energy transfer system is described using the following master equation:

$$\frac{\mathrm{d}\boldsymbol{p}(t)}{\mathrm{d}t} = \mathbf{M}\,\boldsymbol{p}(t) \tag{3.8}$$

where $\mathbf{M}$ is a transition matrix with non-diagonal elements:

$$M_{ji} = -k_{ji} \text{ for } (i \neq j) \tag{3.9}$$

where k_{ji} is the rate at which donor chromophores j transfer energy to acceptor chromophores i (row i, column j). The energy transfer rates were previously reported

values calculated using Förster theory for chromophore positions and orientations given by the structural model of APC [194]. The diagonal matrix elements, M_{ii} correspond to the total energy loss rate for that chromophore, which is the summation of energy loss due to radiative and non-radiative decay, measured as the fluorescence lifetime, k_{ii}^{10}, and energy transfer from that chromophore, as shown below.

$$M_{ii} = -\left(k_{ii}^{10} + \sum_{i,j\neq i} k_{ji}\right) \tag{3.10}$$

Because we have N chromophores participating in the energy transfer, we will end up with N solutions to Eq. 3.8, $\mathbf{M}$ will be an NxN matrix, and $\boldsymbol{p}(t)$ will be a vector Nx1. The total probability of observing fluorescence from any given chromophore i provided that chromophore j has been excited can be calculated as follows.

$$P_i^j = \int_0^\infty p_i^j(t) k_{ii}^{10} \Phi_i \mathrm{d}t \tag{3.11}$$

Φ_i represents the relative quantum yield of that chromophore, and the previously measured values for each subunit were used [194, 214, 215]. The total probability that a chromophore i will fluoresce, P_i, can then be determined by summing over the product of each excited chromophore case and its associated absorbance probability, A_j.

$$P_i = \sum_j A_j P_i^j \tag{3.12}$$

The brightness of that configuration B is then calculated by adding the probability of emission for each chromophore together.

$$B = \sum_i P_i \tag{3.13}$$

The simulated fluorescence decay $g(t)$ for each state can be determined in the following way.

$$g(t) = \sum_i k_i^{10} \Phi_i \left(\frac{\sum_j A_j p_i^j(t)}{\sum_j A_j}\right) \tag{3.14}$$

Each decay was then fit to a exponential decay to extract the fluorescence lifetime, τ_L.

To account for each different photophysical state, two additional parameters were included in our model: (1) a vector PB that catalogued which chromophores were photobleached in a given state; and (2) a vector Q that catalogued the quenching status of the β chromophores. When setting up the transition matrix $\mathbf{M}$ for each photophysical state, if a chromophore was photobleached, its corresponding row and column were set to zero since it could no longer donate or accept excitation. Each diagonal element in $\mathbf{M}$ was then recalculated to reflect the change in the off-diagonal elements. Additionally, the fluorescence rate of the photobleached chromophore was also set to zero. If a β chromophore was a quencher in a given state, all the corresponding α chromophores had their fluorescence emission rates reduced from 1/1.6 ns to 1/1.3 ns according to previous experimental measurements [194] of the effect of the quencher. Furthermore, the fluorescence emission rate of the quencher β chromophore was set to zero. The column in $\mathbf{M}$ corresponding to the quencher chromophore was set to zero to describe the lack of energy transfer to other chromophores, while the row was unchanged. These actions reflected that the quencher would not transfer energy to other chromophores or fluoresce but could still accept energy, respectively.

All 67 photophysical states were analyzed for their fluorescence lifetimes and brightness and the resulting values are plotted in Fig. 3-22 along with the measured single-molecule fluorescence data. As illustrated, there is good agreement between the simulation and the measured data.

Lifetime cutoff for bright and quenched populations. In order to disentangle the contribution of energy transfer, the simulated photophysical states were divided into those that contained an intact α/β dimer for energy transfer and those that did not. These two types of proteins are plotted in Fig. 3-22a in blue and black, respectively. The quenching properties of photodegraded β pigment [194] led to a quenched population enriched in states that lack intact dimers and vice versa. As a simple method to evaluate the level of enrichment, the data was divided into bright and a quenched populations based on a lifetime cutoff value. The percent of photo-

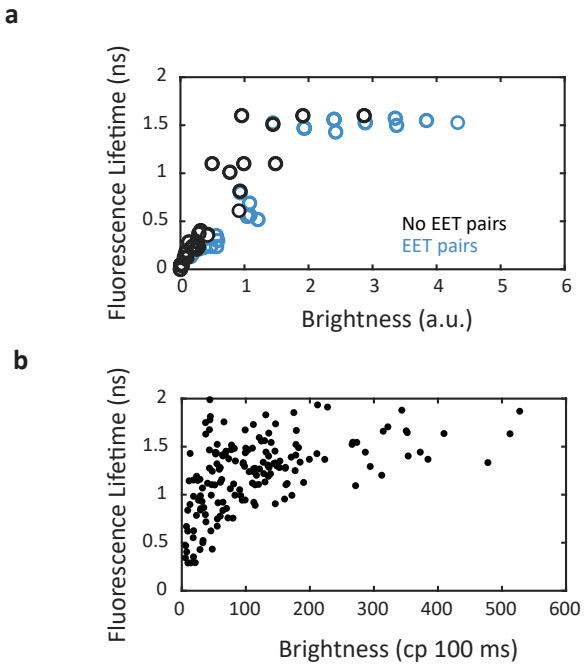

Figure 3-22: **Brightness and lifetime plots of the photophysical states of APC.** (**a**) Simulated values of brightness and lifetime for the 67 photophysical states of APC. States containing intact α/β chromophore pairs, which can give rise to energy transfer, are in blue and photophysical states without intact pairs are in black. (**b**) Experimental brightness and fluorescence lifetime plot for APC from single-molecule fluorescence experiments.

physical states with intact chromophore pairs for energy transfer was calculated for both populations for all lifetime values from 0.5 – 1.6 ns. The percent for both the bright and quenched populations is plotted in Fig. 3-23. Through this metric, the maximum level of enrichment in photophysical states containing energy transfer pairs was at a lifetime cutoff of $\geq$1.50 ns, where 86% of the states in the bright population contain intact chromophore dimers in contrast to the 32% in the quenched population. These percents are in approximate agreement with the amplitudes of the two components from the fit to the measured histograms, 71% for the bright population and 35% for the quenched population as shown in Section 3.6.1.

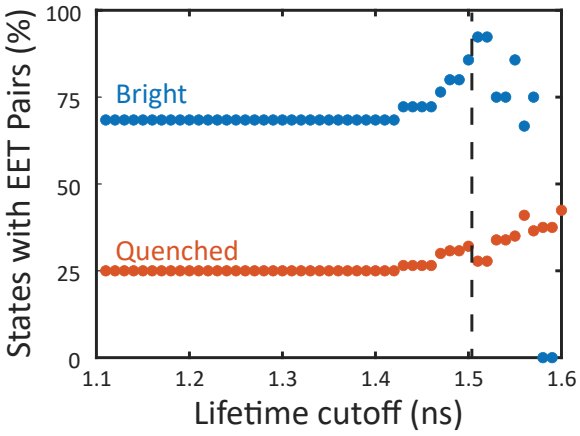

Figure 3-23: **Selection of optimum lifetime cutoff.** The total data set was divided into bright and quenched populations based on a lifetime cutoff. The percent of photophysical states with an intact energy transfer pair was calculated for both populations as a function of the value of the lifetime cutoff. The maximum difference between the bright and quenched populations was observed with a cutoff $\geq$1.50 ns, where 86% of states in the bright population have energy transfer pairs whereas only 32% in the quenched population have energy transfer pairs.

3.6.4 Kinetic model of energetic relaxation and energy transfer

The ultrafast dynamics of energetic relaxation due to nuclear motion and energy transfer were described with a kinetic model. Photoexcitation was assumed to generate a Gaussian population in the excited state. The energetic relaxation of the excited-state population was described as a time-dependent red shift of the population, *i.e.*, the Stokes shift. The energy transfer was described as a time-dependent decrease in population amplitude. Therefore, the evolution of the photoexcited population is modeled as:

$$F(t,E) = Ae^{-k_{EET}t}e^{-\frac{(E-E_0(t))^2}{2c^2}} \tag{3.15}$$

where A is the initial amplitude, which is set to 1, k_{EET} is the energy transfer rate from β to α, c is the standard deviation describing the width of our excitation spectrum, and $E_0(t)$ is the center of the Gaussian population as a function of time,

t. The spectral evolution is described as an exponential decay based on the dynamics observed in ensemble measurements [86], and is given by:

$$E_0(t) = E_{rel} + E_{ER}e^{-k_{ER}t} \tag{3.16}$$

where E_{rel} is the final energy after energetic relaxation due to nuclear motion and E_{ER} is the magnitude of the energetic shift, which occurs with a a rate k_{ER}. The ensemble measurements of energetic relaxation over $\sim$ 250 cm^{-1} extracted a timescale of $\sim$ 250 fs, which is similar to the timescale from the Gaussian mixture model fit of the SM2P distributions [86]. Using Eqtns 3.15 and 3.16, we calculated the kinetics of the system with the experimentally-measured rates of $\sim$0.007 fs^{-1} for energy transfer and $\sim$0.003 fs^{-1} for energetic relaxation. The population transferred was monitored via the amplitude decrease of the Gaussian distribution while the energetic relaxation due to nuclear motion was monitored via the spectral position of the peak of the distribution. The percentage of population transferred and of energetic relaxation, or Stokes shift, completed are plotted as a function of time in Fig. 2e. By 600 fs, energy transfer is almost complete whereas only $\sim$ 20% of the energetic relaxation has occurred, illustrating the relative timescales of these two processes.

Chapter 4

Identification of photo-induced quenching in single light-harvesting complexes from cryptophyte algae

4.1 Chapter Summary

Photosynthetic organisms use pigment-protein complexes to convert sunlight and carbon dioxide into the energy that powers most life on earth. These pigment-protein complexes control the chemical structure, orientation, and position of the attached pigments to optimize safe light harvesting. Additionally, these bio-molecules undergo asynchronous conformational dynamics on disparate length- and timescales that control pigment position and orientation to regulate energy transfer dynamics. Single-molecule spectroscopy provides the opportunity to watch these conformational changes in real-time by removing ensemble averaging. In this work, we used single-molecule fluorescence spectroscopy to identify photophysical substates and the subsequent dynamics present in phycoerythrin 545 (PE545) from cryptophyte algae. These first single-molecule experiments on pigment-protein complexes from cryptophyte algae found similar quenching and photobleaching patterns to proteins from the evolutionarily related cyanobacteria and red algae. These results imply that

light-harvesting complexes from cryptophytes maintain the ability to regulate light harvesting through quenched states that prevent excess sunlight from damaging the light-harvesting machinery. This mechanism could allow for the dissipation of excess excitation and be a built-in safety switch for maintaining the proteins within the lumen. Future work on various subunits may inform upon how pigment makeup, structure, and available dynamics lead to efficient light-harvesting in these robust organisms.

4.2 Introduction

Cryptophytes are microalgae that are ubiquitous in diverse aquatic environments [119]. They are thought to have originated from multiple endosymbiotic events in which cyanobacteria were engulfed by red algae and subsequently eventually evolved into the current organism, which is essentially a chloroplast [114]. In contrast to most photosynthetic organisms in which the light-harvesting apparatuses are organized by membranes or linker proteins, the light-harvesting proteins of cryptophytes are densely packed within the luminal space without any higher order structure [115–118], leading to open questions about access by the protein machinery required for regulation and repair, and thus how cryptophyte light-harvesting proteins are robust under high light. The diverse environments where cryptophytes flourish have evolved a set of proteins with light-harvesting properties tuned to capture sunlight in different ecological niches [114]. The light-harvesting proteins, known as phycobiliproteins (PBPs), contain phycobilin pigments covalently attached to a protein backbone with variations in the pigment identity, their position within the protein scaffold, and the structure of the scaffold itself [115–118, 156]. Although the overall structure and photophysics of several PBPs have been characterized, structural fluctuations are typical for a protein at physiological temperatures, and the impact of these fluctuations on the photophysics, if any, has not been investigated. Furthermore, how these photophysics vary under different conditions, such as high light, has not been determined.

The essential function of the PBPs is to capture sunlight and transfer the pho-

toenergy to the reaction center, which initiates the biochemical reactions of photosynthesis. Energy transfer and other photophysical pathways depend sensitively on the positions of the pigments and the surrounding scaffold. As a result, structural fluctuations are expected to vary the energy transfer dynamics, yet ensemble measurements average over these fluctuations, obfuscating the conformational heterogeneity. Single-molecule methods have, therefore, emerged as a powerful tool to investigate heterogeneous sub-populations and reveal underlying conformational states dynamics [156, 216–221]. The advent of multi-parameter single-molecule techniques that simultaneously measure variables such as fluorescence intensity, lifetime, spectra and polarization has revealed a rich and dynamic energy landscape with different functional conformations [155, 170, 222–224]. Previous single-molecule experiments on PBPs from cyanobacteria and red algae have found a wealth of heterogeneous behaviors including quenching radical cations, interconversion between functional states [170, 195], and even long-lived (ms – s) quenched states of the light-harvesting apparatuses [196, 225, 226].

One of the most widely studied cryptophyte PBPs is phycoerythrin 545 (PE545), so-called for its absorption maximum at ∼545 nm. The structure of PE545 is dimeric (Figure 4-1a). Each monomer of PE545, as well as the rest of the PBPs, consists of a heterodimer of peptides, known as α and β [119]. PE545 binds two strongly coupled dihydrobiliverdin (DBV) pigments at the monomer-monomer interface and six weakly coupled phycoerythrobilin (PEB) pigments [41, 227, 228]. In addition there are six phycoerythrobilin (PEB) pigments which are identified as the red and orange pigments in Figure 4-1a. The pigments at the distal ends are shown in red as they are believed to be the terminal emitters of PE545 [41, 228].

In this work, we report the single-molecule fluorescence of PE545 from *Rhodomonas* sp. strain CS24, which are the first single-molecule measurements of a cryptophyte protein. These measurements revealed bright, quenched, and highly quenched (off) conformations and rapid transitions between them, establishing the presence of conformational dynamics that influence the photophysics. The population of the off conformation increases with excitation fluence, which may reflect non-radiative path-

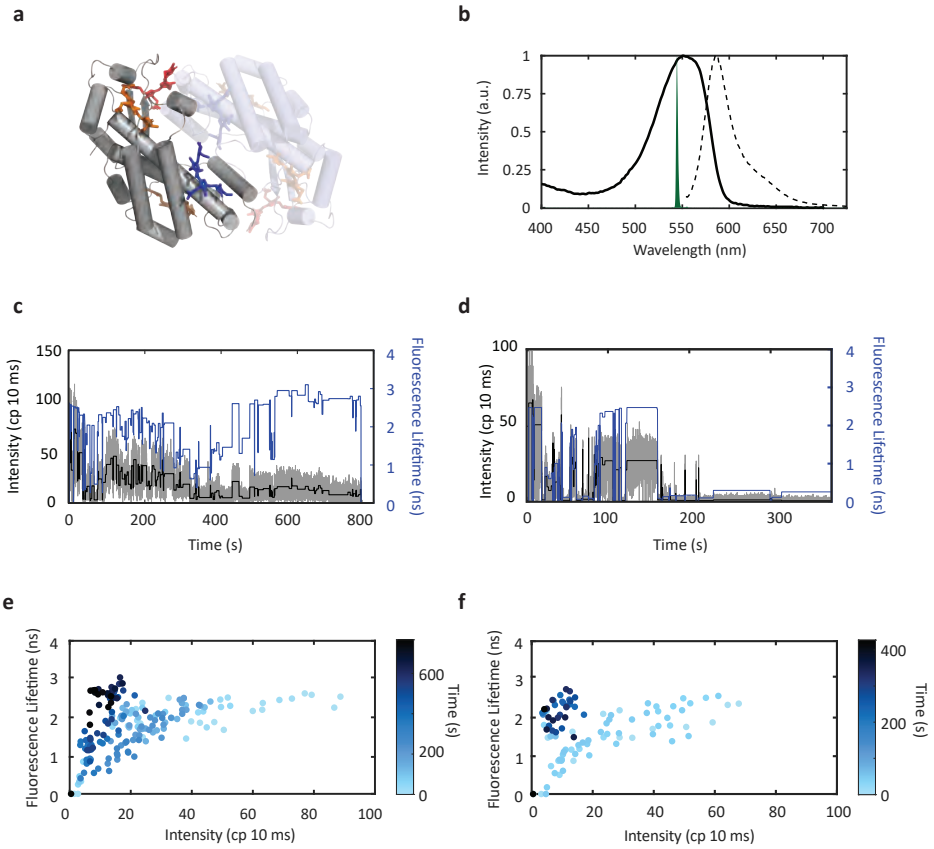

Figure 4-1: **Single-molecule spectroscopy of PE545.** (a) Structure of dimeric PE545 (PDB 1QGW) with monomer subunits in gray and faded blue and pigments in orange and dark blue. (b) Absorption (solid) and emission (dashed) spectra with the excitation laser overlaid in green. (c, d) Representative single-molecule traces of the fluorescence intensity (gray) with the average for each period of constant intensity (black) and the concomitant fluorescence lifetime (blue). (e, f) Corresponding scatter plots of the intensity-lifetime values for each period of constant intensity from the traces in (c) and (d). The colormap indicates the observation time at which the value was detected.

ways that safely dissipate excess energy under high light. In contrast to other PBPs, photodegraded pigments do not quench the other pigments, ensuring robust light harvesting even in the absence of repair mechanisms. These results reveal heterogeneous yet robust behaviors that may contribute to the ability of cryptophyte proteins to capture sunlight under diverse conditions.

4.3 Methods

4.3.1 Single-molecule fluorescence measurements

Solutions of purified PE545 complexes at ∼10 µM were stored at -80°C. The solutions were thawed over ice immediately prior to experiments and diluted to ∼ 500 pM in buffer containing 1% polyvinyl alcohol. An enzymatic oxygen-scavenging system was added for a final concentrations of 25 nM protocatechuate-3,4-dioxygenase and 2.5 mM protocatechuic acid [163, 164].

Single-molecule fluorescence measurements were performed in a home-built confocal microscope. A fiber laser (FemtoFiber pro, Toptica; 130 fs pulse duration, 80 MHz repetition rate) was tuned to 545 nm and set to an excitation power of 10 nW and 30 nW before the microscope (120 nJ/cm2 and 360 nJ/cm2 at the sample plane, respectively, assuming a Gaussian beam). Sample excitation and fluorescence collection were accomplished by the same oil-immersion objective (UPLSAPO100XO, Olympus, NA 1.4). The fluorescence signal was isolated using a dichroic mirror (ZT568rdc-UF3, Chroma) before the objective and a bandpass filter (FF01-600/52-25, Semrock). The signal was detected using an avalanche photodiode (SPCM-AQRH-15, Excelitas) and photon arrival times were recorded using a time-correlated single photon counting module (TimeTagger20, Swabian Instruments). The instrument response function was measured from scattered light to be ∼ 380 ps (full width at half maximum). 170 complexes were measured at 10 nW and 89 complexes at 30 nW.

4.3.2 Analysis of single-molecule data

The detected fluorescence photon stream was analyzed to determine the fluorescence intensity and fluorescence lifetime. Intensity levels were identified using the change-point-finding method developed by Watkins and Yang [229]. The photons collected within each intensity level were then histogrammed to construct a fluorescence decay trace. Each decay was fit to an exponential function convolved with the instrument response function using maximum likelihood estimation to incorporate the effect of

Poissonian noise as described in previous work [207]. To check for lifetime fluctuations within states identified through the change-point analysis, photons within a state were binned by every 1000 photons and no significant fluctuations were observed. These lifetime fluctuations are shown in SI Figure 4-4. Two dimensional histograms of different intensity and lifetime parameters were constructed and a two-dimensional kernel density estimation algorithm was used to better visualize the distributions.

4.4 Results and discussion

The absorption and fluorescence spectra are shown in Figure 4-1b overlaid with the excitation laser spectrum. At the low concentrations required for single-molecule investigation, the dimers are expected to have dissociated into monomer subunits [195, 230, 231]. Previous biochemical experiments showed similar steady-state spectra for the monomer and dimer, suggesting that the monomer maintains a similar secondary structure and function as the dimer [232].

Representative single-molecule fluorescence intensity and lifetime traces are shown in Figure 4-1c and d. Rapid transitions of the intensity and lifetime were observed. To visualize the evolution associated with these transitions, fluorescence intensity-lifetime scatter plots were constructed for all intensity levels below the corresponding traces (Figure 4-1e,f). Qualitatively, two types of behaviors were observed. At early observation times (light blues), the complexes exhibited correlated changes in fluorescence intensity and lifetime along with decreasing intensity for similar lifetime values, generating an bounded-exponential-type curve. At later observation times, *i.e.* after extended illumination (dark blues), the fluorescence intensity was significantly reduced, most likely due to photobleached pigments no longer contributing to the absorption cross section.

4.4.1 Emissive states of PE545

To examine the overall distribution of behaviors, two-dimensional histograms were constructed from the concomitantly-measured fluorescence intensity and lifetime val-

ues for all the PE545 complexes (Figure 4-2a, Figure 4-5). The overall profile of the distribution is similar to PBPs from cyanobacteria, which also exhibit a range of bright (high intensity, long fluorescence lifetime) and quenched (low intensity, shorter fluorescence lifetime) states [193–195]. The distributions can be approximately divided into three states: (1) a bright state with an intensity of $\sim$ 35 cp 10 ms and a fluorescence lifetime $\sim$ 2.45 ns, (2) a semi-quenched state with an intensity of $\sim$ 20 cp 10 ms and a fluorescence lifetime of $\sim$ 1.5 ns, and (3) a quenched state with a fluorescence intensity $\sim$ 5 cp 10 ms and a fluorescence lifetime of $\sim$ 0.5 ns. These different emissive states are generally thought to arise from differences in the pigment photophysics and/or protein conformations [156, 195, 196].

The presence of quenched states establishes that PE545 can exist in quenched conformations. Similarly, previous studies of PBPs from cyanobacteria and red algae observed quenched conformations and concluded that the tetrapyrrole pigment on the β subunit can serve as an acceptor for energy transfer and its low quantum yield can give rise to low fluorescence intensities, and thus quenched complexes [194, 195]. These quenched conformations, as well as the quenched conformations of plant light-harvesting proteins, exhibited photoprotective behaviors, which is the safe dissipation of excess energy by oxygenic photosynthetic organisms under high light conditions. Therefore, PBPs of cryptophyte algae exhibit a similar ability to adopt quenched conformations as other photosynthetic proteins, although ensemble measurements indicate they are not directly involved in photoprotection [233].

4.4.2 Characterization of photodegradation

To isolate the influence of photodegradation on the observed distributions, the single-molecule traces were divided based on observation time. The intensity and lifetime values were split into three groups: early times (the first 25% of the experimental trace; Figure 4-2a), intermediate times (25% to 75% of the trace; Figure 4-5b), and late times (75% to 100% of the trace; Figure 4-5c). To determine the changes upon illumination, the difference between the late and early intensity-lifetime histograms was calculated. The resultant difference-density plot is shown in Figure 4-2b. Consis-

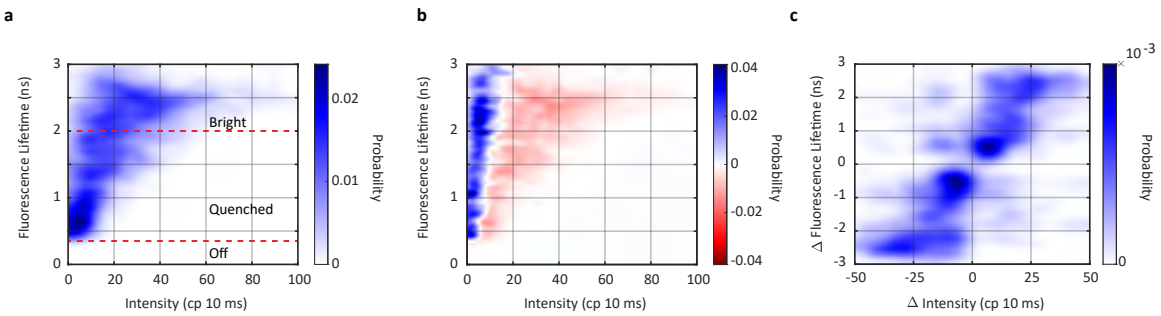

Figure 4-2: **Two-dimensional histograms of intensity and lifetime.** (a) Fluorescence intensity-lifetime probability distribution from measurements of single PE545 (N=170 molecules, M=1835 intensity levels) at low power (10 nW) and early times. (b) Difference-density plot between the estimated probability distributions for late times (final 25%) and early times (initial 25%) of the single-molecule trace. (c) Change in fluorescence intensity-lifetime distributions associated with each change of intensity for PE545 at low power (10 nW) and early times.

tent with the qualitative observations in Figure 4-1e and f, the population at higher intensities decreases (red regions) while the population at lower intensities increases (blue regions), reflecting an overall decrease in intensity. The large slope of the nodal line between the blue and red regions indicates a small shift towards longer lifetime with an overall similar distribution of values. These results show that both bright and quenched conformations in terms of fluorescence lifetime are maintained through the photodegradation process.

4.4.3 Transitions between emissive states

To analyze the ability of PE545 to switch between emissive states, the change in intensity (Δ Intensity) and lifetime (Δ Lifetime) was calculated for each change in intensity levels. The values for all the transitions were used to construct the histogram as shown in Figure 4-2c. In this plot, the upper right quadrant contains transitions to brighter and longer lifetime states while the bottom left quadrant contains transitions to dimmer and shorter lifetime states, *i.e.* shifts into more quenched conformations. The lack of significant population in the other two quadrants reflects correlated changes for intensity and lifetime, as expected from changes in the rate of non-radiative decay.

In figure 4-2c, the features can be described as four peaks. The peaks are easily understood as transitions reflected diagonally across the origin. The upper most peak ($\sim$25 cp 10 ms, $\sim$2.5 ns) corresponds to transitions from the off to the bright state whereas the lower most peak ($\sim$-25 cp 10 ms, $\sim$-2.5 ns) corresponds to transitions from the bright to the off state. The other positive peak, which is a broad feature $<$25 cp 10 ms and $<$2 ns, contains both transitions from the off to the quenched state and from the quenched to the bright state. Similarly, the other below negative peak, which is also a broad feature $<$-25 cp 10 ms and $<$-2 ns, contains both transitions from the quenched to the off state and from the bright to the quenched state. For both features, the high intensity region near the origin is due to transitions within the states.

Therefore, three types of transitions were observed: (1) dynamics between emissive (bright, quenched) states, which likely reflects conformational changes of PE545; (2) blinking, which is the reversible switching into an off state from the emissive states; and (3) photobleaching, which is an intensity decrease within a lifetime state. We ascribe a transition to lower intensity to photodegradation due to the overall intensity decrease upon illumination, as described above and illustrated in Figure 4-2b.

Overall, the presence of significant population across the diagonal line indicates a high degree of connectivity between the states, *i.e.*, transitions occur between all states. Furthermore, the similar populations on both sides of the origin reveals that the majority of these transitions are reversible. In contrast to other PBPs where degradation into lower intensity and shorter lifetime states was primarily observed, PE545 exhibits reversible dynamics, likely reflecting additional conformational dynamics for this protein.

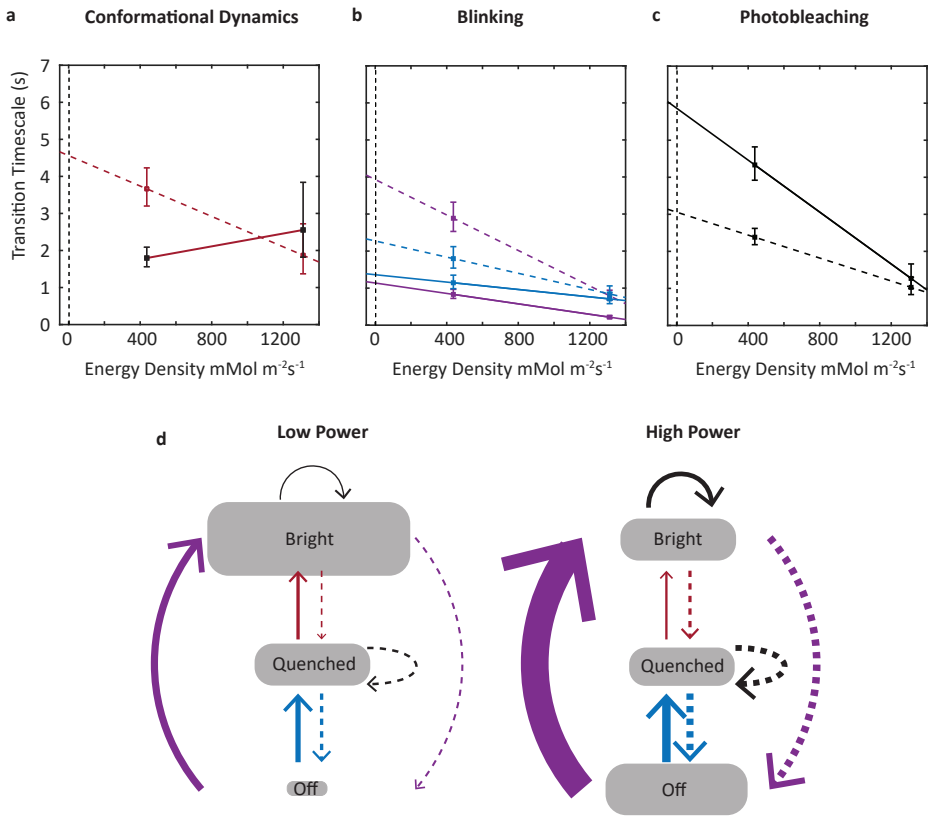

Figure 4-3: **Emissive states and dynamics.** (a) Timescales for transitions between the bright and quenched states. (b) Timescales for transitions into and out of the off state, i.e., blinking. The power dependence of the transitions out of the off state indicates the protein remains photoactive. (c) Timescales for transitions within a single emitting state, i.e., intensity decreases without a lifetime change, which predominantly arise from pigment photobleaching. Error bars show 95% confidence intervals and the dashed vertical line at 2 $mMol\ m^{-2}s^{-1}$ indicates the energy density of sunlight. (d) Schematic indicating the emissive states and their transitions for the two power conditions. The relative population fractions in each state are indicated by the size of oval and the relative timescales of the transitions are indicated by the thickness of the arrows.

4.4.4 Kinetics of transitions between emissive states

To further characterize the dynamics associated with the transitions observed in Figure 4-2c, the timescales were quantified for each transition. The dwell times, which are the duration of the intensity level prior to a transition, were calculated for all transitions [216]. For each combination of initial and final states, a histogram of dwell times was constructed and fit to an exponential probability distribution using

maximum likelihood estimation. An example histogram with the corresponding fit is shown in Figure 4-7 and the extracted timescales for all transitions are plotted in Figure 4-3a-c and shown along with the relative populations in the schematics in Figure 4-3d and e. All transitions were found to occur on timescales of one to five seconds.

The timescale calculations shown in Figure 4-3 were limited to the early times (first 25%) of the single-molecule traces to minimize the influence from photodegraded PE545 on the extracted rates. The rates for early, intermediate, and late times are plotted in Figure 4-8. The timescales all slowed as a function of observation time, likely due to photobleaching of pigments that removed their contribution to the system and thereby reduced the number of pathways available.

The single-molecule measurements were performed at two different powers of the excitation laser, 10 mW (400 mM $m^{-2}s^{-1}$) and 30 mW (1200 mM $m^{-2}s^{-1}$), and the rates were determined for both data sets. To determine the power dependence of all types of transitions, the values at both powers were fit to a linear function. Analysis of these fits enable photoinduced and thermal dynamics to be distinguished, as they give rise to negative and near-zero slopes, respectively. Furthermore, the linear functions from the fits were used to extrapolate the rates to the energy density of sunlight [196]. From this extrapolation, all transitions are predicted to occur on timescales of one to six seconds, indicating that the dynamics observed here are relatively frequent under physiological conditions.

For the conformational dynamics between the bright and quenched states, the bright to quenched transition becomes approximately twice as frequent ($\sim$2 sec to $\sim$4 sec) at higher powers, indicating a photoinduced process. In contrast, no significant change was found for the $\sim$2.5 sec timescale of the quenched to bright transition, indicating a thermal process. For the blinking dynamics, transitions between the bright and off states become approximately four times as frequent at higher powers whereas the transitions between the quenched and off states become approximately three times as frequent. Therefore, the blinking dynamics are all photoinduced. Notably, the photoinduced nature of the transitions from the off state to the quenched

and bright states suggests that the off state state is actually a 'strongly-quenched' state as it retains its photoactivity.

Overall, the changes to the conformational and blinking dynamics at higher power lead to a re-equilibration of the population from the bright state into the off (or strongly-quenched) state. While cyanobacteria and red algae can quickly repair or replace damaged PBPs, experiments have shown that PBPs within cryptophytes are not as mobile as the phycobilisome [234]. The switch to more quenched states could allow for safe dissipation of excess excitation energy preventing photodamage and making replacement mechanisms superfluous.

Lastly, for the photobleaching dynamics, which are the intensity decreases within the lifetime states, the transitions become much more frequent at higher powers, as expected for this process. The transitions in the bright state increase by a factor of 3.4, while the transitions in the quenched state increase by a factor of 2.3. The ratio of the lifetimes (2.5 ns to 1.5 ns, or 1.7) is approximately the same as the ratio of the increase in transitions (3.4 to 2.3, or 1.5), which indicates that photobleaching scales with the time spent in the excited state. Consistently, the blinking dynamics are faster for the bright to off transition than the quenched to off one, indicating a similar scaling may be present.

Previous work on PBPs from cyanobacteria and red algae observed photodegradation through two processes: (1) an intensity decrease, assigned to pigment photobleaching as observed here; and (2) a correlated decrease in intensity and lifetime, assigned to photo-induced and irreversible conversion of pigments into quenchers [193–195]. The second of these processes was not observed in PE545, indicating that photodegradation for this complex has a smaller impact of the photophysics than for other PBPs. Altogether, these results imply a complex set of transitions in PE545 that involve both conformational dynamics and the ability to activate photoprotective quenching.

4.5 Conclusion

In this work we used single-molecule fluorescence spectroscopy to identify emissive states and dynamics of the light-harvesting complex PE545 from cryptophyte algae. By simultaneously monitoring the fluorescence intensity and lifetime of single complexes, we can identify states and monitor the transitions between them. From these measurements, conformational dynamics were discovered as well as photodegradation pathways in which pigments are energetically removed from the coupled system. Lastly, the transition timescales revealed a photo-induced bias towards quenched states, which could work to safely dissipate excess excitation energy.

The diverse environments that cryptophyte algae thrive in has led to a homologous proteins with distinct energetics to efficiently harvest solar energy in each ecological ninche. While early studies have characterized how larger structural changes affect spectra and ultrafast dynamics, these results provide a first look at the underlying conformational dynamics that have the potential to adapt to different light intensities without complex regulation and repair machinery. Future work on the homologous proteins may inform upon how pigment makeup, structure, and available dynamics have been optimized in these organisms.

4.6 Supplemental Information

4.6.1 No Significant Fluorescence Lifetime Fluctuations within Individual States

Because the change-point algorithm by Watkins and Yang only uses the fluorescence intensity, it is possible that it obscures fluorescent lifetime changes at constant intensity. Previous fluctuations in the fluorescence lifetime were found in allophycocyanin and were reported to be the result of the effect of micorscopic configurations on the fluorescent lifetime [193]. To check for these fluorescent lifetime fluctuations, photons from a single identified change-point intensity level were binned by every 1000 photons. These 1000 photons were then histogrammed based on their relative arrival

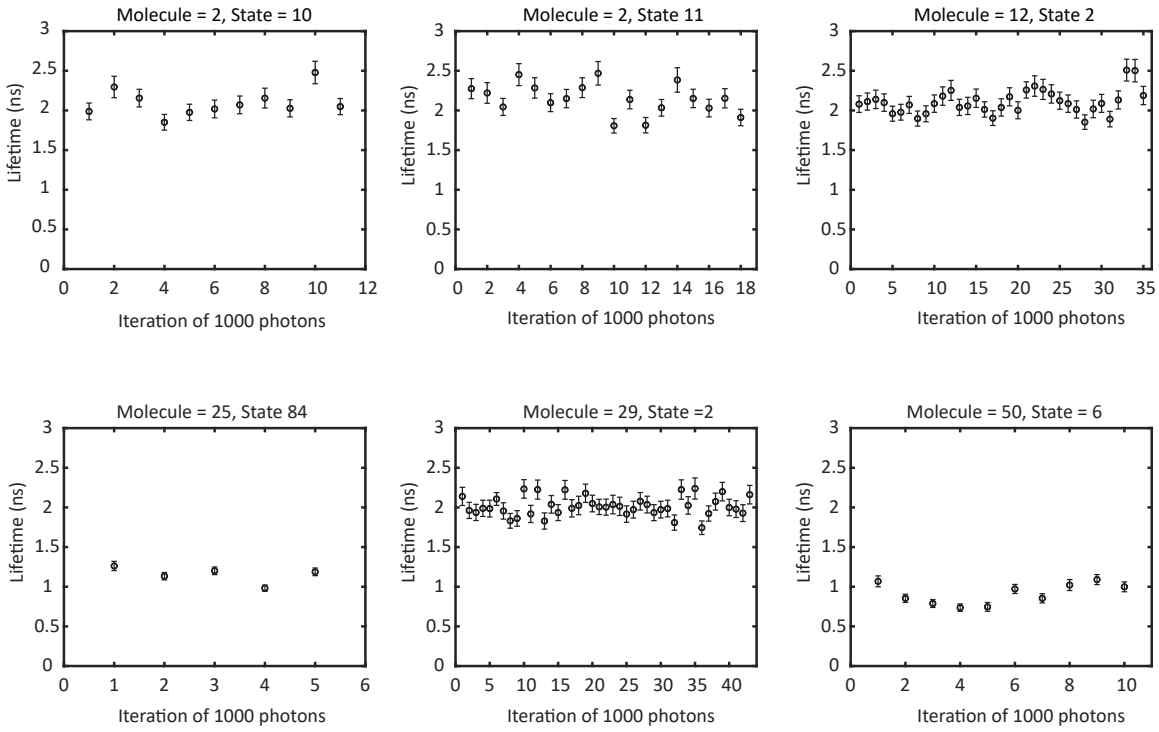

Figure 4-4: **Fluorescence Lifetime within single intensity levels.** To guarantee that there were no significant lifetime levels within single intensity levels found through our change point algorithm,the relative photon arrival time within single levels were histogrammed for every 1000 photons. Several examples are plotted with as a function of 1000 photons with the error bars indicating the standard error of the fit. While some small fluctuations can be seen, no significant changes in fluorescence lifetime were observed.

time and were fit to an exponential function convolved with the system instrument response function as described in Chapters 2 and 3. No significant lifetime fluctuations were observed. Figure 4-4 plots the fluorescence lifetime for every 1000 photons for 6 different molecules and change point levels. The error bars indicate the standard error of the fit and show little fluctuations within a single level.

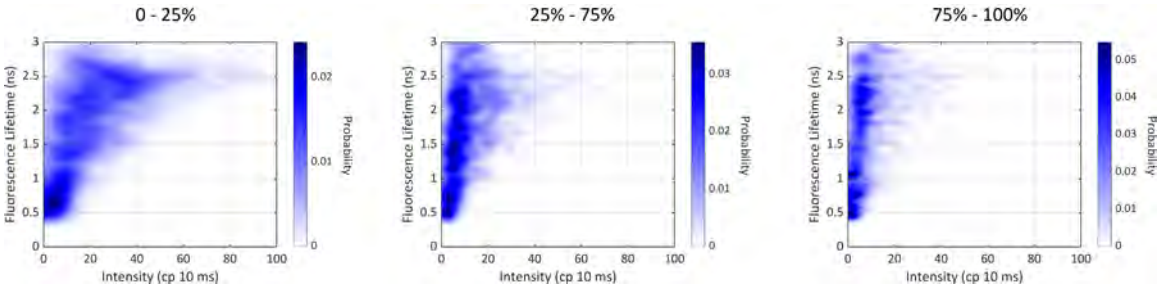

Figure 4-5: **Intensity-lifetime histograms throughout the extent of the experiment for Low Power Experiments.** To disentangle the effects of photobleaching,intensity-lifetime histograms were built for portion of the traces. Intensity-lifetime data points were separated based on the arrival time within the survival time of their individual single-molecule experiments. These results are histogrammed above for 0-25%, 26-75%, and 76% to the end. As the traces approach the final photobleaching states, they maintain access to long-lifetime unquenched states, but lose intensity, mostly likely due to the removal of pigment absorption through photobleaching.

4.6.2 Intensity-Lifetime Distribution Observed throughout the Measurement Time

Immobilizing the single light-harvesting complexes on the surface of the glass coverslip allows the measurement to directly observe the inevitable photobleaching. Because we don't want this photobleaching to affect our analysis, the distribution was separated based on the experimental measurement time. The resulting Intensity-Lifetime histograms are shown in Figure 4-5. To build these distributions, the intensity-lifetime data points were filtered based on their arrival time within in any single-molecule experimental trace. This was done to highlight effect of photobleaching as these distributions highlight how the system loses access to higher intensity states the longer the molecule lives due to subsequent photobleaching of active pigments. The distributions for the high power data are shown below in Figure 4-6 as well.

4.6.3 Determination of Transition Timescales

Information regarding the dynamics of interstate transitions is contained within the dwell time dynamics. That is, the change-point algorithm identifies times of constant fluorescent intensity, and the time spent in this specific state can report on

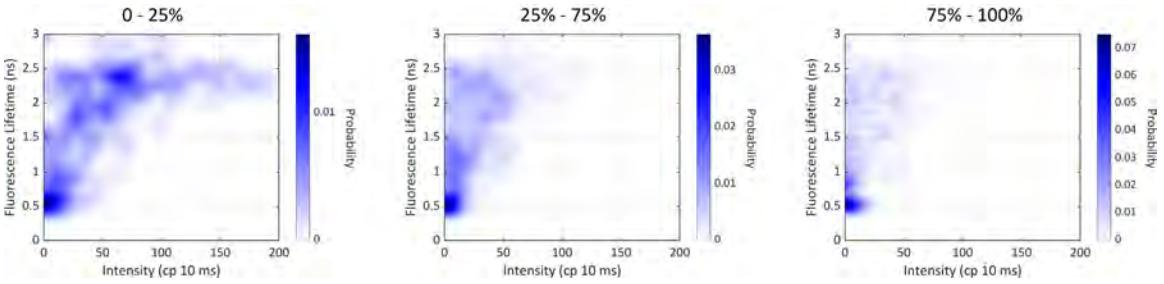

Figure 4-6: **Intensity-lifetime histograms throughout the extent of the experiment for High Power Experiments.** To disentangle the effects of photobleaching,intensity-lifetime histograms were built for portion of the traces. Intensity-lifetime data points were separated based on the arrival time within the survival time of their individual single-molecule experiments. These results are histogrammed above for 0-25%, 26-75%, and 76% to the end. As the traces approach the final photobleaching states, they maintain access to long-lifetime unquenched states, but lose intensity, mostly likely due to the removal of pigment absorption through photobleaching.

the transition dynamics. By assigning states to the initial and final transitions we can extract the transition timescale from the initial to final state. Figure 4-7 shows details a histogram of the dwell times for intensity levels that started in Bright state and ended in an Off State. The dashed line shows a maximum-likelihood estimation of the distribution assuming an exponential distribution. This procedure was completed for all change-point levels and used to build the statistics for the analysis in this manuscript. In Figure 4-8 we detail the change transition timescales based on the the measurement observation time of any individual single-molecule experiment. All transitions detail a slowing down of the transition timescale as a function of measurement time. Note that the Off to Off transitions report on intensity fluctuations within weakly emitting states. While these intensity levels can be identified through the change-point algorithm, it is difficult to assign a robust analysis or identifying mechanism due to experimental noise.

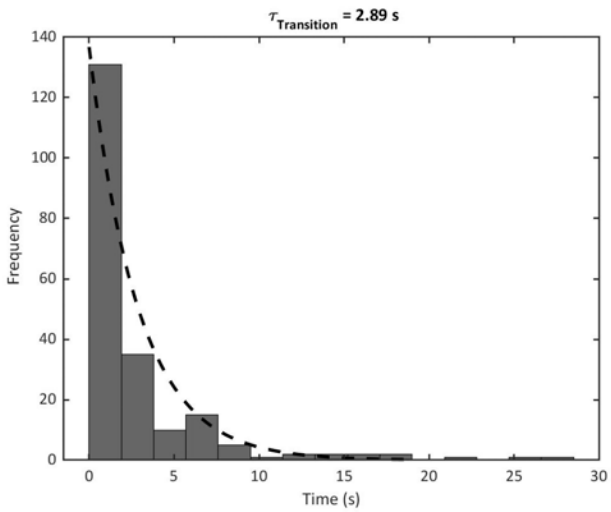

Figure 4-7: **Extracting the timescale for the Bright to Off Transition through intensity dwell time.** The dwell time for intensity levels in the Bright state that transition to the Quenched state were histogrammed and fit to an exponential distribution to recover the transition timescale of 2.89 s.

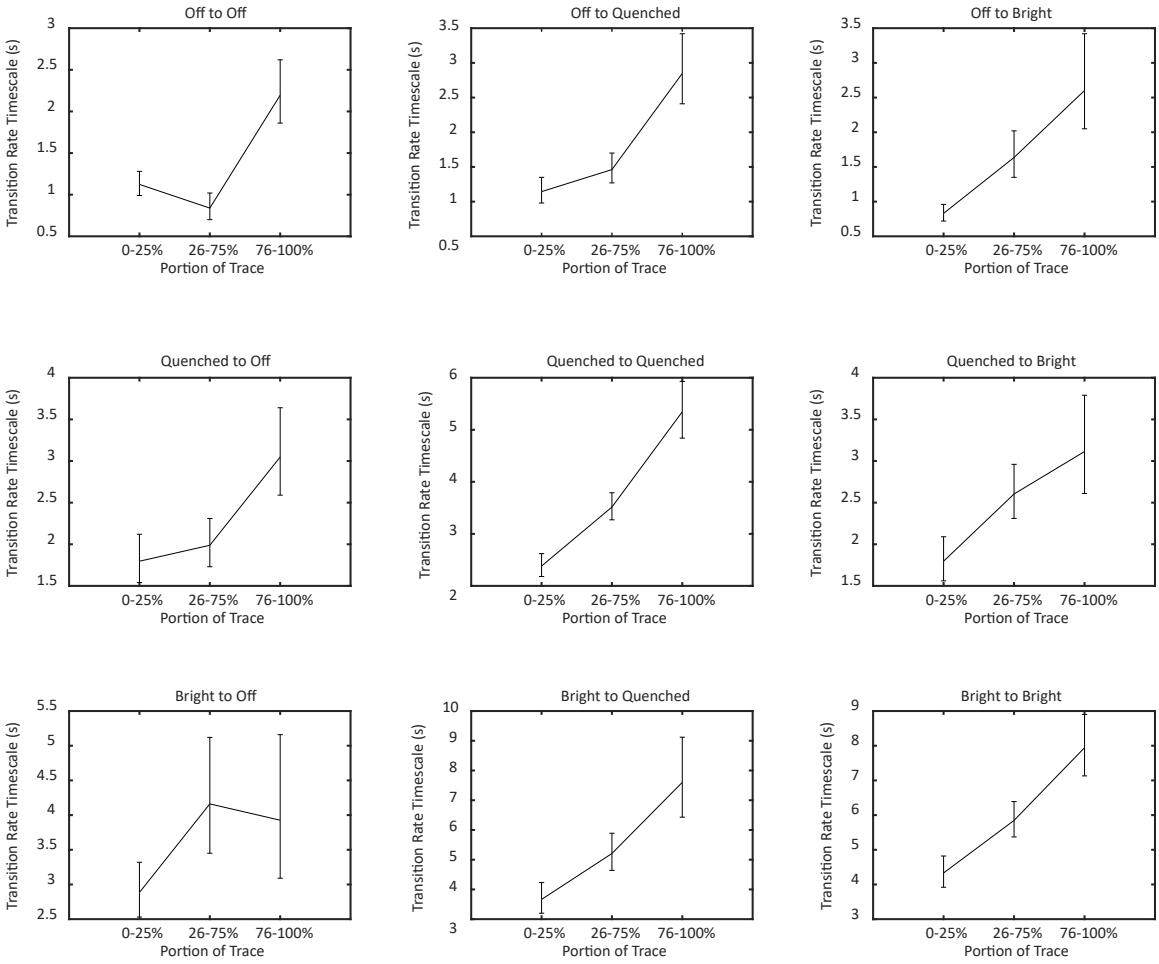

Figure 4-8: **Transition timescales dependence on Time.** The dwell times of the identified change points were used to calculate transition timescales between states. The longer the complexes lived, the slower the transitions. This is most easily explained by photobleaching removing pathways for specific transitions. Error bars indicate 95% confidence intervals.

Chapter 5

Conclusions and Outlook

This work serves as a stepping stone in advancing the unity of single-molecule and ultrafast spectroscopy. Combining these disparate time- and length-scales, these experiments provide a first look at heterogeneity in ultrafast chemical processes. Specifically, we developed a spectrally tunable version of single-molecule pump-probe spectroscopy, a technique that accesses the ultrafast dynamics of single emitters. These experiments revealed multi-timescale relaxation within single fluorophores with heterogeneity less than the Poissonian noise. This suggests the time constants of the early-time processes are insensitive to the local environment. As the fluorescence signal is limited by the number of detected photons, we performed a first silumative study of how the limited signal affects the recovered timescales. This analysis lays the groundwork for accurately, and robustly, recovering meaningful understanding from these experiments. We hope that these statistical considerations will provide insight into future analysis.

We utilized this technique to investigate the complex ultrafast dynamics of light-harvesting complexes. We performed experiments on APC, to see that longer timescale vibrational relaxation takes longer and is more distributed than vibrational relaxation in simple fluorophores. Moreover, filtering APC traces for pristine-like APC suggests that an ultrafast energy transfer component is present at $\sim$ 159 fs and is rigidly controlled by the protein backbone. These experiments set forth an investigation of physical properties that were previously unidentified. With this novel tool, the ability

to probe heterogeneous substates and the asynchronous dynamics nature employs will provide fundamental insight into the efficacy of photosynthesis.

Moving forward, the versatility of our SM2P set-up allows for the investigation into the distribution of energetic relaxation time constants for a multitude of optical systems. The expanded spectral range will enable studies of photosynthetic proteins from many different species, such as the various light-harvesting complexes from plants. Additionally, advances in ultrafast spectroscopy may provide pathways for better temporal resolution and investigation of electronic or vibrational coherences as seen in typical pump-probe like experiments. How the slow asynchronous dynamics of the environment control ultrafast processes like energy and charge transfer, is now a question we can ask.

Bibliography

[1] Barber, J. Photosynthetic energy conversion: natural and artificial. *Chem. Soc. Rev.* **38**, 185–196 (2009).

[2] Barber, J. Biological solar energy. *Philos. T. R. Soc. A* **365**, 1007–1023 (2007).

[3] Blankenship, R. E. *et al.* Comparing photosynthetic and photovoltaic efficiencies and recognizing the potential for improvement. *Science* **332**, 805–809 (2011).

[4] Blankenship, R. E. *Molecular Mechanisms of Photosynthesis* (John Wiley & Sons, 2014).

[5] Van Grondelle, R., Bergström, H., Sundström, V. & Gillbro, T. Energy transfer within the bacteriochlorophyll antenna of purple bacteria at 77 k, studied by picosecond absorption recovery. *Biochim. Biophys. Acta Bioen.* **894**, 313–326 (1987).

[6] Cogdell, R. J., Gall, A. & Köhler, J. The architecture and function of the light-harvesting apparatus of purple bacteria: from single molecules to *in vivo* membranes. *Quart. Rev. Biophys.* **39**, 227–324 (2006).

[7] Scholes, G. D. & Fleming, G. R. On the mechanism of light harvesting in photosynthetic purple bacteria: B800 to b850 energy transfer. *J. Phys. Chem. B* **104**, 1854–1868 (2000).

[8] Blankenship, R. E. *Molecular Mechanisms of Photosynthesis* (Blackwell Publishing, 2002).

[9] van Amerongen, H., Valkunas, L. & van Grondelle, R. *Photosynthetic Excitons* (World Scientific, Singapore, 2000).

[10] Cheng, Y.-C. & Fleming, G. R. Dynamics of light harvesting in photosynthesis. *Annu. Rev. Phys. Chem.* **60**, 241–262 (2009).

[11] Ahn, T. K. *et al.* Architecture of a charge-transfer state regulating light harvesting in a plant antenna protein. *Science* **320**, 794–797 (2008).

[12] Croce, R. & Van Amerongen, H. Natural strategies for photosynthetic light harvesting. *Nat. Chem. Biol.* **10**, 492 (2014).

[13] Noy, D., Moser, C. C. & Dutton, P. L. Design and engineering of photosynthetic light-harvesting and electron transfer using length, time, and energy scales. *Biochim. Biophys. Acta Bioen.* **1757**, 90–105 (2006).

[14] Scholes, G. D., Fleming, G. R., Olaya-Castro, A. & Van Grondelle, R. Lessons from nature about solar light harvesting. *Nat. Chem.* **3**, 763 (2011).

[15] Fleming, G. R., Schlau-Cohen, G. S., Amarnath, K. & Zaks, J. Design principles of photosynthetic light-harvesting. *Faraday Discuss.* **155**, 27–41 (2012).

[16] Ishizaki, A., Calhoun, T. R., Schlau-Cohen, G. S. & Fleming, G. R. Quantum coherence and its interplay with protein environments in photosynthetic electronic energy transfer. *Phys. Chem. Chem. Phys.* **12**, 7319–7337 (2010).

[17] Ishizaki, A. & Fleming, G. R. On the interpretation of quantum coherent beats observed in two-dimensional electronic spectra of photosynthetic light harvesting complexes. *J. Phys. Chem. B* **115**, 6227–6233 (2011).

[18] Novoderezhkin, V. I., Romero, E., Dekker, J. P. & van Grondelle, R. Multiple charge-separation pathways in photosystem ii: Modeling of transient absorption kinetics. *Chem. Phys. Chem.* **12**, 681–688 (2011).

[19] Novoderezhkin, V. I. & van Grondelle, R. Physical origins and models of energy transfer in photosynthetic light-harvesting. *Phys. Chem. Chem. Phys.* **12**, 7352–7365 (2010).

[20] Şener, M. *et al.* Förster energy transfer theory as reflected in the structures of photosynthetic light-harvesting systems. *Chem. Phys. Chem* **12**, 518–531 (2011).

[21] Scholes, G. D. Long-range resonance energy transfer in molecular systems. *Annu. Rev. of Phys. Chem.* **54**, 57–87 (2003).

[22] Hu, Z., Engel, G. S., Alharbi, F. H. & Kais, S. Dark states and delocalization: Competing effects of quantum coherence on the efficiency of light harvesting systems. *J. Phys. Chem. Lett.* **148**, 064304 (2018).

[23] Thyrhaug, E., Zidek, K., Dostál, J., Bína, D. & Zigmantas, D. Exciton structure and energy transfer in the fenna–matthews–olson complex. *J. Phys. Chem. Lett.* **7**, 1653–1660 (2016).

[24] Reinders, A., Verlinden, P., Van Sark, W. & Freundlich, A. *Photovoltaic Solar Energy: From Fundamentals to Applications* (John Wiley & Sons, 2017).

[25] Del Alamo, J. A. Nanometre-scale electronics with iii–v compound semiconductors. *Nature* **479**, 317 (2011).

[26] Wong, C. Y., Cotts, B. L., Wu, H. & Ginsberg, N. S. Exciton dynamics reveal aggregates with intermolecular order at hidden interfaces in solution-cast organic semiconducting films. *Nat. Comm* **6**, 5946 (2015).

[27] Penwell, S. B., Ginsberg, L. D., Noriega, R. & Ginsberg, N. S. Resolving ultrafast exciton migration in organic solids at the nanoscale. *Nat. Mater.* **16**, 1136 (2017).

[28] Brédas, J.-L., Norton, J. E., Cornil, J. & Coropceanu, V. Molecular understanding of organic solar cells: the challenges. *Acc. Chem. Res.* **42**, 1691–1699 (2009).

[29] Poelking, C. *et al.* Impact of mesoscale order on open-circuit voltage in organic solar cells. *Nat. Mater.* **14**, 434 (2015).

[30] Lee, S., Zhitomirsky, D. & Grossman, J. C. Manipulating electronic energy disorder in colloidal quantum dot solids for enhanced charge carrier transport. *Adv. Funct. Mater.* **26**, 1554–1562 (2016).

[31] Glazer, A. N. Light guides. directional energy transfer in a photosynthetic antenna. *J. Biol. Chem.* **264**, 1–4 (1989).

[32] Feng, X. *et al.* Spectroscopic study of the cp43 complex and the psi–cp43 supercomplex of the cyanobacterium synechocystis pcc 6803. *J. Phys. Chem. B* **115**, 13339–13349 (2011).

[33] Chenu, A. & Scholes, G. D. Coherence in energy transfer and photosynthesis. *Annu. Rev. Phys. Chem.* **66**, 69–96 (2015).

[34] Mohseni, M., Rebentrost, P., Lloyd, S. & Aspuru-Guzik, A. Environment-assisted quantum walks in photosynthetic energy transfer. *J. Chem. Phys.* **129**, 11B603 (2008).

[35] Sessler, J. L., Wang, B. & Harriman, A. Photoinduced energy transfer in associated, but noncovalently-linked photosynthetic model systems. *J. Am. Chem. Soc.* **117**, 704–714 (1995).

[36] Causgrove, T. P., Brune, D. C. & Blankenship, R. E. Förster energy transfer in chlorosomes of green photosynthetic bacteria. *Photochem. Photobiol.* **15**, 171–179 (1992).

[37] Förster, T. Energiewanderung und fluoreszenz. *Naturwissenschaften* **33**, 166–175 (1946).

[38] Kell, A., Khmelnitskiy, A. Y., Reinot, T. & Jankowiak, R. On uncorrelated inter-monomer förster energy transfer in fenna–matthews–olson complexes. *J. Roy. Soc. Interface* **16**, 20180882 (2019).

[39] Braslavsky, S. E. *et al.* Pitfalls and limitations in the practical use of förster's theory of resonance energy transfer. *Photochem. Photobiol. Sci.* **7**, 1444–1448 (2008).

[40] Scholes, G. D., Jordanides, X. J. & Fleming, G. R. Adapting the förster theory of energy transfer for modeling dynamics in aggregated molecular assemblies. *J. Phys. Chem. B* **105**, 1640–1651 (2001).

[41] van Grondelle, R. & Novoderezhkin, V. I. Energy transfer in photosynthesis: experimental insights and quantitative models. *Phys. Chem. Chem. Phys.* **8**, 793–807 (2006).

[42] Mirkovic, T., Ostroumov, E. E., Anna, J. M., van Grondelle, R. & Scholes, G. D. Light absorption and energy transfer in the antenna complexes of photosynthetic organisms. *Chem. Rev.* **117**, 249–293 (2016).

[43] Ishizaki, A. & Fleming, G. R. Unified treatment of quantum coherent and incoherent hopping dynamics in electronic energy transfer: Reduced hierarchy equation approach. *J. Chem. Phys.* **130**, 234111 (2009).

[44] Ogren, J. I. *et al.* Impact of the lipid bilayer on energy transfer kinetics in the photosynthetic protein lh2. *Chem. Sci.* **9**, 3095–3104 (2018).

[45] Son, M., Pinnola, A., Bassi, R. & Schlau-Cohen, G. S. The electronic structure of lutein 2 is optimized for light harvesting in plants. *Chem* (2019).

[46] Myers, J. A. *et al.* Two-dimensional electronic spectroscopy of the d1-d2-cyt b559 photosystem ii reaction center complex. *J. Phys. Chem. Lett.* **1**, 2774–2780 (2010).

[47] Ostroumov, E. E., Mulvaney, R. M., Cogdell, R. J. & Scholes, G. D. Broadband 2d electronic spectroscopy reveals a carotenoid dark state in purple bacteria. *Science* **340**, 52–56 (2013).

[48] Fidler, A. F., Singh, V. P., Long, P. D., Dahlberg, P. D. & Engel, G. S. Probing energy transfer events in the light harvesting complex 2 (lh2) of *Rhodobacter sphaeroides* with two-dimensional spectroscopy. *J. Chem Phys.* **139**, 155101 (2013).

[49] Womick, J. M. & Moran, A. M. Exciton coherence and energy transport in the light-harvesting dimers of allophycocyanin. *J. Phys. Chem. B* **113**, 15747–15759 (2009).

[50] Zhang, Z., Lambrev, P., Wells, K. . L., Garab, G. & Tan, H. Direct observation of multistep energy transfer in lhcii with fifth-order 3d electronic spectroscopy. *Nat. Comm* **6** (2015).

[51] Brixner, T., Stenger, J., Vaswani, H. M., Cho, M. & Blankenship, R. E. Two-dimensional spectroscopy of electronic couplings in photosynthesis. *Nature* **434**, 625–628 (2005).

[52] Ginsberg, N. S., Cheng, Y.-C. & Fleming, G. R. Two-dimensional electronic spectroscopy of molecular aggregates. *Acc. Chem. Res.* **42**, 1352–1363 (2009).

[53] Romero, E. *et al.* Quantum coherence in photosynthesis for efficient solar-energy conversion. *Nat. Phys.* **10**, 676 (2014).

[54] Jimenez, R., van Mourik, F., Yu, J. Y. & Fleming, G. R. Three-pulse photon echo measurements on lh1 and lh2 complexes of *Rhodobacter sphaeroides*: a nonlinear spectroscopic probe of energy transfer. *J. Phys. Chem. B* **101**, 7350–7359 (1997).

[55] Kennis, J. T. M., Streltsov, A. M., Permentier, H., Aartsma, T. J. & Amesz, J. Exciton coherence and energy transfer in the lh2 antenna complex of *Rhodopseudomonas acidophila* at low temperature. *J. Phys. Chem. B* **101**, 8369–8374 (1997).

[56] Niedringhaus, A. *et al.* Primary processes in the bacterial reaction center probed by two-dimensional electronic spectroscopy. *Proc. Natl. Acad. Sci.* **115**, 3563–3568 (2018).

[57] Dahlberg, P. D. *et al.* Mapping the ultrafast flow of harvested solar energy in living photosynthetic cells. *Nat. Comm* **8**, 988 (2017).

[58] Dostál, J., Pšenčík, J. & Zigmantas, D. In situ mapping of the energy flow through the entire photosynthetic apparatus. *Nat. Chem.* **8**, 705 (2016).

[59] Paleček, D., Edlund, P., Westenhoff, S. & Zigmantas, D. Quantum coherence as a witness of vibronically hot energy transfer in bacterial reaction center. *Sci. Adv.* **3**, e1603141 (2017).

[60] Gelzinis, A. *et al.* Mapping energy transfer channels in fucoxanthin–chlorophyll protein complex. *Biochim. Biophy. Acta Bioen.* **1847**, 241–247 (2015).

[61] Kitao, A., Hayward, S. & Go, N. Energy landscape of a native protein: Jumping-among-minima model. *Proteins* **33**, 496–517 (1998).

[62] Ansari, A. *et al.* Protein states and proteinquakes. *Proc. Natl. Acad. Sci.* **82**, 5000–5004 (1985).

[63] Hofmann, C., Aartsma, T. J., Michel, H. & Köhler, J. Direct observation of tiers in the energy landscape of a chromoprotein: a single-molecule study. *Proc. Natl. Acad. Sci.* **100**, 15534–15538 (2003).

[64] Fritsch, K., Friedrich, J., Parak, F. & Skinner, J. Spectral diffusion and the energy landscape of a protein. *Proc. Natl. Acad. Sci.* **93**, 15141–15145 (1996).

[65] Jankowiak, R., Hayes, J. & Small, G. Spectral hole-burning spectroscopy in amorphous molecular solids and proteins. *Chem. Rev.* **93**, 1471–1502 (1993).

[66] Andrews, D. L., Curutchet, C. & Scholes, G. D. Resonance energy transfer: beyond the limits. *Laser Photon. Rev.* **5**, 114–123 (2011).

[67] Delor, M. *et al.* Exploiting chromophore-protein interactions through linker engineering to tune photoinduced dynamics in a biomimetic light harvesting platform. *J. Am. Chem. Soc.* **140**, 6278–6287 (2018).

[68] Noriega, R. *et al.* Manipulating excited-state dynamics of individual light-harvesting chromophores through restricted motions in a hydrated nanoscale protein cavity. *J. Phys. Chem. B* **119**, 6963–6973 (2015).

[69] Dashdorj, N., Yamashita, E., Schaibley, J., Cramer, W. A. & Savikhin, S. Ultrafast optical pump- probe studies of the cytochrome b 6 f complex in solution and crystalline states. *J. Phys. Chem. B* **111**, 14405–14410 (2007).

[70] Allodi, M. A. *et al.* Redox conditions affect ultrafast exciton transport in photosynthetic pigment–protein complexes. *J. Phys. Chem. Lett.* **9**, 89–95 (2017).

[71] Schulten, K. & Tesch, M. Coupling of protein motion to electron transfer: Molecular dynamics and stochastic quantum mechanics study of photosynthetic reaction centers. *Chemical Physics* **158**, 421–446 (1991).

[72] Olbrich, C., Strümpfer, J., Schulten, K. & Kleinekatöer, U. Theory and simulation of the environmental effects on fmo electronic transitions. *J. Phys. Chem. Lett.* **2**, 1771–1776 (2011).

[73] Treutlein, H. *et al.* Chromophore-protein interactions and the function of the photosynthetic reaction center: A molecular dynamics study. *Proc. Natl. Acad. Sci.* **89**, 75–79 (1992).

[74] Khmelnitskiy, A., Reinot, T. & Jankowiak, R. Impact of single-point mutations on the excitonic structure and dynamics in a fenna–matthews–olson complex. *J. Phys. Chem. Lett.* **9**, 3378–3386 (2018).

[75] Jankowiak, R. *et al.* Mutation-induced changes in the protein environment and site energies in the (m) l214g mutant of the rhodobacter sphaeroides bacterial reaction center. *J. Phys. Chem. B* **120**, 7859–7871 (2016).

[76] Valkunas, L., Abramavicius, D. & Mancal, T. *Molecular Excitation Dynamics and Relaxation: Quantum Theory and Spectroscopy* (John Wiley & Sons, 2013).

[77] Pullerits, T. & Freiberg, A. Kinetic model of primary energy transfer and trapping in photosynthetic membranes. *Biophys. J.* **63**, 879–896 (1992).

[78] Renger, T., Madjet, M. E.-A., Am Busch, M. S., Adolphs, J. & Müh, F. Structure-based modeling of energy transfer in photosynthesis. *Photosynth. Res.* **116**, 367–388 (2013).

[79] Colbow, K. Energy transfer in photosynthesis. *Biochim. Biophys. Acta Bioen.* **314**, 320–327 (1973).

[80] Rivera, E., Montemayor, D., Masia, M. & Coker, D. F. Influence of site-dependent pigment–protein interactions on excitation energy transfer in photosynthetic light harvesting. *J. Phys. Chem. B* **117**, 5510–5521 (2013).

[81] Fassioli, F., Nazir, A. & Olaya-Castro, A. Quantum state tuning of energy transfer in a correlated environment. *J. Phys. Chem. Lett.* **1**, 2139–2143 (2010).

[82] Rebentrost, P., Mohseni, M. & Aspuru-Guzik, A. Role of quantum coherence and environmental fluctuations in chromophoric energy transport. *J. Phys. Chem. B* **113**, 9942–9947 (2009).

[83] Kell, A., Blankenship, R. E. & Jankowiak, R. Effect of spectral density shapes on the excitonic structure and dynamics of the fenna–matthews–olson trimer from chlorobaculum tepidum. *J. Phys. Chem. A* **120**, 6146–6154 (2016).

[84] Kell, A., Khmelnitskiy, A., Jassas, M. & Jankowiak, R. Dichotomous disorder versus excitonic splitting of the b800 band of allochromatium vinosum. *J. Phys. Chem. Lett.* **9**, 4125–4129 (2018).

[85] Saer, R. G. *et al.* Probing the excitonic landscape of the chlorobaculum tepidum fenna-matthews-olson (fmo) complex: a mutagenesis approach. *Biochim. Biophys. Acta Bioen.* **1858**, 288–296 (2017).

[86] Edington, M. D., Riter, R. E. & Beck, W. F. Femtosecond transient hole-burning detection of interexciton-state radiationless decay in allophycocyanin trimers. *J. Phys. Chem. B* **101**, 4473–4477 (1997).

[87] Davison, I. R. Environmental effects on algal photosynthesis: temperature. *J. Phycol.* **27**, 2–8 (1991).

[88] Terazono, Y. *et al.* Mimicking the role of the antenna in photosynthetic photoprotection. *J. Am. Chem. Soc.* **133**, 2916–2922 (2011).

[89] Grätzel, M. Molecular photovoltaics that mimic photosynthesis. *Pure App. Chem.* **73**, 459–467 (2001).

[90] Brixner, T., Hildner, R., Köhler, J., Lambert, C. & Würthner, F. Exciton transport in molecular aggregates–from natural antennas to synthetic chromophore systems. *Adv. Func. Mater.* **7**, 1700236 (2017).

[91] Ringsmuth, A., Milburn, G. & Stace, T. Multiscale photosynthetic and biomimetic excitation energy transfer. *Nat. Phys.* **8**, 562 (2012).

[92] Adir, N. Elucidation of the molecular structures of components of the phycobilisome: reconstructing a giant. *Photosynth. Res.* **85**, 15–32 (2005).

[93] Moya, I., Silvestri, M., Vallon, O., Cinque, G. & Bassi, R. Time-resolved fluorescence analysis of the photosystem II antenna proteins in detergent micelles and liposomes. *Biochem.* **40**, 12552–12561 (2001).

[94] MacColl, R. Cyanobacterial phycobilisomes. *J. Struct. Biol* **124**, 311–334 (1998).

[95] Stadnichuk, I., Krasilnikov, P. & Zlenko, D. Cyanobacterial phycobilisomes and phycobiliproteins. *Microbiology* **84**, 101–111 (2015).

[96] Peng, P.-P. *et al.* The structure of allophycocyanin b from *Synechocystis PCC 6803* reveals the structural basis for the extreme redshift of the terminal emitter phycobilisomes. *Acta Crystallogr. Sect. D: Biol. Crystallogr* **70**.

[97] Glazer, A. N. Phycobilisome a macromolecular complex optimized for light energy transfer. *Biochim. Biophys. Acta Rev. Bioen.* **768**, 29–51 (1984).

[98] Brejc, K., Ficner, R., Huber, R. & Steinbacher, S. Isolation, crystallization, crystal structure analysis and refinement of allophycocyanin from the cyanobacterium *Spirulina platensis* at 2.3 åresolution. *J. Molec. Biol.* **249**, 424–440 (1995).

[99] Siegelman, H. W. & Kycia, J. H. Molecular morphology of cyanobacterial phycobilisomes. *Plant Physiol.* **70**, 887–897 (1982).

[100] Gingrich, J. C., Blaha, L. K. & Glazer, A. N. Rod substructure in cyanobacterial phycobilisomes: analysis of synechocystis 6701 mutants low in phycoerythrin. *J. Cell. Biol.* **92**, 261–268 (1982).

[101] Kehoe, D. M. Chromatic adaptation and the evolution of light color sensing in cyanobacteria. *Proc. Natl. Acad. Sci.* **107**, 9029–9030 (2010).

[102] Kehoe, D. M. & Gutu, A. Responding to color: the regulation of complementary chromatic adaptation. *Annu. Rev. Plant Biol.* **57**, 127–150 (2006).

[103] Liu, L.-N. Distribution and dynamics of electron transport complexes in-cyanobacterial thylakoid membranes. *Biochim. Phys. Acta* **1857**, 256–265 (2016).

[104] Liberton, M. *et al.* Probing the consequences of antenna modification in cyanobacteria. *Photosynth. Res.* **118**, 17–24 (2013).

[105] Liberton, M. *et al.* Organization and flexibility of cyanobacterial thylakoid membranes examined by neutron scattering. *J. Biol. Chem.* **288**, 3632–3640 (2013).

[106] Scheer, H. & Zhao, K.-H. Biliprotein maturation: the chromophore attachment. *Mol. Microbiol.* **68**, 263–276 (2008).

[107] Miller, C. A. *et al.* Biogenesis of phycobiliproteins iii. cpcm is the asparagine methyltransferase for phycobiliprotein β-subunits in cyanobacteria. *J. Biol. Chem.* **283**, 19293–19300 (2008).

[108] Soni, B. R. *et al.* Structure of the novel 14 kda fragment of α-subunit of phycoerythrin from the starving cyanobacterium phormidium tenue. *J. Struc. Biol.* **171**, 247–255 (2010).

[109] Sidler, W. A. Phycobilisome and phycobiliprotein structures. In *The Molecular Biology of Cyanobacteria*, 139–216 (Springer, 1994).

[110] De Marsac, N. T. & Cohen-Bazire, G. Molecular composition of cyanobacterial phycobilisomes. *Proc. Natl. Acad. Sci.* **74**, 1635–1639 (1977).

[111] Liu, H. *et al.* Phycobilisomes supply excitations to both photosystems in a megacomplex in cyanobacteria. *Science* **342**, 1104–1107 (2013).

[112] Watanabe, M. & Ikeuchi, M. Phycobilisome: architecture of a light-harvesting supercomplex. *Photosynth. Res.* **116**, 265–276 (2013).

[113] van Grondelle, R., Dekker, J. P., Gillbro, T. & Sundstrom, V. Energy transfer and trapping in photosynthesis. *Biochim. Biophy. Acta Bioen.* **1187**, 1–65 (1994).

[114] Croce, R., Van Grondelle, R., Van Amerongen, H. & Van Stokkum, I. *Light harvesting in photosynthesis* (CRC press, 2018).

[115] Apt, K. E., Collier, J. L. & Grossman, A. R. Evolution of the phycobiliproteins. *Journal of molecular biology* **248**, 79–96 (1995).

[116] Gantt, E., Edwards, M. t. & Provasoli, L. Chloroplast structure of the cryptophyceae: evidence for phycobiliproteins within intrathylakoidal spaces. *The Journal of cell biology* **48**, 280–290 (1971).

[117] Spear-Bernstein, L. & Miller, K. R. Unique location of the phycobiliprotein light-harvesting pigment in the cryptophyceae 1. *Journal of Phycology* **25**, 412–419 (1989).

[118] Vesk, M., Dwarte, D., Fowler, S. & Hiller, R. Freeze fracture immunocytochemistry of light-harvesting pigment complexes in a cryptophyte. *Protoplasma* **170**, 166–176 (1992).

[119] Wilk, K. E. *et al.* Evolution of a light-harvesting protein by addition of new subunits and rearrangement of conserved elements: crystal structure of a cryptophyte phycoerythrin at 1.63-å resolution. *Proceedings of the National Academy of Sciences* **96**, 8901–8906 (1999).

[120] Rathbone, H. W., Michie, K. A., Landsberg, M. J., Green, B. R. & Curmi, P. M. Scaffolding proteins guide the evolution of algal light harvesting antennas. *Nature communications* **12**, 1–9 (2021).

[121] Doust, A. B., Wilk, K. E., Curmi, P. M. & Scholes, G. D. The photophysics of cryptophyte light-harvesting. *Journal of Photochemistry and Photobiology A: Chemistry* **184**, 1–17 (2006).

[122] Wong, C. Y. *et al.* Electronic coherence lineshapes reveal hidden excitonic correlations in photosynthetic light harvesting. *Nature chemistry* **4**, 396–404 (2012).

[123] Jumper, C. C., Van Stokkum, I. H., Mirkovic, T. & Scholes, G. D. Vibronic wavepackets and energy transfer in cryptophyte light-harvesting complexes. *The Journal of Physical Chemistry B* **122**, 6328–6340 (2018).

[124] Bennett, D. I., Maly, P., Kreisbeck, C., Van Grondelle, R. & Aspuru-Guzik, A. Mechanistic regimes of vibronic transport in a heterodimer and the design principle of incoherent vibronic transport in phycobiliproteins. *The journal of physical chemistry letters* **9**, 2665–2670 (2018).

[125] Blau, S. M., Bennett, D. I., Kreisbeck, C., Scholes, G. D. & Aspuru-Guzik, A. Local protein solvation drives direct down-conversion in phycobiliprotein pc645 via incoherent vibronic transport. *Proceedings of the National Academy of Sciences* **115**, E3342–E3350 (2018).

[126] Jumper, C. C. *et al.* Broad-band pump–probe spectroscopy quantifies ultrafast solvation dynamics of proteins and molecules. *J. Phys. Chem. Lett.* **7**, 4722–4731 (2016).

[127] Dean, J. C., Mirkovic, T., Toa, Z. S., Oblinsky, D. G. & Scholes, G. D. Vibronic enhancement of algae light harvesting. *Chem* **1**, 858–872 (2016).

[128] Lakowicz, J. R. *Principles of Fluorescence Spectroscopy* (Springer Science & Business Media, 2013).

[129] Selvin, P. R. & Ha, T. *Single-Molecule Techniques* (Cold Spring Harbor Laboratory Press, 2008).

[130] Mukamel, S. *Principles of Nonlinear Optical Spectroscopy* (Number 6. Oxford University Press, 1999).

[131] Diels, J. C. & Rudolph, W. *Ultrashort Laser Pulse Phenomena* (2006).

[132] Fleming, G. R. *Chemical Applications of Ultrafast Spectroscopy* (Oxford University Press, New York, NY, 1986).

[133] Moerner, W. E. & Orrit, M. Illuminating single molecules in condensed matter. *Science* **283**, 1670–1676 (1999).

[134] Xie, X. S. Single-molecule spectroscopy and dynamics at room temperature. *Acc. Chem. Res.* **29**, 598–606 (1996).

[135] Parson, W. W. *Modern Optical Spectroscopy,* (Springer, 2007).

[136] Hernando, J. *et al.* Effect of disorder on ultrafast exciton dynamics probed by single molecule spectroscopy. *Phys Rev. Lett.* **97**, 216403 (2006).

[137] Accanto, N. *et al.* Phase control of femtosecond pulses on the nanoscale using second harmonic nanoparticles. *Light Sci. Appl.* **3**, e143 (2014).

[138] Gao, B., Hartland, G. V. & Huang, L. Transient absorption spectroscopy and imaging of individual chirality-assigned single-walled carbon nanotubes. *ACS Nano* **6**, 5083–5090 (2012).

[139] Min, W. *et al.* Imaging chromophores with undetectable fluorescence by stimulated emission microscopy. *Nature* **461**, 1105–1109 (2009).

[140] Celebrano, M., Kukura, P., Renn, A. & Sandoghdar, V. Single-molecule imaging by optical absorption. *Nat. Photon* **5**, 95–98 (2011).

[141] Van Dijk, E., Hernando, J., García-Parajó, M. & Van Hulst, N. Single-molecule pump-probe experiments reveal variations in ultrafast energy redistribution. *J. Chem. Phys.* **123**, 064703 (2005).

[142] Hildner, D., R. an dBrinks & van Hulst, N. F. Femtosecond coherence and quantum control of single molecules at room temperature. *Nat. Phys.* **7**, 172–177 (2011).

[143] Brinks, D. *et al.* Visualizing and controlling vibrational wave packets of single molecules. *Nature* **465**, 905–908 (2010).

[144] Hildner, R., Brinks, D., Nieder, J. B., Cogdell, R. J. & van Hulst, N. F. Quantum coherent energy transfer over varying pathways in single light-harvesting complexes. *Science* **340**, 1448–1451 (2013).

[145] Malý, P., Gruber, J. M., Cogdell, R. J., Mančal, T. & van Grondelle, R. Ultrafast energy relaxation in single light-harvesting complexes. *Proc. Natl. Acad. Sci.* **113**, 2934–2939 (2016).

[146] Devadas, M. S. *et al.* Imaging nano-objects by linear and nonlinear optical absorption microscopies. *Nanotechnology* **26**, 354001 (2015).

[147] Beane, G., Devkota, T., Brown, B. S. & Hartland, G. V. Ultrafast measurements of the dynamics of single nanostructures: a review. *Rep. Prog. Phys.* **82**, 016401 (2018).

[148] Guo, Z., Manser, J. S., Wan, Y., Kamat, P. V. & Huang, L. Spatial and temporal imaging of long-range charge transport in perovskite thin films by ultrafast microscopy. *Nature communications* **6**, 7471 (2015).

[149] Guo, Z. *et al.* Long-range hot-carrier transport in hybrid perovskites visualized by ultrafast microscopy. *Science* **356**, 59–62 (2017).

[150] Nah, S. *et al.* Spatially segregated free-carrier and exciton populations in individual lead halide perovskite grains. *Nature Photonics* **11**, 285 (2017).

[151] Nah, S. *et al.* Ultrafast imaging of carrier cooling in metal halide perovskite thin films. *Nano letters* **18**, 1044–1048 (2018).

[152] Doust, A. B. *et al.* Mediation of ultrafast light-harvesting by a central dimer in phycoerythrin 545 studied by transient absorption and global analysis. *The Journal of Physical Chemistry B* **109**, 14219–14226 (2005).

[153] van Oijen, A. M., Ketelaars, M., Köhler, J., Aartsma, T. J. & Schmidt, J. Unraveling the electronic structure of individual photosynthetic pigment-protein complexes. *Science* **285**, 400–402 (1999).

[154] Hofmann, C. *et al.* Single-molecule study of the electronic couplings in a circular array of molecules: light-harvesting-2 complex from rhodospirillum molischianum. *Physical review letters* **90**, 013004 (2003).

[155] Lerner, E. *et al.* Toward dynamic structural biology: Two decades of single-molecule förster resonance energy transfer. *Science* **359** (2018).

[156] Kondo, T., Chen, W. J. & Schlau-Cohen, G. S. Single-molecule fluorescence spectroscopy of photosynthetic systems. *Chem. Rev.* **117**, 860–898 (2017).

[157] Huang, L. *et al.* Ultrafast transient absorption microscopy studies of carrier dynamics in epitaxial graphene. *Nano letters* **10**, 1308–1313 (2010).

[158] van Dijk, E. M. *et al.* Single-molecule pump-probe detection resolves ultrafast pathways in individual and coupled quantum systems. *Phys. Rev. Lett.* **94**, 078302 (2005).

[159] Hildner, R., Brinks, D., Stefani, F. D. & van Hulst, N. F. Electronic coherences and vibrational wave-packets in single molecules studied with femtosecond phase-controlled spectroscopy. *Physical Chemistry Chemical Physics* **13**, 1888–1894 (2011).

[160] Akturk, S., Gu, X., Kimmel, M. & Trebino, R. Extremely simple single-prism ultrashort-pulse compressor. *Optics express* **14**, 10101–10108 (2006).

[161] Guild, J. B., Xu, C. & Webb, W. W. Measurement of group delay dispersion of high numerical aperture objective lenses using two-photon excited fluorescence. *Applied Optics* **36**, 397–401 (1997).

[162] Müller, M., Squier, J. & Brakenhoff, G. Measurement of femtosecond pulses in the focal point of a high-numerical-aperture lens by two-photon absorption. *Opt. Lett.* **20**, 1038–1040 (1995).

[163] Aitken, C. E., Marshall, R. A. & Puglisi, J. D. An oxygen scavenging system for improvement of dye stability in single-molecule fluorescence experiments. *Biophys. J.* **94**, 1826–1835 (2008).

[164] Swoboda, M. *et al.* Enzymatic oxygen scavenging for photostability without ph drop in single-molecule experiments. *ACS nano* **6**, 6364–6369 (2012).

[165] Gelin, M. F., Egorova, D. & Domcke, W. Strong and long makes short: strong-pump strong-probe spectroscopy. *The journal of physical chemistry letters* **2**, 114–119 (2011).

[166] Palacino-González, E., Gelin, M. F. & Domcke, W. Theoretical aspects of femtosecond double-pump single-molecule spectroscopy. ii. strong-field regime. *Physical Chemistry Chemical Physics* **19**, 32307–32319 (2017).

[167] Chen, L., Gelin, M. F., Domcke, W. & Zhao, Y. Simulation of femtosecond phase-locked double-pump signals of individual light-harvesting complexes lh2. *J. Phys. Chem. Lett.* **9**, 4488–4494 (2018).

[168] Dickson, R. M., Cubitt, A. B., Tsien, R. Y. & Moerner, W. E. On/off blinking and switching behaviour of single molecules of green fluorescent protein. *Nature* **388**, 355–358 (1997).

[169] Moerner, W. & Fromm, D. P. Methods of single-molecule fluorescence spectroscopy and microscopy. *Rev. Sci. Inst.* **74**, 3597–3619 (2003).

[170] Wang, Q. & Moerner, W. Lifetime and spectrally resolved characterization of the photodynamics of single fluorophores in solution using the anti-brownian electrokinetic trap. *The Journal of Physical Chemistry B* **117**, 4641–4648 (2013).

[171] Fleming, G. R. & Cho, M. Chromophore-solvent dynamics. *Annual Review of Physical Chemistry* **47**, 109–134 (1996).

[172] Pawitan, Y. *In all likelihood: statistical modelling and inference using likelihood* (Oxford University Press, 2001).

[173] Stratt, R. M. & Cho, M. The short-time dynamics of solvation. *J. Chem. Phys.* **100**, 6700–6708 (1994).

[174] Bagchi, B. Molecular theory of nonpolar solvation dynamics. *The Journal of chemical physics* **100**, 6658–6664 (1994).

[175] Nitzan, A. *Chemical Dynamics in Condensed Phases: Relaxation, Transfer and Reactions in Condensed Molecular Systems* (Oxford university press, 2006).

[176] Lee, Y. *et al.* Ultrafast solvation dynamics and vibrational coherences of halogenated boron-dipyrromethene derivatives revealed through two-dimensional electronic spectroscopy. *Journal of the American Chemical Society* **139**, 14733–14742 (2017).

[177] Lu, J., Lee, Y. & Anna, J. M. Extracting the frequency-dependent dynamic stokes shift from two-dimensional electronic spectra with prominent vibrational coherences. *Journal of Physical Chemistry B* **124**, 8857–8867 (2020).

[178] Zhang, T.-F. *et al.* Broadband photodetector based on carbon nanotube thin film/single layer graphene schottky junction. *Scientific reports* **6**, 1–8 (2016).

[179] Campillo, A. & Shapiro, S. Picosecond fluorescence studies of exciton migration and annihilation in photosynthetic systems. a review. *Photochemistry and Photobiology* **28**, 975–989 (1978).

[180] Tang, C. & Erskine, D. Femtosecond relaxation of photoexcited nonequilibrium carriers in al x ga 1- x as. *Physical Review Letters* **51**, 840 (1983).

[181] Taylor, A., Erskine, D. & Tang, C. Femtosecond vibrational relaxation of large organic molecules. *Chemical physics letters* **103**, 430–435 (1984).

[182] Taylor, A., Erskine, D. & Tang, C. Equal-pulse correlation technique for measuring femtosecond excited state relaxation times. *Applied physics letters* **43**, 989–991 (1983).

[183] Turton, D. A., Reid, G. D. & Beddard, G. S. Accurate analysis of fluorescence decays from single molecules in photon counting experiments. *Analytical chemistry* **75**, 4182–4187 (2003).

[184] Malỳ, P., Gardiner, A. T., Cogdell, R. J., Van Grondelle, R. & Mančal, T. Robust light harvesting by a noisy antenna. *Physical Chemistry Chemical Physics* **20**, 4360–4372 (2018).

[185] Womick, J. M. & Moran, A. M. Vibronic enhancement of exciton sizes and energy transport in photosynthetic complexes. *J. Phys. Chem. B* **115**, 1347–1356 (2011).

[186] Womick, J. M. & Moran, A. M. Nature of excited states and relaxation mechanisms in c-phycocyanin. *J. Phys. Chem. B* **113**, 15771–15782 (2009).

[187] Womick, J. M., Miller, S. A. & Moran, A. M. Toward the origin of exciton electronic structure in phycobiliproteins. *J. Chem. Phys.* **133**, 07B603 (2010).

[188] Edington, M. D., Riter, R. & Beck, W. F. Interexciton-state relaxation and exciton localization in allophycocyanin trimers. *J. Phys. Chem.* **100**, 14206–14217 (1996).

[189] Edington, M. D., Riter, R. E. & Beck, W. F. Evidence for coherent energy transfer in allophycocyanin trimers. *J. Phys. Chem.* **99**, 15699–15704 (1995).

[190] Beck, W. F. & Sauer, K. Energy-transfer and exciton-state relaxation processes in allophycocyanin. *J. Phys. Chem.* **96**, 4658–4666 (1992).

[191] Riter, R. R., Edington, M. D. & Beck, W. F. Protein-matrix solvation dynamics in the α subunit of c-phycocyanin. *J. Phys. Chem.* **100**, 14198–14205 (1996).

[192] Homoelle, B. J., Edington, M. D., Diffey, W. M. & Beck, W. F. Stimulated photon-echo and transient-grating studies of protein-matrix solvation dynamics and interexciton-state radiationless decay in α phycocyanin and allophycocyanin. *J. Phys. Chem. B* **102**, 3044–3052 (1998).

[193] Goldsmith, R. & Moerner, W. Watching conformational- and photodynamics of single fluorescent proteins in solution. *Nat. Chem.* **2**, 179–185 (2010).

[194] Wang, Q. & Moerner, W. Dissecting pigment architecture of individual photosynthetic antenna complexes in solution. *Proc. Natl. Acad. Sci.* **112**, 13880–13885 (2015).

[195] Squires, A. H. & Moerner, W. Direct single-molecule measurements of phycocyanobilin photophysics in monomeric c-phycocyanin. *Proc. Natl. Acad. Sci.* **114**, 9779–9784 (2017).

[196] Gwizdala, M., Berera, R., Kirilovsky, D., Van Grondelle, R. & Kruger, T. P. Controlling light harvesting with light. *J. Am. Chem. Soc.* **138**, 11616–11622 (2016).

[197] Ying, L. & Xie, X. S. Fluorescence spectroscopy, exciton dynamics, and photochemistry of single allophycocyanin trimers. *J. Phys. Chem. B* **102**, 10399–10409 (1998).

[198] Loos, D., Cotlet, M., De Schryver, F., Habuchi, S. & Hofkens, J. Single-molecule spectroscopy selectively probes donor and acceptor chromophores in the phycobiliprotein allophycocyanin. *Biophys. J.* **87**, 2598–2608 (2004).

[199] Xie, S., Du, M., Mets, L. & Fleming, G. R. Femtosecond fluorescence depolarization study of photosynthetic antenna proteins: observation of ultrafast energy transfer in trimeric c-phycocyanin and allophycocyanin. In *Time-Resolved Laser Spectroscopy in Biochemistry III*, vol. 1640, 690–706 (International Society for Optics and Photonics, 1992).

[200] Rancova, O., Jakučionis, M., Valkunas, L. & Abramavicius, D. Origin of non-gaussian site energy disorder in molecular aggregates. *Chemical Physics Letters* **674**, 120–124 (2017).

[201] Curutchet, C. *et al.* Photosynthetic light-harvesting is tuned by the heterogeneous polarizable environment of the protein. *J. Am. Chem. Soc.* **133**, 3078–3084 (2011).

[202] Homoelle, B. J. & Beck, W. F. Solvent accessibility of the phycocyanobilin chromophore in the α subunit of c-phycocyanin: implications for a molecular mechanism for inertial protein-matrix solvation dynamics. *Biochemistry* **36**, 12970–12975 (1997).

[203] Ferwerda, H. A., Terpstra, J. & Wiersma, D. A. Discussion of a "coherent artifact"in four-wave mixing experiments. *J. Chem. Phys.* **91**, 3296–3305 (1989).

[204] Riter, R. E., Edington, M. D. & Beck, W. F. Isolated-chromophore and exciton-state photophysics in c-phycocyanin trimers. *J. Phys. Chem. B* **101**, 2366–2371 (1997).

[205] McGregor, A., Klartag, M., David, L. & Adir, N. Allophycocyanin trimer stability and functionality are primarily due to polar enhanced hydrophobicity of the phycocyanobilin binding pocket. *Journal of molecular biology* **384**, 406–421 (2008).

[206] Biedermannová, L. & Schneider, B. Hydration of proteins and nucleic acids: Advances in experiment and theory. a review. *Biochim. Biophys. Acta Gen. Subj.* **1860**, 1821–1835 (2016).

[207] Moya, R., Kondo, T., Norris, A. C. & Schlau-Cohen, G. S. Spectrally-tunable femtosecond single-molecule pump-probe spectroscopy. *Optics Express* **29**, 28246–28256 (2021).

[208] Jumper, C. C., Rafiq, S., Wang, S. & Scholes, G. D. From coherent to vibronic light harvesting in photosynthesis. *Curr. Opin. Chem. Biol.* **47**, 39–46 (2018).

[209] Krissinel, E. & Henrick, K. Inference of macromolecular assemblies from crystalline state. *J. Mol. Bio.* **372**, 774–797 (2007).

[210] Maus, M. *et al.* An experimental comparison of the maximum likelihood estimation and nonlinear least-squares fluorescence lifetime analysis of single molecckules. *Analytical chemistry* **73**, 2078–2086 (2001).

[211] Wang, Q. & Moerner, W. Single-molecule motions enable direct visualization of biomolecular interactions in solution. *Nature methods* **11**, 555 (2014).

[212] Gelin, M. F., Egorova, D. & Domcke, W. Strong-pump strong-probe spectroscopy: effects of higher excited electronic states. *Physical Chemistry Chemical Physics* **15**, 8119–8131 (2013).

[213] Good, P. I. *Permutation, parametric, and bootstrap tests of hypotheses* (Springer Science & Business Media, 2006).

[214] Lundell, D. J. & Glazer, A. N. Allophycocyanin b. a common beta subunit in synechococcus allophycocyanin b (lambda max 670 nm) and allophycocyanin (lambda max 650 nm). *Journal of Biological Chemistry* **256**, 12600–12606 (1981).

[215] Cohen-Bazire, G., Beguin, S., Rimon, S., Glazer, A. & Brown, D. Physicochemical and immunological properties of allophycocyanins. *Archives of microbiology* **111**, 225–238 (1977).

[216] Kondo, T. *et al.* Single-molecule spectroscopy of lhcsr1 protein dynamics identifies two distinct states responsible for multi-timescale photosynthetic photoprotection. *Nat. Chem.* **9**, 772 (2017).

[217] Schlau-Cohen, G. S. *et al.* Single-molecule identification of quenched and unquenched states of lhcii. *J. Phys. Chem. Lett.* **6**, 860–867 (2015).

[218] Saga, Y. *et al.* Spectral heterogeneity in single light-harvesting chlorosomes from green sulfur photosynthetic bacterium *Chlorobium tepidum*. *Photochem. Photobiol.* **75**, 433–436 (2002).

[219] Van Oijen, A. M., Ketelaars, M., Köhler, J., Aartsma, T. J. & Schmidt, J. Spectroscopy of individual light harvesting 2 complexes of *Rhodopseudomonas acidophila*: diagonal disorder, intercomplex heterogeneity, spectral diffusion, and energy transfer in the b800 band. *Biophys. J.* **78**, 1570–1577 (2000).

[220] Bopp, M. A., Jia, Y., Li, L., Cogdell, R. J. & Hochstrasser, R. M. Fluorescence and photobleaching dynamics of single light-harvesting complexes. *Proc. Natl. Acad. Sci. U.S.A.* **94**, 10630–10635 (1997).

[221] Rutkauskas, D., Novoderezkhin, V., Cogdell, R. J. & van Grondella, R. Fluorescence spectral flucutations of single lh2 complexes from *Rhodopseudomonas acidophila* strain 10050. *Biochem.* **43**, 4431–4438 (2004).

[222] Wang, Q., Goldsmith, R. H., Jiang, Y., Bockenhauer, S. D. & Moerner, W. Probing single biomolecules in solution using the anti-brownian electrokinetic (ABEL) trap. *Acc. Chem. Res.* **45**, 1955–1964 (2012).

[223] Kapanidis, A. N. *et al.* Initial transcription by rna polymerase proceeds through a dna-scrunching mechanism. *Science* **314**, 1144–1147 (2006).

[224] Wang, S., Vafabakhsh, R., Borschel, W. F., Ha, T. & Nichols, C. G. Structural dynamics of potassium-channel gating revealed by single-molecule fret. *Nature structural & molecular biology* **23**, 31 (2016).

[225] Gwizdala, M., Kruger, T. P., Wahadoszamen, M., Gruber, J. M. & Van Grondelle, R. Phycocyanin: one complex, two states, two functions. *The journal of physical chemistry letters* **9**, 1365–1371 (2018).

[226] Gwizdala, M. *et al.* Switching an individual phycobilisome off and on. *The journal of physical chemistry letters* **9**, 2426–2432 (2018).

[227] Doust, A. B. *et al.* Developing a structure–function model for the cryptophyte phycoerythrin 545 using ultrahigh resolution crystallography and ultrafast laser spectroscopy. *Journal of molecular biology* **344**, 135–153 (2004).

[228] Curutchet, C. *et al.* Energy flow in the cryptophyte pe545 antenna is directed by bilin pigment conformation. *The Journal of Physical Chemistry B* **117**, 4263–4273 (2013).

[229] Watkins, L. P. & Yang, H. Detection of intensity change points in time-resolved single-molecule measurements. *The Journal of Physical Chemistry B* **109**, 617–628 (2005).

[230] Huang, C., Berns, D. S. & MacColl, R. Kinetics of allophycocyanin's trimer-monomer equilibrium. *Biochemistry* **26**, 243–245 (1987).

[231] Laos, A. J. *et al.* Cooperative subunit refolding of a light-harvesting protein through a self-chaperone mechanism. *Angewandte Chemie* **129**, 8504–8508 (2017).

[232] MacColl, R. *et al.* Phycoerythrin 545: monomers, energy migration, bilin topography, and monomer/dimer equilibrium. *Biochemistry* **37**, 417–423 (1998).

[233] Kaňa, R. Application of spectrally resolved fluorescence induction to study light-induced nonphotochemical quenching in algae. *Photosynthetica* **56**, 132–138 (2018).

[234] Kaňa, R., Prášil, O. & Mullineaux, C. W. Immobility of phycobilins in the thylakoid lumen of a cryptophyte suggests that protein diffusion in the lumen is very restricted. *FEBS letters* **583**, 670–674 (2009).